

HIDDEN QUANTUM INTERFERENCE AND ACHIRAL SYMMETRY BREAKING REVEALED BY NONLINEAR OPTICAL HARMONIC GENERATION SPECTROSCOPY

A Dissertation
Submitted to
the Temple University Graduate Board

In Partial Fulfillment
of the Requirements for the Degree of
DOCTOR OF PHILOSOPHY

by
Sujan Babu Subedi
April 2024

Examining Committee Members:

Darius H. Torchinsky, Ph.D., Advisory Chair, Department of Physics, Temple University
Peter S. Riseborough, Ph.D., Department of Physics, Temple University
Maria Iavarone, Ph.D., Department of Physics, Temple University
Eric Borguet, Ph.D., Department of Chemistry, Temple University

©
Copyright
2024

by

Sujan Babu Subedi
All Rights Reserved

ABSTRACT

In the first portion of this thesis, we report on the observation of the quantum interference between localized f - orbitals and dispersive d and p like bands in the LnAlSi (Ln= La, Ce, Pr, and Nd) family of Weyl semimetals. An asymmetric Fano resonance was observed, resulting from the interference between electronic states derived from lanthanide f -band and electrons in the conduction band. Rotational anisotropy second harmonic generation measurements conducted with incoming photon energies range of 1.1 - 1.8 eV revealed the presence of strong magnetic dipole (MD) transitions that we assign to the trivalent lanthanide ions. Extracting the spectra of the MD transition susceptibility tensor, we observe an asymmetric resonance at ~ 1.5 eV, consistent with a Fano lineshape. Comparison of our data with a band structure obtained from density function theory revealed the hybridization of an unoccupied band deriving from unassigned orbitals in LaAlSi and CeAlSi, the unoccupied 1D_2 state of PrAlSi, and occupied $^4I_{\frac{9}{2}}$ state in NdAlSi. Moreover, polarimetry measurement was conducted at normal incidence in the paramagnetic phase of LnAlSi revealed a novel, nonlinear form of electromagnetically induced chirality (EIC) that derives from resonant MD transitions. This form of nonlinear magnetoelectricity is expressed as $P_i = \chi_{ijk}^{em} E_j H_k$, which causes the emission of elliptically polarized SHG.

In a separate study, we used the second and third harmonic nonlinear harmonic generation spectroscopy to study 1T-TiSe₂ below its charge density wave phase transition temperature at 200 K. The lack of a second harmonic signal below and above the transition temperature indicated that the low-temperature symmetry-breaking phase is achiral. Further study using rotational anisotropy nonlinear third harmonic generation revealed that 1T-TiSe₂ experiences a non-trivial phase transition at ~ 180 K within the charge density phase that comprises two separate domain types that randomly rearrange upon thermal cycling. Taken together, our data support the onset of orbital ordering at 180 K without the emergence of an electronically chiral state.

Finally, we describe THz emission spectroscopy to study the circular photogalvanic effect (CPGE) and linear photogalvanic effect (LPGE) spectra of the structurally chiral Weyl semimetal PdGa. We reveal that CPGE and LPGE spectra produce signals of opposite signs for the two PdGa enantiomers, as predicted by theory. Measurement of the spectra deriving from the material's bulk reveals a peak in the photogalvanic spectra at 0.68 eV, which is due to optical transitions between the parallel bands near the Weyl nodes dispersing from Γ to R and similar transitions between M and R. Surface sensitive measurements are consistent with helicoidally dispersing states of opposite helicity from the two different chirality samples.

Dedicated to My Family

ACKNOWLEDGEMENTS

I am thankful to those who have supported and guided me during my journey through the Ph.D. program.

First and foremost, I would like to extend my deepest gratitude to my advisor, Professor Darius Torchinsky. His guidance and support were invaluable, from my first day in the lab to the preparation of my thesis manuscript. I appreciate his availability for hours of discussion on physics and technical issues, which helped me grasp scientific studies and techniques with which I was previously unfamiliar. He was a superb model for me not only in scientific studies but also in being helpful outside the lab. I am also indebted to him for providing many opportunities to collaborate with other experimental groups and to attend several amazing conferences in the US.

I am thankful to Professor Fazel Tafti for providing the LaAlSi ($\text{Ln} = \text{La}, \text{Ce}, \text{Pr}, \text{Pr}_{0.8}\text{Nd}_{0.2}, \text{and Nd}$) samples and for the collaborative work on the SmAlSi sample. I would like to thank Professor Goran Karapetrov for providing the 1T-TiSe_2 sample and for doing collaborative work on it. I thank my faculty oversight committee members, Professor Alexander Gray and Professor Adrienne Ruzsinsky, for their guidance. I am also thankful to Professor Peter S. Riseboroug, Professor Maria Iavarone, and Professor Eric Borguet for being members of the thesis committee.

Many thanks to Dr. Baozhu Lu and Dr. Manita Rai for teaching me and helping with the experimental setup. I would also like to thank Wesley Deeg and Awadesh Das for their help in the lab.

I would like to thank my parents and my wife, Sabina Lamsal, for always being supportive. Their love, care, and encouragement have been crucial to my success. I cannot imagine going through this endeavor without their unwavering support.

Finally, I wish to express my gratitude to my friends Raj Kishor Sah, Dr. Pradeep Bhetwal, Dr. Jay Poudel, Dr. Babu Ram Pokharel, Dr. Santosh Neupane, Dr. Navagyan Ghimire, and Anoj Aryal for their invaluable guidance and consistent encouragement.

TABLE OF CONTENTS

	Page
ABSTRACT	iii
DEDICATION	v
ACKNOWLEDGEMENTS	vi
LIST OF FIGURES	xi
LIST OF TABLES	xv
CHAPTER	
1. INTRODUCTION	1
2. INTRODUCTION TO FANO RESONANCE AND ELECTROMAGNETICALLY INDUCED CHIRALITY IN WEYL SEMIMETALS	6
2.1 Fano Resonance	6
2.1.1 Two Coupled Oscillators	8
2.1.2 Electromagnetically Induced Transparency	11
2.2 Electromagnetically Induced Chirality	11
2.3 Overview of Topological Materials	14
2.4 Topological Semimetals	17
2.5 Weyl Semimetals	18
2.5.1 Type-I and type-II Weyl Semimetal	20
2.6 Recent Nonlinear Experimental Study on Weyl Semimetal	21
2.6.1 SHG in Weyl Semimetals	22
2.6.2 Photocurrent in Weyl Semimetals	23
2.7 Weyl Semimetals- LnAlSi and PdGa	24
2.7.1 LnAlSi	24
2.7.2 PdGa	26
3. CHARGE DENSITY WAVE IN TRANSITION METAL DICHALCOGENIDE 1T-TiSe ₂	28
3.1 Brief Introduction to Charge Density Wave Physics	28
3.1.1 Excitonic Instability	31

3.1.2	Jahn-Teller Effect	33
3.2	Transition Metal Dichalcogenides (TMDs)	35
3.3	Overview of the Properties of 1T–TiSe ₂	37
3.3.1	Lattice and Electronic Structure	37
3.3.2	CDW in 1T–TiSe ₂	38
3.4	Mechanism Behind the Phase Transition	39
3.5	Recent Study on the Nature of CDW Phase Transition	42
4.	EXPERIMENTAL METHODS	47
4.1	Time Resolved Pump-Probe Spectroscopy	47
4.1.1	Experimental Alignment and Challenges	50
4.1.2	Pump-Probe Data Detection Method	51
4.2	Nonlinear Harmonic Generation	52
4.2.1	Second Harmonic Generation	54
4.2.2	Third Harmonic Generation	61
4.2.3	Rotational Anisotropy Nonlinear Harmonic Generation	62
4.3	Photogalvanic Effect	63
5.	QUANTUM INTERFERENCE-DRIVEN NONLINEAR ELECTROMAGNETICALLY INDUCED CHIRALITY IN THE LnAlSi (Ln=La, Ce, Pr AND Nd) WEYL SEMIMETALS	67
5.1	Introduction	68
5.2	Experiment	73
5.3	Results and discussion	77
5.3.1	MD Transition and Fano Resonance Effect	77
5.3.2	Electromagnetically Induced Chirality (EIC) at Nonlinear Order	84
5.4	Conclusion	88
6.	TIME RESOLVED CIRCULAR DICHROISM AND NON-LINEAR OPTICAL HARMONIC GENERATION STUDY OF THE CHARGE DENSITY WAVE PHASE OF THE TRANSITION METAL DICHALCOGENIDE (1T–TiSe ₂)	90
6.1	Background	91
6.2	Time-Resolved Pump-Probe Circular Dichroism	95
6.2.1	Experimental Setup	95
6.2.2	Results of tr-CD Experiments	96
6.3	Rotational Anisotropy Nonlinear Harmonic Generation (RA-NHG)	97
6.3.1	Static Scattering Plane Rotational Anisotropy Second and Third Harmonic Generation	100
6.4	Conclusions	108

7. TERAHERTZ EMISSION PHOTOGALVANIC EFFECT SPECTROSCOPY OF RIGHT AND LEFT HAND ENANTIOMERS OF THE CHIRAL MULTIFOLD FERMION PdGa	110
7.1 Introduction	110
7.2 Experimental Setup	112
7.3 Results and Discussion	115
7.4 Conclusions	118
8. CONCLUSIONS	119
BIBLIOGRAPHY	121
APPENDIX	144
A. ROTATIONAL ANISOTROPY SECOND HARMONIC GENERATION WITH SUBGROUP OF C_{4v}	145
A.1 C_{4v} Electric Dipole	146
A.2 C_{2v} Electric Dipole	149
A.3 C_2 Electric Dipole	151
A.4 C_4 Electric Dipole	153
A.5 C_s Electric Dipole	155
A.6 C_{4v} Magnetic Dipole	157
A.7 C_{4v} Magnetic Dipole and Electric Dipole	159

LIST OF FIGURES

Figure		Page
2.1	Two coupled oscillators	8
2.2	Electromagnetically induced transparency	12
2.3	Five-level scheme for the electromagnetic induce cross-coupling.	13
2.4	3D topological matter	18
2.5	Type-I and Type-II Weyl nodes	20
2.6	Crystal and band structure of LnAlSi and DOS for PrAlGe.	25
2.7	Magnetic order in LnAlSi materials with transition temperatures.	26
2.8	Unit cell, band structure and first BZ of PdGa.	27
3.1	Schematic representation of a Peierls transition.	29
3.2	Excitonic instability	31
3.3	Jahn–Teller effect with distortions.	34
3.4	The schematic model for 2H and 1T phase of TMDs	36
3.5	Electronic structures of 1 T–TiSe ₂	38
3.6	Excitonic insulator mechanism.	40
3.7	CDW transition temperature as a function of Cu intercalation in TiSe ₂	42
3.8	STM image of 1 T–TiSe ₂ with unit vectors and amplitude of line profile along unit vectors	43
3.9	Schematic representation of left and right-handed CDWs in 1 T–TiSe ₂	44
3.10	STM image of 1 T–TiSe ₂	44
3.11	Integrated intensities of the superlattice reflections in 1 T–TiSe ₂	45
3.12	A diagram illustrating the transformation of the 1 T–TiSe ₂ structure into either the achiral or chiral structure at low temperatures.	46

4.1	experimental setup for time-resolved pump-probe measurement where pump and probe measurement	49
4.2	The experimental setup for pump-probe traces with the DAQ card.	51
4.3	Schematic view of the N^{th} harmonic conversion of an incidence beam	52
4.4	A schematic experimental diagram for rotating quarter waveplate (QWP) polarimetry measurement.	57
4.5	Schematic diagram of setup used in rotational anisotropy measurements.	63
4.6	Schematic experimental geometry for THz emission spectroscopy measurement.	66
5.1	Schematic diagram of setup used in SHG measurement.	75
5.2	Plot of the Fano lineshape with energy and assymetic parameters.	78
5.3	Second harmonic generation data and fit for NdAlSi.	79
5.4	Experimentally measured spectra of χ_{ijk}^{em} with error bars and Fano fit to the Fano lineshape in LnAlSi	80
5.5	Experimentally measured spectra for electric SHG susceptibility χ_{zzz}^{eee} in LnAlSi.	81
5.6	Diagram that representing Fano resonance in LnAlSi.	82
5.7	Plot for Fano fitting asymmetry parameter q with atomic number.	82
5.8	Schematic diagram of the electronic transition hierarchy in LnAlSi.	83
5.9	Schematic diagram of the setup used in polarimetry measurements to determine the polarization state of SHG emitted from LnAlSi at normal incidence.	85
5.10	Polarimetry data of emitted SHG from $\text{Pr}_{0.8}\text{Nd}_{0.2}\text{AlSi}$ sample.	87
5.11	Cartesian and polar plot of the ellipticity angle of the emitted SHG due to linearly polarized incident light on $\text{Pr}_{0.8}\text{Nd}_{0.2}\text{AlSi}$	88
5.12	Dependence of the degree of ellipticity with Ln atomic number in LnAlSi.	89
6.1	Fermi surface and CDW vectors in 1T-TiSe ₂	92

6.2	Diagram depicting the transformation of high-temperature structure into either the achiral or the chiral CDW phase at low temperature in 1 T–TiSe ₂ .	93
6.3	Experimental Setup for time-resolved pump-probe measurement.	95
6.4	Time-resolved change in reflectivity with right and left circularly polarized probe beam at low temperature.	97
6.5	Transient circular dichroism (Tr-CD) measured on 1 T–TiSe ₂ with 620 nm and 680 nm probe wavelengths.	98
6.6	Static scattering plane RA-SHG experimental setup.	99
6.7	SHG Experimental data at 150 K.	101
6.8	THG data from 1 T–TiSe ₂ at 150 K using 1830 nm incident wavelength.	103
6.9	THG tensor elements $\chi_{ijk}^{(3)}$ as a function of temperature.	104
6.10	RA-THG susceptibility tensor element (χ_{xxxx}) as a function of temperature from three different thermal cycles.	105
6.11	RA-THG susceptibility tensor element $\chi_{xxxx}^{(3)}$ fitted by the critical exponent Equation for different temperature cycles.	106
6.12	Schematic representation of the Fermi surface pockets in the first Brillouin zone of TiSe ₂ with resulting polarization direction due to orbital ordering.	109
7.2	Frequency-dependent second-order conductivity for CPGE and LPGE derived from numerical calculations based on a tight binding model of RhSi.	113
7.3	Experimental setup used here for THz emission spectroscopy.	114
7.4	THz time-domain data for LPGE with spectra for both PdGa enantiomers.	116
7.5	THz time-domain data for CPGE with spectra.	117
7.6	Band structure of PdGa with spin-orbit coupling (SOC).	118
A.1	RA-SHG data on LnAlSi fitting with bulk electric dipolar SHG in the C _{4v} point group for incoming wavelength 1350nm.	148

A.2	RA-SHG data on LnAlSi fitting with bulk electric dipolar SHG in the C_{4v} point group for incoming wavelength 800nm.	149
A.3	RA-SHG data on LnAlSi fitting with bulk electric dipolar SHG in the C_{2v} point group for incoming wavelength 800nm.	151
A.4	RA-SHG data on LnAlSi fitting with bulk electric dipolar SHG in the C_2 point group for incoming wavelength 800nm.	153
A.5	RA-SHG data on LnAlSi fitting with bulk electric dipolar SHG in the C_4 point group for incoming wavelength 800nm.	155
A.6	RA-SHG data on LnAlSi fitting with bulk electric dipolar SHG in the C_s point group for incoming wavelength 800nm.	157
A.7	RA-SHG data on LnAlSi fitting with bulk electric dipolar and magnetic dipolar SHG in the C_{4v} point group for incoming wavelength 800nm. . . .	160

LIST OF TABLES

Table		Page
5.1	Fano resonance fitting parameters for LnAlSi	80
A.1	Character table for C_{4v} point group.	145

CHAPTER 1

INTRODUCTION

In recent years, two phases of matter have dominated the focus of hard condensed matter research: topologically ordered phases and two-dimensional materials. These trends began with the discovery of the quantum Hall effect in 1980 [1], with research in topological physics exploding in 2007 with the discovery of bulk topological insulators [2]. Since then many more 3D topological phases have been discovered such as Dirac semimetals [3], Weyl semimetals [4, 5] and, more recently, nodal line semimetals [6] and axion insulators [7]. Similarly, in the two-dimensional phase of materials, the fabrication of a single atomic layer of graphene using mechanical exfoliation in 2004 [8] led to the development of other 2D materials such as the transition metal-dichalcogenides (TMDs) [8], hexagonal boron nitride (h-BN) [9] and black phosphorous [10]. Below, we will briefly discuss each material class as it relates to my thesis.

Topological materials host exotic electronic properties, and nontrivial band structures give rise to protected electronic states at their surface or interface. In 2005, Kane and Mele proposed that time-reversal symmetry would impose a topological index Z_2 , which classifies the topological property of the topologically ordered phase [11]. It has been realized in 3D topological insulators, which exhibit four distinct Z_2 indices [2], with one being strong [12], indicating the existence of insulating bulk material with metallic surface properties [13]. The topological index typically applies to systems characterized by an insulating bulk with a topologically protecting surface [12]. Recently, a topologically protected semimetallic phase has been observed in which bands of opposite polarity cross at a 1D point in the Brillouin zone, known as either Dirac points or Weyl points depending upon the symmetries realized by the lattice and the electrons [14]. The materials that host

the Dirac points are known as Dirac semimetals, which preserve both time-reversal and inversion symmetry [5]. Due to the presence of both symmetries, all bands on the Dirac semimetal are doubly degenerate. In the topological semimetals that break either time-reversal-symmetry and/or inversion symmetry, the band degeneracy is lifted, which splits the Dirac nodes into two opposite chirality nodes, known as Weyl nodes. The low-energy quasiparticles are described by the Weyl equation, and thus, these materials are known as Weyl semimetals. In both topological semimetals, the projection of the Dirac/Weyl nodes on the surface Brillouin zone is connected to the so-called Fermi arc. Fermi arc states are closed for Dirac semimetals and unclosed for Weyl semimetals. The unique feature of the unclosed Fermi arc and linearly dispersing bands gives novel physical phenomena.

Weyl semimetals are further classified into Type-I and Type-II based on the geometry of the cone formed by the linearly dispersing bands. In Type-I Weyl semimetals, the Weyl cones are vertical and have a point-like Fermi surface, while in Type-II Weyl, they are tilted, and electron and hole pockets are connected at Weyl points. The tilting of the Weyl cones breaks Lorentz invariance and can lead to unique properties such as directional-dependent conductivity [15]. The study of the electromagnetic response of magnetic Weyl semimetals with both type-I and type-II fermions is still relatively limited. Thus, we have studied the LnAlSi ($\text{Ln} = \text{La, Ce, Pr, Pr}_{0.8}\text{Nd}_{0.2}, \text{Nd}$) series of WSMs. They are noncentrosymmetric materials belonging to the space group ($I4_1md$), the same as the first experimentally discovered Weyl semimetal TaAs. High-field magnetotransport measurements have revealed that LnAlSi materials host both type-I and type-II Weyl nodes [16]. The family of LnAlSi belongs to magnetic or nonmagnetic semimetals, depending on the presence of f-electron in rare earth elements, i.e., LaAlSi is paramagnetic while the rest host different forms of the magnetic order. An electric dipole (ED) primarily mediates most light-matter interactions, but the intra- $4f$ optical transition of Ln^{3+} enhances magnetic dipole contributions. Most rare-earth ions support the strong magnetic dipole transitions [17]. Such a strong magnetic dipole has been observed in Eu^{3+} atoms with a transition from ${}^7F_0 \rightarrow {}^5D_1$ [18].

Electromagnetically induced chirality (EIC) is defined by an achiral material obeying the constitutive equation of a chiral medium, i.e., it induces magnetoelectric cross-coupling term [19]. The quantum coupling between the MD transition and ED transition has been extensively studied in magnetically ordered materials [20] and nanoparticles [21]. Here, we will demonstrate EIC at second optical order in LnAlSi, signaled by a Fano resonance in the SHG spectrum and measured by helical SHG emission for normal incidence linearly polarized light.

The transition metal dichalcogenides (TMDs) are another class of material that exhibit a wide range of unique electronic, optical, and mechanical properties. The TMDs comprise a two-dimensional material with the generic chemical formula MX_2 , ($\text{M} = \text{Mo}, \text{W}, \text{Ti}, \text{etc.}; \text{X} = \text{S}, \text{Se}, \text{Te}$) and are characterized by a hexagonal lattice structure. The common structural phases of TMDs are octahedral (1T) and trigonal prismatic (2H). In the 1T phase, the transition metal ions are surrounded by six chalcogen atoms in an octahedral configuration, while in the 2H phase, the transition metal ions are surrounded by six chalcogen atoms in a trigonal prismatic configuration [22].

Electronically, TMDs exist in semiconductors (e.g., MoSe_2 , WS_2), semimetals (e.g., WTe_2 , TiSe_2), and metals (e.g., VSe_2), and possess exceptional properties such as a tunable band gap [23], high carrier mobility [24], strong spin-orbit coupling [25] and strong light-matter interactions due to quantum confinement [26]. Certain TMDs support a charge density wave (CDW) instability due to their electronic structures spontaneously undergoing a periodic modulation under various conditions, such as temperature [27], pressure [28], intercalation [29], doping [30], and optical excitation [31]. Thus, the TMDs are an ideal platform for studying a wide range of physical phenomena.

The TMD studied here, 1T-TiSe₂, is no different in that it also exhibits a wide range of electronic, structural, and optical properties [32]. Angle-resolved photoemission spectroscopy (ARPES) [33], scanning tunneling microscopy (STM) [34], and X-ray diffraction (XRD) [27] studies show the existence of CDW phase transition below ~ 200 K. However,

the mechanism and nature of the phase transition are still a subject of intense debate. One important question regarding the CDW phase transition is whether it is driven by electron-phonon interaction [35] or the formation of excitonic pairs [36]. 1T–TiSe₂ was at first proposed to exhibit a secondary transition to a chiral CDW phase at 180 K as observed through STM [34], which is attributed to helical charge ordering induced by a $\frac{2\pi}{3}$ phase slip from layer among the three planes that comprise the CDW. Subsequent STM experiments found no differences in charge density configuration between the neighboring layers [37]. Even though low-temperature optical measurement has been done in the monolayer of transitional metal dichalcogenide in 1T–TiSe₂ and observe the CDW-induced second harmonic generation (SHG) [38], higher-order nonlinear experiments on bulk have yet to be performed, which was our focus here.

In this thesis, we measured the nonlinear optical response from the topological Weyl semimetals PdGa and LnAlSi and the 2D material 1T–TiSe₂. In LnAlSi, using second harmonic generation spectroscopy, we measured the second harmonic generation susceptibility spectrum with incoming photon energies ranges of 1.1 - 1.8 eV. Significantly, we observed that there was a strong magnetic dipole contribution to SHG. This revealed the strong band hybridization between localized *f*–electron and itinerant conduction *p*– and *d*– electrons, leading to a Fano resonance in the SHG spectrum. We also observed EIC due to this quantum interference between magnetic dipole transitions and electric dipole transitions. Second and third harmonic generation measurements were performed in 1T–TiSe₂ below its charge density wave phase transition temperature to study the low-temperature symmetry of the material. THz emission spectroscopy was also employed to study the circular photogalvanic effect (CPGE) and linear photogalvanic effect (LPGE) spectra of the bulk of both left and right handed enantiomers of the structurally chiral Weyl semimetal PdGa, which resulted in opposite polarity THz transients in both CPGE and LPGE spectra for the enantiomers due to the opposite handedness.

This thesis is organized as follows:

In Chapter 2, we will discuss the theory and recent progress in nonlinear study on Weyl semimetals. We will also discuss electric and magnetic dipole transitions and how they may result in quantum coherent phenomena such as the Fano resonance [39] and EIC [19] in the LnAlSi series of Weyl Semimetals. Chapter 3 includes the theory of transition metal dichalcogenides and recent experimental progress on 1T-TiSe₂. We will discuss experimental methods such as pump-probe spectroscopy and nonlinear optical effects, including second and third harmonic generation and the photogalvanic effect, in Chapter 4. Chapter 5 will focus on the study of rotational anisotropy nonlinear optical measurements on the LnAlSi family of materials. Nonlinear measurement data reveals the magnetic dipole transition in the paramagnetic phase, which is evident as a Fano resonance that leads to EIC in the second order. The study of the charge density phase of 1T-TiSe₂ using the third-harmonic generation technique will be presented in Chapter 6. Chapter 7 will include the study of LPGE and CPGE in both left and right handed enantiomers of the structurally chiral Weyl semimetal PdGa. In Chapter 8, we will provide a summary of our conclusions.

CHAPTER 2

INTRODUCTION TO FANO RESONANCE AND ELECTROMAGNETICALLY INDUCED CHIRALITY IN WEYL SEMIMETALS

This chapter will briefly discuss the fundamental concepts of two quantum effects: the Fano resonance and electromagnetically induced chirality. We then will provide a basic introduction to Weyl semimetals and conclude by introducing the two primary material classes explored in this thesis: LnAlSi ($\text{Ln} = \text{La, Ce, Pr and Nd}$) family Weyl semimetals and the chiral Weyl semimetal belonging to space group 198.

2.1 Fano Resonance

Resonance typically refers to the enhancement of a response to an external perturbation at a specific energy or wavelength. It usually manifests as a symmetric peak in the response curve. In 1961, Ugo Fano identified an asymmetric resonance profile in the absorption spectra during his analysis of the spectral lines of helium [40]. Later, he provided a theoretical quantum mechanical explanation for this phenomenon by examining the autoionizing states of atoms, thereby defining it as a Fano resonance [41]. The Fano resonance is characterized by an asymmetric resonance profile resulting from the interference between two different states: a discrete resonant quantum state and a much broader resonance “continuum” of states. This phenomenon requires the energy of the discrete state to fall within the energy range of the continuum of states. Typically, near the resonance energy, the amplitude of the background scattering changes slowly with energy, in contrast

to the resonant scattering amplitude, which exhibits rapid changes in both magnitude and phase. This difference is responsible for the asymmetric profile.

In mathematical terms, the Fano lineshape is dependent upon the resonance energy E_{res} and the linewidth of the resonance curve Γ_{res} . The intensity of the asymmetric lineshape near resonance is given by

$$I(E) \propto \frac{(q \frac{\Gamma_{res}}{2} + E - E_{res})^2}{(\frac{\Gamma_{res}}{2})^2 + (E - E_{res})^2} \approx \frac{(q + \frac{2(E-E_{res})}{\Gamma_{res}})^2}{1 + (\frac{2(E-E_{res})}{\Gamma_{res}})^2} \quad (2.1-1)$$

where q is the Fano parameter that induces the asymmetry in the resonance line profile. It is dependent upon the relative phase difference between the discrete resonance at E_{res} and the background continuum.

Wood et al. observed the first asymmetric line shape in 1902 when working on metallic gratings, where anomalies served to improve grating efficiency [42]. Although the concept of Fano resonance was developed in the context of atomic physics, it also appears in nuclear and molecular physics [43, 44], in scattering theory [45], resonant tunneling in semiconductor devices [46], and nanophotonics and plasmonics [47]. In nanophotonics, the Fano resonance enhances light-matter interactions at the nanoscale [39]. It is also important to the design of metamaterials [48] and photonic crystals [49], some of which host tunable Fano resonances [50], which are useful for creating highly sensitive sensors and narrow band filters as well as devices for controlling light flow at the subwavelength scale [51]. In recent years, the study of Fano resonance has extended to quantum dots [52], quantum wells [53], and even in topological insulators [54] and semimetals [55]. Our interest in Fano resonances is more relevant to nonlinear optical systems, where it could enhance or control nonlinear phenomena such as harmonic generation [56].

2.1.1 Two Coupled Oscillators

Although the Fano resonance is a quantum effect, we can gain some insight on it using a classical model based on coupled oscillators. We begin by considering an oscillator, labeled A , with a large damping rate subject to an external time-dependent driving force. This oscillator is the equivalent of the continuum. Another oscillator, labeled B , with a low damping rate that is not driven serves as the equivalent of the discrete state.

These two oscillators, A and B , are coupled by a spring of constant K . Let M_a , k_a , and γ_a be the mass, spring constant, and damping coefficient for oscillator A , respectively. Similarly, M_b , k_b , and γ_b are the mass, spring constant, and damping coefficient for oscillator B , respectively. For simplicity, let us assume the unit mass of two oscillators is the same $M_a=M_b=1$.

With a time-harmonic force $F(t)$ applied to oscillator A , the equations of motion of the system are

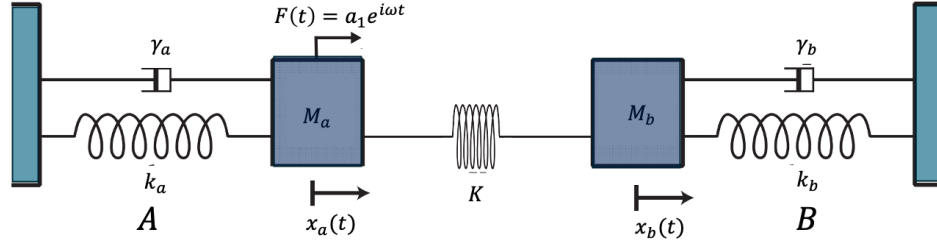


Figure 2.1: Two coupled oscillators. An Oscillator A is driven by external harmonic force $F(t)$ and coupled with oscillator B by spring constant K . k_a and k_b are the spring constant for oscillator A and B . Figure taken from Ref. [57].

$$\ddot{x}_a + \gamma_a \dot{x}_a + \omega_a^2 x_a + v_{ab} x_b = a_1 e^{i\omega t} \quad (2.1-2)$$

$$\ddot{x}_b + \gamma_b \dot{x}_b + \omega_b^2 x_b + v_{ab} x_a = 0 \quad (2.1-3)$$

Assuming a time-harmonic behavior for the response of the oscillators $x_a(t) = c_a(\omega)e^{i\omega t}$ and $x_b(t) = c_b(\omega)e^{i\omega t}$, the amplitude response of oscillator A is

$$c_a(\omega) = \frac{\omega_b^2 - \omega^2 + i\gamma_b\omega}{(\omega_a^2 - \omega + i\gamma_a\omega)(\omega_b^2 - \omega^2 + i\gamma_b\omega) - v_{ab}^2} a_1 \quad (2.1-4)$$

The amplitude $c_a(\omega)$ will give the characteristics of the resonance behavior reflecting the presence of the second oscillator B near the frequency $\omega = \omega_b$. The numerator of Equation 2.1-4 defines the extra phase shift,

$$\theta = \tan^{-1} \left(\frac{\gamma_b \omega_b}{\omega_b^2 - \omega_a^2} \right) \quad (2.1-5)$$

which will provides the background phase shift of the resonance in $c_a(\omega)$.

The coupled oscillator has two eigenmodes: a symmetric mode in which the two oscillators swing back and forth together and an antisymmetric mode in which they move in opposite directions. By solving the Equations 2.1-2 and 2.1-3 for under the condition of friction i.e., ($\gamma_a, \gamma_b = 0$), the eigenmode can be obtained as

$$(\omega_a^2 - \omega^2)(\omega_b^2 - \omega^2) - v_{ab}^2 = 0 \quad (2.1-6)$$

If the coupling parameter is weak ($\omega_b - \omega_a \gg v_{ab}$), the eigenmodes of the coupled system can be written as

$$\tilde{\omega}_a^2 \approx \omega_a^2 - \frac{v_{ab}^2}{\omega_b^2 - \omega_a^2}, \quad \tilde{\omega}_b^2 \approx \omega_b^2 + \frac{v_{ab}^2}{\omega_b^2 - \omega_a^2} \quad (2.1-7)$$

which are shifted by $v_{ab}^2/(\omega_b^2 - \omega_a^2)$ in the opposite direction from their original.

In the vicinity of $\omega = \omega_b$, we may define the shift in resonance ε as

$$\varepsilon = \omega^2 - \tilde{\omega}_b^2 = \omega^2 - \omega_b^2 - \frac{v_{ab}^2}{\omega_b^2 - \omega_a^2} \quad (2.1-8)$$

$$\implies \omega^2 = \varepsilon + \omega_b^2 + \frac{v_{ab}^2}{\omega_b^2 - \omega_a^2} \quad (2.1-9)$$

With Equations 2.1-4 and 2.1-9 and in the neighbor of $\varepsilon = 0$, if we use the approximation

$$\frac{v_{ab}^2}{\omega_b^2 - \omega_a^2} \gg \varepsilon \approx 0 \quad (2.1-10)$$

the amplitude Eq. 2.1-4 can be written as,

$$c_a(\omega) \approx -\frac{\zeta + q}{\zeta - i} \frac{a_1}{\omega_b^2 - \omega_a^2} \quad (2.1-11)$$

where,

$$\zeta = \frac{1}{\gamma_a \omega_b} ((\omega_b^2 - \omega_a^2)^2 / v_{ab})^2 \varepsilon, \quad q = \frac{1}{\gamma_a \omega_b} (\omega_b^2 - \omega_a^2) \quad (2.1-12)$$

Therefore, the magnitude of the oscillation of the system $|c_a(\omega)|^2$ can be written as,

$$|c_a(\omega)|^2 \approx \frac{(\zeta + q)^2}{\zeta^2 + 1} \frac{a_1^2}{(\omega_b^2 - \omega_a^2)^2} \quad (2.1-13)$$

This is a Fano formula where q is the Fano profile parameter. substituting the value of q in the Equation 2.1-5, the phase shift of the damped oscillator is $\tan^{-1}(1/q)$ or $\cot^{-1}(q)$. This classical result is the analog to the quantum effect, that is at the heart of electromagnetically induced transparency.

2.1.2 Electromagnetically Induced Transparency

Electromagnetically induced transparency (EIT) is a special case of Fano resonance [41]. When the frequencies of the two modes match in Equation 2.1-12 i.e., $\omega_a = \omega_b$, the Fano parameter vanishes at $q = 0$ and generates the transmission band [39], which is shown in Figure 2.2a. It is a quantum interference effect that eliminates optical absorption in an opaque medium [40]. This is due to destructive interference between the two excitation pathways, effectively preventing the probe beam's absorption.

EIT can be defined by the three-level system as shown in Figure 2.2b, where $|1\rangle$ is the ground state couple to the excited state $|3\rangle$ by a laser at Rabi frequency Ω_p . When another electromagnetic field resonant to the transition from $|2\rangle$ to $|3\rangle$ is applied, there are two ways to excite atoms from the ground state to the upper level: $|1\rangle \rightarrow |3\rangle$ and $|1\rangle \rightarrow |3\rangle \rightarrow |2\rangle \rightarrow |3\rangle$ that can interfere destructively, allowing the absorption to reach zero.

EIT was first predicted in 1989 by Harries at coherent population trapping [58], and experimentally, it has been realized in Sr vapor by Boller et al. [59] and Field et al. in Pb vapor [60]. EIT has been widely studied in e.g., atomic systems [61], superconductors [62] and photonic crystals [39]. EIT materials not only possess zero absorption but also over a limited frequency range, exhibit giant nonlinearity.

2.2 Electromagnetically Induced Chirality

Electromagnetically-induced chirality (EIC) is a quantum coherent interference effect due to the electromagnetic cross-coupling between an electric dipole (ED) transition and a magnetic dipole (MD) transition [19]. Chirality is an asymmetry property in which a material cannot be superposed upon its mirror image.

In chiral medium, the induced polarization and magnetization are different from the normal

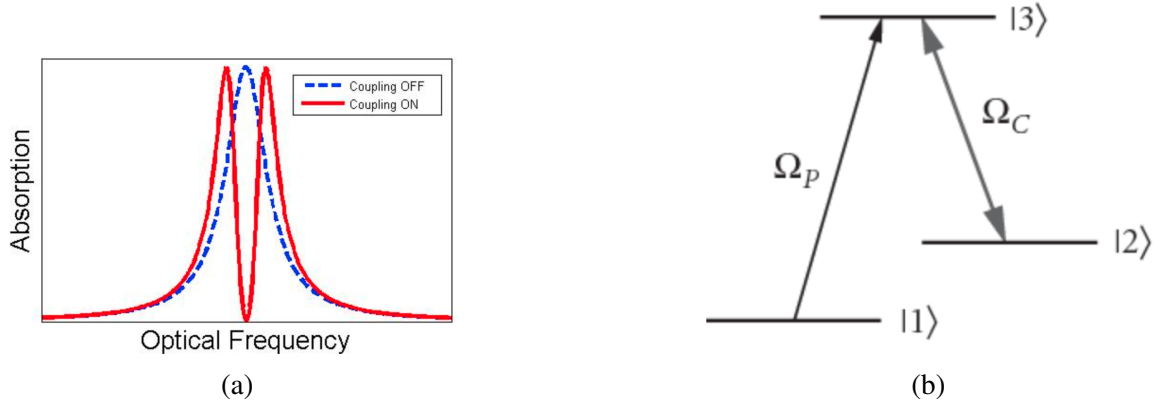


Figure 2.2: (a) Electromagnetically induced transparency (EIT) with absorption line. Initially, a weak probe beam is absorbed, illustrated by the blue line; however, the introduction of a second coupling beam leads to the creation of a "window" within this absorption region, depicted in red, where absorption is significantly reduced. (b) three-level system scheme for EIT. Figure taken from [63].

medium and are given as

$$P_i = \chi_{ij}^{ee} E_j + \chi_{ij}^{em} H_j \quad (2.2-14)$$

and

$$M_i = \chi_{ij}^{mm} H_j + \chi_{ij}^{me} E_j \quad (2.2-15)$$

where χ_{ij}^{em} and χ_{ij}^{me} are electric and magnetic susceptibilities of the chiral medium.

EIC typically emerges not from the inherent structural asymmetry of matter but from its interaction with electromagnetic fields. The process is fundamentally grounded in the principle of quantum coherence, which allows for a system to exist in a superposition of quantum states otherwise symmetric.

The operational basis at EIC involves preparing atoms or molecules in a dark state i.e., a superposition state that interacts with both the electric and magnetic components of an electromagnetic field. This interaction is mediated through a driving field, often a laser, which can control the magnitude and phase of the coherence between the quantum states.

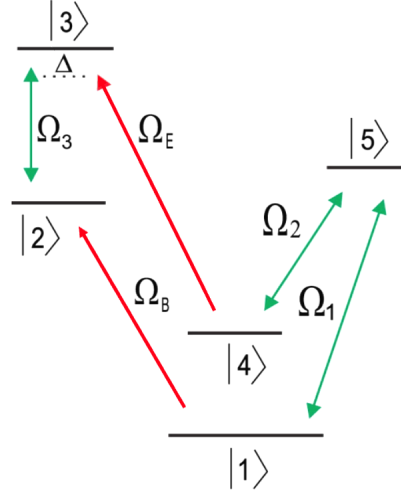


Figure 2.3: Five-level scheme for the electromagnetic induce cross-coupling. Ω_1 , Ω_2 and Ω_c are the Rabi frequencies of the external laser field. Ω_E and Ω_B are Rabi frequencies of electric and magnetic dipole fields. The electric and magnetic dipole fields are coupled with Ω_3 , with the upper level at detuning Δ . Figure taken from [19].

One of the various atomic level “topologies” for EIC via the closed-loop level scheme shown in Figure 2.3, where photon absorption and emission occurs cyclically. It contains two nearly degenerate ground states $|1\rangle$ and $|4\rangle$. These ground states are coupled to the excited state $|5\rangle$ by control fields of Rabi frequency Ω_1 and Ω_2 . The ED transition and MD transition states $|3\rangle$ and $|2\rangle$, respectively, are coupled to $|1\rangle$ and $|4\rangle$, as shown in the Figure 2.3. The nearly degenerate ground coherence forms the dark state, which leads to an asymmetrical distribution of electromagnetic fields around the atoms. This asymmetry, induced by the precise control of light, can make the system behave as if it were chiral. This setup ensures that the induced chirality is not a transient effect but is embedded within the material’s interaction with the light.

From Eqs 2.2-14 and 2.2-15, the refractive index for a circularly polarized beam in the chiral medium is

$$n = \sqrt{(1 + \chi^{ee})(1 + \chi^{mm}) - \frac{(\chi^{em} + \chi^{me})^2}{4}} + \frac{i}{2}(\chi^{em} - \chi^{me}) \quad (2.2-16)$$

If the material satisfies the relation, $\chi^{em} = -\chi^{me} = i\chi$, then

$$n = \sqrt{(1 + \chi^{ee})(1 + \chi^{mm})} - \xi \quad (2.2-17)$$

implying that if $\chi > \sqrt{(1 + \chi^{ee})(1 + \chi^{mm})}$ the refractive index is negative. Negative refractive index due to EIC has been studied extensively [64] and shows evidence of tunability [65].

2.3 Overview of Topological Materials

Michael Berry first introduced his theoretical model in 1984 to study the characteristics of topological properties in condensed phase systems under the cyclic, adiabatic evolution of eigenstates of a Hamiltonian $H(\mathbf{R}_i)$ via slowly varying parameters $\mathbf{R}_i = (\mathbf{R}_1(t), \mathbf{R}_2(t), \dots)$ [66]. The eigenvalue for the n^{th} eigenstate is defined as

$$H(\mathbf{R}) |n(\mathbf{R})\rangle = \varepsilon_n(\mathbf{R}) |n(\mathbf{R})\rangle \quad (2.3-18)$$

The states evolved adiabatically in parameter space (so that they remain in the same eigenstate) will acquire an extra geometrical, gauge-invariant phase factor known as the Berry phase. That geometrical phase only depends on the path taken through the parameter space. In particular, Berry found that this phase can be written as

$$\gamma_n = \oint_c d\mathbf{R} \cdot A_n(\mathbf{R}) \quad (2.3-19)$$

where,

$$A_n(\mathbf{R}) = i \langle n(\mathbf{R}) | \frac{\partial}{\partial \mathbf{R}} | n(\mathbf{R}) \rangle \quad (2.3-20)$$

is known as the Berry connection, which does not explicitly depend on time. Since $A_n(\mathbf{R})$ is gauge-dependent, it cannot be physically observed.

Using the generalized Stokes theorem, the Berry phase can be written as the flux of the curl of the Berry connection.

$$\gamma_n = \oint_c d\mathbf{R} \cdot A_n(\mathbf{R}) = \int_S (\Delta_{\mathbf{R}} \times A_n(\mathbf{R})) \cdot d\mathbf{S} = \int_S \Omega_n(\mathbf{R}) \cdot d\mathbf{S} \quad (2.3-21)$$

where

$$\Omega_n(\mathbf{R}) = \Delta_{\mathbf{R}} \times A_n(\mathbf{R}) \quad (2.3-22)$$

is the Berry curvature of the n^{th} band and is a gauge-invariant quantity. The magnetic vector potential and magnetic field are analogous the Berry connection and curvature, respectively, as they have the same mathematical relationship between them.

The Aharonov-Bohm effect is a phenomenon where a charged particle is affected by an electromagnetic field, even in regions where both the electric and magnetic fields are zero. In quantum mechanics, the Berry formalism and its geometrical phase can be realized through the analogy of the Aharonov-Bohm effect. In the Aharonov-Bohm effect, the electrons acquire a phase shift even when traveling outside of the solenoidal region where there is no magnetic field [67]. Both phenomena describe how a system acquires a phase shift due to its geometrical path through a parameter space and independent of the dynamic properties of the system.

Furthermore, Equation 2.3-21 closely resembles the principles of Cauchy's Residue Theorem. Cauchy's Residue Theorem states that the integral of a function over an oriented closed contour in the complex plane equals the sum of the residues enclosed. Similarly, the integral of the Berry curvature over a close surface of the Brillouin zone must be an integer multiple of 2π . This integer multiple, known as the Chern number C_n is defined as

$$C_n = \frac{1}{2\pi} \int_{BZ} \Omega_n(\mathbf{k}) d\mathbf{k} \quad (2.3-23)$$

and is a topological invariant representing the global geometrical properties of the band structure. The Chern number for a single band is well defined only if there exists a local gap in energy $|E_n(\mathbf{k}) - E_{n+1}(\mathbf{k})| > 0$. When electronic bands are degenerate at some subset of points in the Brillouin zone, then the Chern number given by Equation 2.3-23 is not well-defined for any of those bands. The Nielsen-Ninomiya theorem [68] dictates the sum of Chern numbers should be zero in the 1st Brillouin zone.

The integral quantum Hall effect (QHE) was discovered in 1980, in which the quantization of transverse electric Hall resistance R_H was measured in 2D electronic gas as a function of the applied magnetic field [1]. The QHE is the first experimental evidence of invariant properties of topologically ordered systems in solid-state physics. Here, the transverse current is characterized by a quantized conductivity given as

$$\sigma_{xy} = \frac{e^2}{2\pi\hbar} I(C_n) \quad (2.3-24)$$

where $I(C_n)$ is the Chern number defined in Equation 2.3-23. Thus, the Hall conductivity is a Chern number, an integer that cannot vary continuously. It is, therefore, invariant under small changes of the Hamiltonian. Large deformations can lead to energy level crossings, which are the transitions to other Chern numbers.

In 2005, Kane and Mele proposed a quantum spin Hall effect (QSHE) in graphene, where the induced spin-up and spin-down 1D edge states exhibit chiral and anti-chiral type integer quantum Hall effect due to strong spin-orbit coupling, even in the absence of an external magnetic field [69]. Due to the lack of strong spin-orbit coupling, it is impossible to observe the QSHE in graphene. But evidence for the effect exists in (Hg, Cd)Te quantum wells [70], as predicted by Bernevig et al. [71]. Recently, many quantum materials have shown evidence for the QSHE, such as monolayers of WTe₂, MoSe₂ and WSe₂ [72–74]. This new phase of material is known as the 2D Topological Insulator.

The general mechanism for topological insulators is band inversion, in which the order-

ing of the odd parity conduction band and even the parity valence band is inverted by spin-orbit coupling. A three-dimensional topological insulator can be understood as an extension of its two-dimensional counterpart and is characterized by an insulating bulk with metallic states on its surface. These surface states exhibit linear crossings at specific points in momentum space due to the band inversion that is protected by crystal symmetry. Angle-resolved photoemission spectroscopy (ARPES) experiment showed that $\text{Bi}_x\text{Sb}_{1-x}$ is the first three-dimensional topological insulator that hosts these exotic surface states [75]. In contrast to graphene, which exhibits two band crossing points with spin degeneracy, the surface of a topological insulator is characterized by a single Dirac point without any spin degeneracy.

2.4 Topological Semimetals

Following the discovery of 3D topological insulators with an insulating bulk, research was more focused on finding topologically non-trivial gapless metallic or semimetallic phases of materials. In 2014, Liu et al. experimentally discovered a 3D analog of graphene using ARPES measurements [76] that has linear band crossing in the bulk with Dirac fermions as low-energy excitations, known as the Dirac semimetal (DSM). The next year, another new class of topological materials was discovered using ARPES measurements, which is known as the Weyl semimetal [77]. The Weyl semimetal comprises linear dispersing bands but obeys a two-component Dirac equation. Weyl semimetals (WSMs) host Weyl quasiparticles as their low-energy excitation and also exhibit unclosed surface states in k -space known as Fermi arcs.

In Weyl semimetals (WSMs) and Dirac semimetals (DSMs), bulk topological bands originate from band inversion, where the conduction and valence bands touch even under spin-orbit coupling. However, in topological insulators (TIs), this interaction opens up a gap with the metallic surface state, as illustrated in Figure 2.4a. The DSM preserves both inversion symmetry (P) and time-reversal symmetry (T), leading to the DSM. Dirac points

with doubly degenerate bands. The WSM requires either inversion symmetry or time-reversal symmetry to be broken, which splits the doubly degenerate linear dispersing bands into two Weyl nodes with opposite chirality as shown in Figure 2.4c.

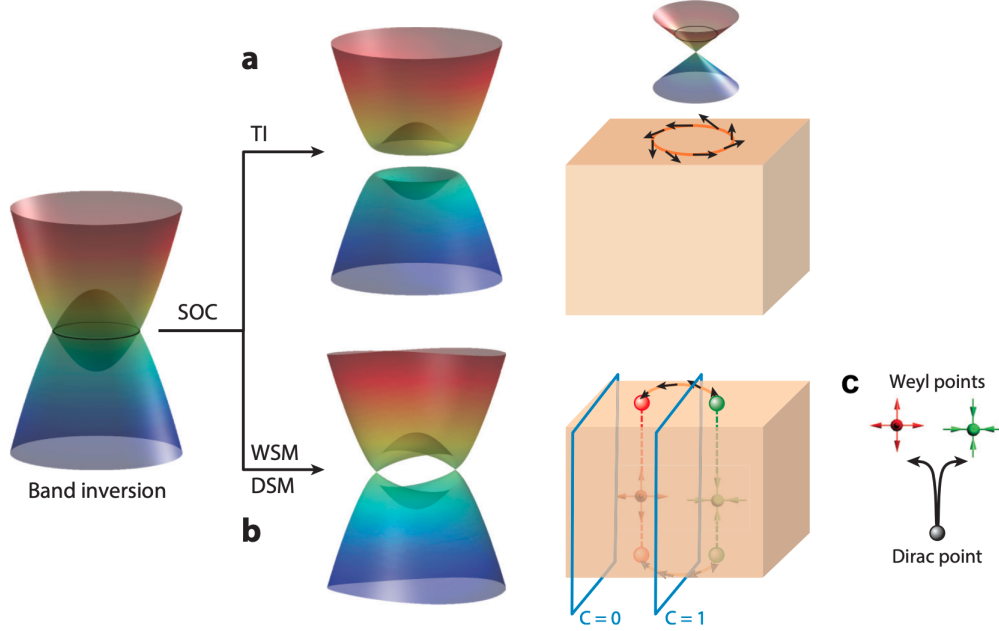


Figure 2.4: 3D topological matter (a) topological insulator opens a full gap after spin-orbit coupling (SOC) with metallic surface state (b) Dirac/Weyl semimetals gapped by the SOC except at some linearly crossing point and form Dirac/Weyl points and form the Fermi arc. (c) A Dirac point hosts the two Weyl nodes of opposite chirality. Figure taken from Ref. [78].

2.5 Weyl Semimetals

Weyl semimetals host two opposite chiral massless quasiparticles. The dynamics of such quasiparticles can be described by the Hamiltonian proposed by Hermann Weyl in 1937 in which the mass term of the Dirac equation is set to zero, which is given as

$$H_{\pm}(\mathbf{k}) = \pm v_F(\mathbf{k} - \mathbf{k}_0) \cdot \boldsymbol{\sigma} \quad (2.5-25)$$

where v_F is the Fermi velocity and $\boldsymbol{\sigma} = (\sigma_x, \sigma_y, \sigma_z)$ is the vector of the Pauli matrices

$$\sigma_x = \begin{pmatrix} 0 & 1 \\ 1 & 0 \end{pmatrix}, \sigma_y = \begin{pmatrix} 0 & -i \\ i & 0 \end{pmatrix}, \sigma_z = \begin{pmatrix} 1 & 0 \\ 0 & -1 \end{pmatrix}$$

The \pm sign in equation 2.5-25 represents the positive and negative chirality of Weyl fermions. An investigation of this Hamiltonian shows that a small perturbation on \mathbf{k}_0 does not create a gap at the location of Weyl points. Similarly, a perturbation on only v_F changes the slope of the dispersion. The solution of the Weyl Hamiltonian is left and right-handed spinors, each of which has the general form:

$$\psi(\mathbf{r}, t) = \begin{pmatrix} \psi_1 \\ \psi_2 \end{pmatrix} = \chi e^{-i(\mathbf{k}\cdot\mathbf{r} - \omega t)} \quad (2.5-26)$$

which represent Weyl fermions with different chirality. These particles have not yet been realized in the standard model.

The Berry curvature of the Weyl Hamiltonian was used to obtain the relation [79]

$$\Omega(\mathbf{k}) = \pm \frac{\mathbf{k}}{|\mathbf{k} - \mathbf{k}_0|^3} \quad (2.5-27)$$

This relation requires that the Berry curvature must have singularities at the Weyl points. This implies that the WPs serve as sources and sinks of Berry curvature and must correspond to a nonzero Berry phase. They have non-zero Chern numbers and, therefore, must be topologically protected.

ARPES measurement can directly observe these band crossings at the Weyl nodes. Materials belonging to the same family of TaAs, such as TaP, NbAs, and NbP, show evidence of linear band crossing with Weyl nodes [80]. Surface Fermi arch was also observed using ARPES measurement in these materials [81].

2.5.1 Type-I and type-II Weyl Semimetal

In the TaAs family of Weyl semimetals which belong to space group 109, the Fermi surface at the Weyl node is point-like. The linear dispersing bands form a 3D cone that is perpendicular to the Fermi surface, and in the vicinity of the Weyl node, the energy difference between the conduction band and valence band changes linearly with momentum as shown in Figure 2.5a. However, Soluyanov et al. introduced a new type of Weyl node in WTe₂ [82], which has Weyl fermions emerging at the boundary between the electron and hole pockets. They named the former configuration Type-I WSM, while the latter is Type-II which is shown in Figure 2.5.

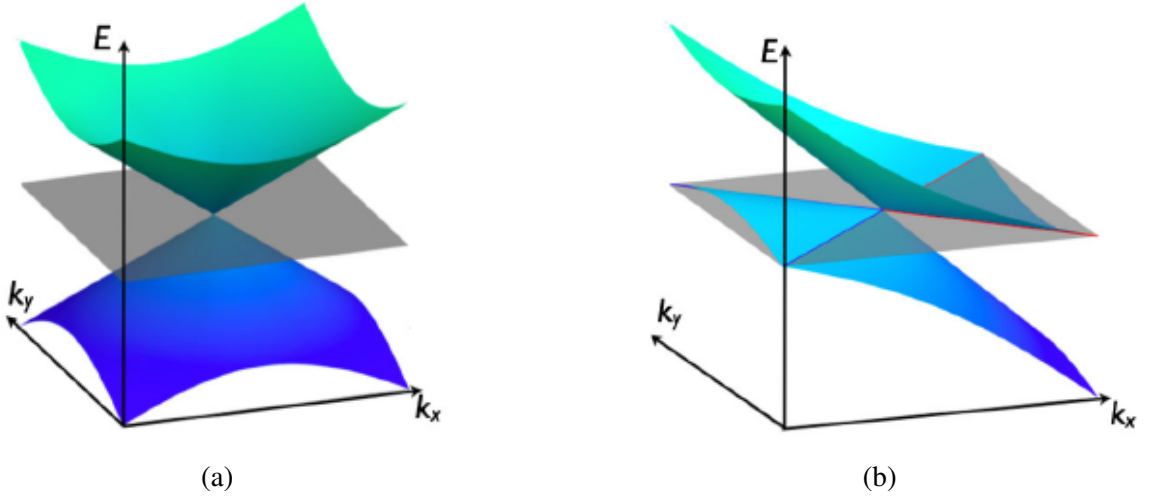


Figure 2.5: (a) Type-I and (b) type-II Weyl nodes with tilting Weyl nodes. Figure taken from Ref. [82].

The most general Hamiltonian of a Weyl point linear in \mathbf{k} can be written as [83],

$$H_{\pm}(\mathbf{k}) = E_0(\mathbf{k}_0) + \mathbf{v}_0 \cdot (\mathbf{k} - \mathbf{k}_0) + \sum_{i,j=x,y,z} v_{ij}(\mathbf{k} - \mathbf{k}_0)_i \sigma_j \quad (2.5-28)$$

where $\sigma_{x,y,z}$ are Pauli matrices and v_0 and v_F characterize the band dispersion near the touching points.

The eigenvalues of Equation 2.5-28, ignoring the constant term, are

$$\varepsilon_{\pm} = \mathbf{v}_0 \cdot \delta \mathbf{k} \pm \sqrt{\sum_{i,j=x,y,z} \delta k_i (v v^T) \delta k_j}, \quad \delta \mathbf{k} = \mathbf{k} - \mathbf{k}_0 \quad (2.5-29)$$

$$= T(\delta \mathbf{k}) \pm U(\delta \mathbf{k}) \quad (2.5-30)$$

where, $T(\delta \mathbf{k})$ and $U(\delta \mathbf{k})$ are the kinetic and potential components of the energy spectrum, respectively. Applying the classification to Equation 2.5-29, we can recover both possible types of Weyl points from this dispersion relation. Moreover, $T(\delta \mathbf{k}) > U(\delta \mathbf{k})$ is the condition for type-II WSM where two bands overlap in energy yielding electron and hole pockets around the Weyl point. Since the formation of the Weyl point is different, the Weyl cone for type-II is tilted, as shown in Figure 2.5b, even though it is still linearly dispersing.

The T_d phase of the TMD MoTe_2 hosts strong Type-II Weyl nodes [84], in which one node is located 6 meV and another 59 meV above the Fermi level. This large separation makes it easy to observe the nodes and the surface band structure by ARPES measurements [84]. Later, type-II nodes were observed in rare-earth-based Weyl semimetal LaAlGe and $\text{Mo}_x\text{W}_{1-x}\text{Te}_2$ alloys [85]. The tilt of the Weyl cone leads to specific transport properties, such as a chiral anomaly associated with unusual magnetoresistance [15]. It will also support a modified anomalous Hall effect [86], and new quantum oscillations due to momentum Klein tunneling [87].

2.6 Recent Nonlinear Experimental Study on Weyl Semimetal

Due to their unique electronic structure, both Type-I and Type-II Weyl semimetals can exhibit strong nonlinear effects, such as SHG [88], photogalvanic effect [89] and nonlinear Hall effect [13]. In this thesis, we will focus only on the SHG and photocurrent measurement.

2.6.1 SHG in Weyl Semimetals

A suitable theoretical approach to studying the topological nature of nonlinear optical effects was introduced in 2016 using the Floquet formalism link with the Berry formalism and observed that SHG enhanced at the exciton resonance [90]. In the same year, an experimental study observed unusually strong SHG in the Weyl semimetal TaAs, which is about an order of magnitude larger than that of the well-known strong and robust SHG response material GaAs [88]. However, a later study on TaAs has shown that this large response is due to a resonance effect along the polar axis of the materials along with a large third cumulant of the Bloch wavelength [91]. Thus, it is not a topological effect. Recently, SHG has been studied on the multifold semimetal RhSi, where the response is suppressed by the linear band crossing in the BZ indicating that Weyl topological band structures are, in fact, antagonistic to SHG at all but the lowest frequencies rather than enhancing SHG [92].

Although generally only non-centrosymmetric materials generate the SHG signal, SHG has been theoretically studied in the inversion symmetric magnetic Weyl semimetal $\text{Co}_3\text{Sn}_2\text{S}_2$ under DC current and THz pump since both can serve to break inversion to allow bulk SHG [93]. In the former experiment strength of the induced SHG is about the same order of magnitude as SHG in GaAs; however, with THz pump, it is 10^3 times larger than GaAs and 10^2 times larger than TaAs. Beyond the ED SHG, electric quadrupole SHG (EQ-SHG) has also been studied in $\text{Co}_3\text{Sn}_2\text{S}_2$ to reveal a magnetic phase transition at 175 K, which is due to ferromagnetic order, and another transition at 120 K, which is due to antiferromagnetic order [94].

SHG has also been studied in the type-II Weyl semimetals MoTe_2 and WTe_2 using ultrafast pump-probe and time-resolved second-harmonic-generation spectroscopy [95, 96]. In MoTe_2 , the SHG revealed the presence of a phase transition through a change in the intensity of the response, while in WTe_2 , it was used to experimentally verify a structural transition from a topologically ordered phase to a topologically trivial phase [97]. The magnetic Weyl semimetal, CeAlSi , shows the evidence of directionally dependent SHG

intensity at low temperatures known as the nonlinear optical diode effect [98].

All of these studies on SHG in Weyl semimetals have focused on two-photon absorption via ED transitions, with MD transitions remaining largely unexplored. This motivates our study of SHG in Weyl semimetals, where we investigate two-photon absorption attributed to MD transitions alongside ED transitions in the rare earth family of Weyl semimetals, as described in Chapter 5.

2.6.2 Photocurrent in Weyl Semimetals

The generation of electrical current in response to light, known as photocurrent, has been the subject of various theoretical investigations [99], particularly in Weyl semimetals and other materials lacking inversion symmetry [100]. Particularly relevant are the shift current/linear photogalvanic effect (LPGE) and the injection current/circular photogalvanic effect (CPGE).

The first topological material predicted to support CPGE/LPGE is in Bi_2Se_3 [101], where it was realized that the current due to interband transition at momentum k was proportional to the Berry curvature. In these experiments, a photon with definite helicity induced a transition that flipped the direction of spin and, through spin-momentum locking, created a particle-hole pair that carried a net current. Later, de Juan et al. showed the evidence that CPGE may depend on only the topological charge and fundamental constant [102], i.e., independent of material-specific properties and the frequency of the excitation of light over a band of wavelengths. Although theoretically, quantized CPGE exists only in idealized, non-interacting Weyl systems, WSMs can still realize large helicity-dependent photocurrents, these were measured by Rees et al. [102]. Further research examining the CPGE/LPGE in a range of Weyl Semimetals such as TaAs and TaIrTe₄ has uncovered behavior dependent on helicity linked to the chirality of the Weyl nodes [89, 103].

Besides the bulk CPGE, the surface of the Weyl semimetal also provides the photogalvanic effect. Chang et al. [104] theoretically studied the photocurrent from RhSi surface Fermi arcs which are typically transverse to the propagating excitation beam due to the nonsymmorphic nature of space group 198 compounds. This effect was experimentally studied using THz emission photogalvanic effect spectroscopy, where measurement revealed an emergent mirror symmetry inconsistent with the chiral structure of the crystal [105].

2.7 Weyl Semimetals- LnAlSi and PdGa

In this section, we will outline some basic details of two Weyl semimetals studied here, LnAlSi (Ln = La , Ce , Pr and Nd) and PdGa.

2.7.1 LnAlSi

LnAlSi is noncentrosymmetric, belonging to the space group 109 ($I4_1md$), i.e., the same space group as the first experimentally observed Weyl semimetal TaAs. The tetragonal unit cell and the first BZ with a high symmetry point and mirror planes of NdAlSi are shown in Figures 2.6a and 6.5a. NdAlSi has two mirror planes m_x and m_y , and two glide mirror planes, m_{xy} and $m_{x\bar{y}}$, but site mixing between the Al and Si atom restore the glide plane symmetry and change to the centrosymmetric space group 141 ($I4_1/amd$). The second harmonic generation (SHG) is only allowed in non-centrosymmetric materials, so we used the SHG probe to identify whether the mixing between the Al and Si atoms is present or not. Our experimental data for SHG measurement for all LnAlSi family of Weyl semimetal is presented in Chapter 5.

The first-principles band structure of structural analog PrAlGe in its ferromagnetic phase is shown in Figure 2.6d with red (blue) for the spin up (down) with the Weyl node near the Fermi energy level. Rare earth atoms occupy the specific lattice points within the tetragonal structure, maximizing their interaction with Al and Si atoms and carrying an in-

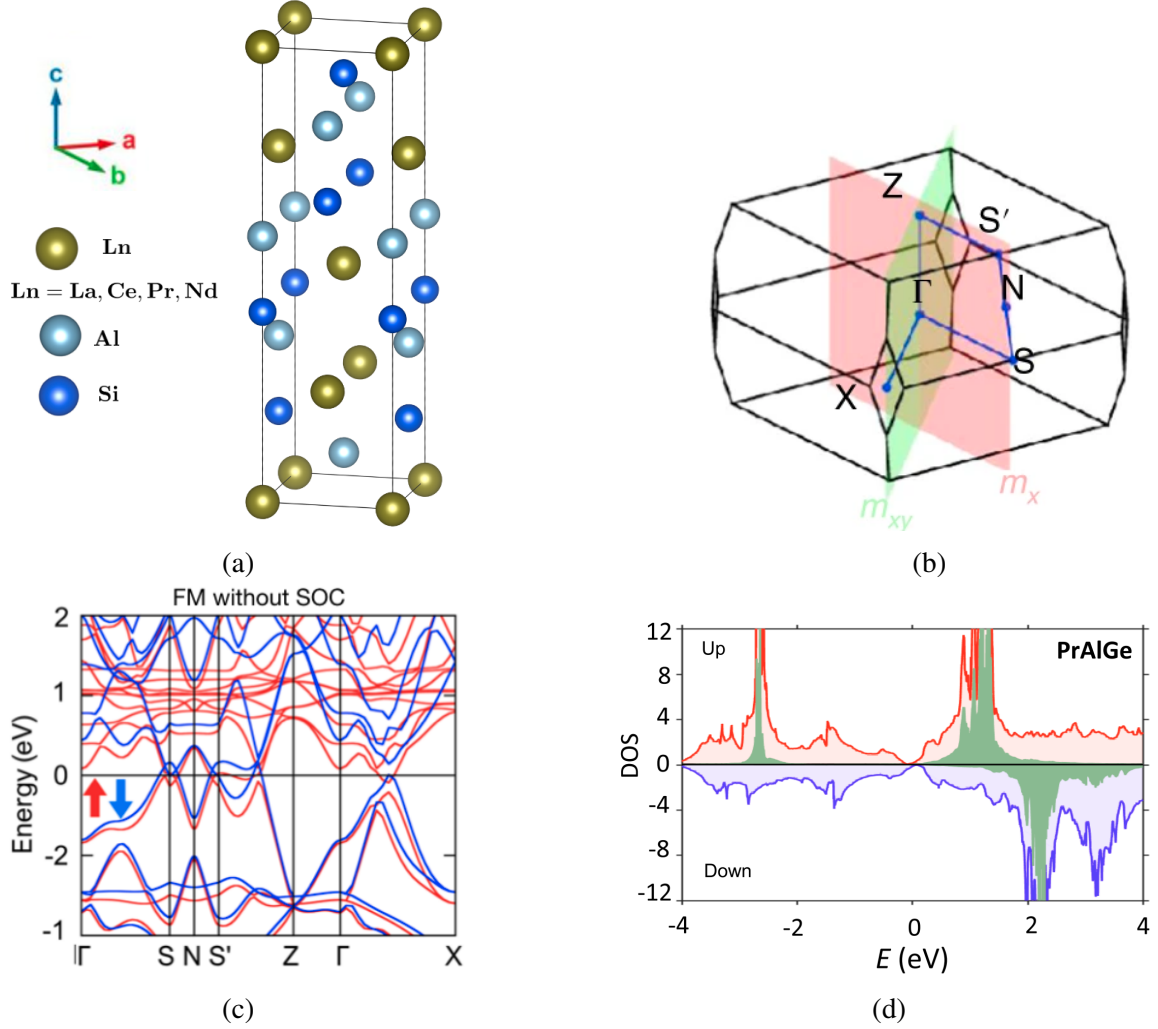


Figure 2.6: Crystal and band structure of LnAlSi and DOS for PrAlGe. (a) Crystal structure of LnAlSi. (b) First Brillouin zone of NdAlSi with mirror planes. (c) Band structure of NdAlSi from first-principles calculations with Paramagnetic state in the PBE approximation (d) The partial DOS for PrAlGe, closely related material with LnAlSi, spin-up, and spin-down states are plotted in red and violet colors, respectively. The DOS from localized f - orbitals are in green. Figures taken from Ref. [106, 107].

trinsic f -electron magnetic moment. The LaAlSi hosts both type-I and type-II Weyl nodes and supports the various topological phenomena arising from the Weyl fermions, such as the large spin Hall effect [16]. LaAlSi is nonmagnetic semimetal due to it does not have an f electron in its trivalency. As a class, these materials host various forms of magnetic order, such as canted magnetic ordering in CeAlSi at a temperature of 8.2 K with a nontrivial magnetic domain wall [108]. Also, ARPES measurement shows evidence of tunable Weyl

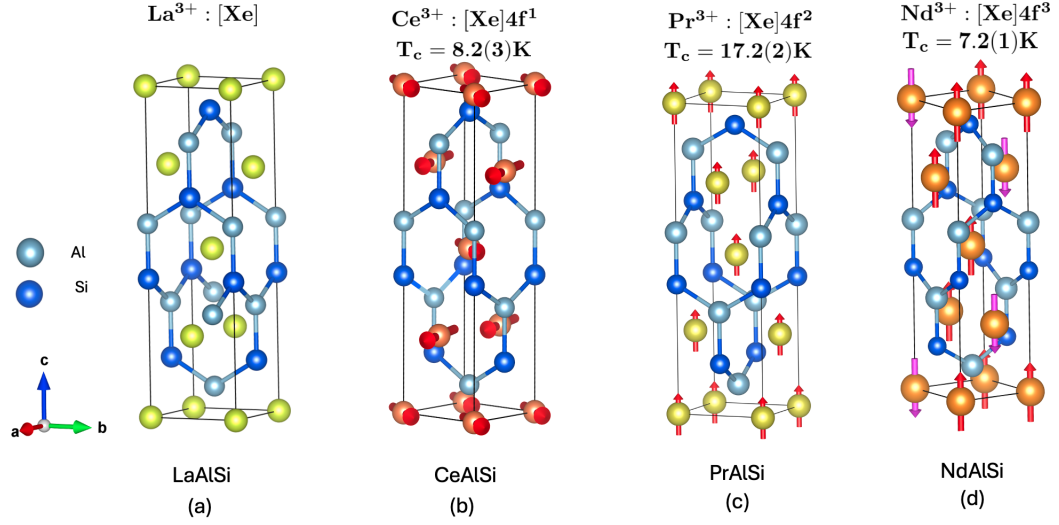


Figure 2.7: Magnetic order in LnAlSi materials with their transition temperatures (a) no magnetic order in LaAlSi, (b) canted AFM order in CeAlSi [108], (c) FM order in PrAlSi [110], and (d) spin density wave order in NdAlSi [107].

nodes with external magnetic field and pressure [109]. Strong local-moment, out-of-plane ferromagnetic ordering has been observed in PrAlSi at 17.2 K as shown in Figure 2.7c, which also exhibits an anomalous Hall effect [110]. The spin density wave ordering at 7.2 K in NdAlSi is shown in Figure 2.7d. The magnetic behavior in these materials mainly derives from f -orbitals, which are linked to the rare earth ions in their trivalent state.

The LnAlSi family of WSMs also shows evidence of strong nonlinear and quantum effects. The partial DOS for PrAlGe, shows that localized f -orbital are found below and above the Fermi level. The semimetal CeAlSi shows nonlinear optical diode effect [98] and anisotropy Fano resonance in LaAlSi in phonon modes measured by Raman Scattering [55].

2.7.2 PdGa

The crystal structure of PdGa is cubic in the space group 198 ($P2_13$) with lattice constant $a = 4.9 \text{ \AA}$. The cubic unit cell of PdGa having eight Pd atoms at the corner and one Ga atom at the center is shown in Figure 2.8a. Figure 2.8b shows the band structure of PdGa in which Weyl nodes are at the high symmetry points Γ , and R. Both Weyl nodes

lie below the Fermi surface and are separated by ~ 0.45 eV [111]. This offset in energy is due to the structural chirality. This material has higher pseudospin generation of Weyl semimetal due to the fact that more than two bands cross, pseudospin-3/2 fermions were observed near the Γ point and double pseudospin-1 fermions at the R point. Thus, this is a topological multifold fermion with Chern number 4 at the crossing nodes.

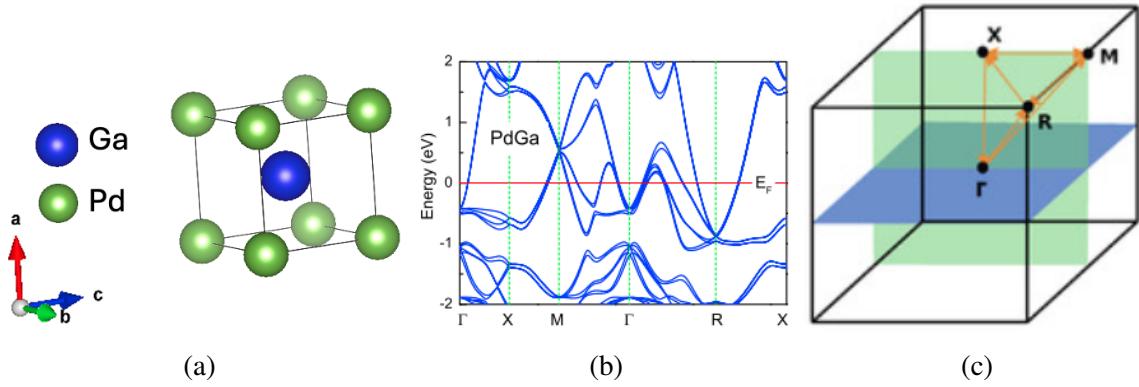


Figure 2.8: PdGa (a) unit cell (b) band structure (c) BZ with high symmetry points. Figure taken from Ref. [112].

The BZ with a high symmetry point is shown in Figure 2.8c. The enantiomers of PdGa have the same band structure and BZ. ARPES and STM measurements on enantiomers of PdGa showed the opposite helicity of Fermi arc dispersion. In Chapter 7, we will discuss the nonlinear photogalvanic effect on enantiomers of PdGa and the effect of structural chirality on the response.

CHAPTER 3

CHARGE DENSITY WAVE IN TRANSITION METAL DICALCOGENIDE 1T – TiSe₂

3.1 Brief Introduction to Charge Density Wave Physics

The Charge Density Wave (CDW) is a phenomenon that arises from the interplay between the electronics and the lattice [113]. It is characterized by a periodic distortion of the lattice, leading to a modulation of the charge density. In this phenomenon, the system minimizes its energy due to the reconstruction of the electronic structure, which Peierls [114] and Frohlich [115] first proposed for a 1D free electronic system in the 1950s. In Peierls picture the electrons of the 1D metals experience electron-phonon coupling at a low temperature, resulting in a periodic lattice distortion. After such a lattice distortion, the relevant conduction band gaps as the real-space charge exhibit a new charge density. The Brillion Zone is also reduced in size as the Fermi surface reconstructs.

In the 1D linear chain of atoms, the modulated electron density of $\rho(\mathbf{r})$ with periodic wave vector \mathbf{q} is given by

$$\rho(\mathbf{r}) = \rho_0 + \rho_1 \cos(\mathbf{q} \cdot \mathbf{r} + \phi) \quad (3.1-1)$$

In Equation 3.1-1, ρ_0 describes the unperturbed electron density with constant periodic lattice spacing a as shown in Figure 3.1(a), ρ_1 and ϕ are the amplitude and phase of the electron density modulation of CDW, respectively. The CDW is commensurate if $\mathbf{q} = (m/n)a$, where m/n is a rational number; otherwise, it is considered to be incommensurate.

The rearrangement of charge density can be written in terms of Fermi-Dirac distribution $f(\epsilon)$ in d dimensions as

$$\rho(\mathbf{r}) = \int \frac{d\mathbf{k}}{(2\pi)^d} [f(\epsilon_{\mathbf{k}}) + f(\epsilon_{\mathbf{k}+\mathbf{q}})] + \int \frac{d\mathbf{k}}{(2\pi)^d} \frac{f(\epsilon_{\mathbf{k}}) - f(\epsilon_{\mathbf{k}+\mathbf{q}})}{\epsilon_{\mathbf{k}} - \epsilon_{\mathbf{k}+\mathbf{q}}} \phi(\mathbf{q}) \quad (3.1-2)$$

where $\phi(\mathbf{q})$ is the time-independent potential. The second term can be written in the form of the Lindhard response function $\chi(\mathbf{q})$ with,

$$\chi(\mathbf{q}) = \int \frac{d\mathbf{k}}{(2\pi)^d} \frac{f_{\mathbf{k}} - f_{\mathbf{q}+\mathbf{k}}}{\epsilon_{\mathbf{k}} - \epsilon_{\mathbf{q}+\mathbf{k}}} \quad (3.1-3)$$

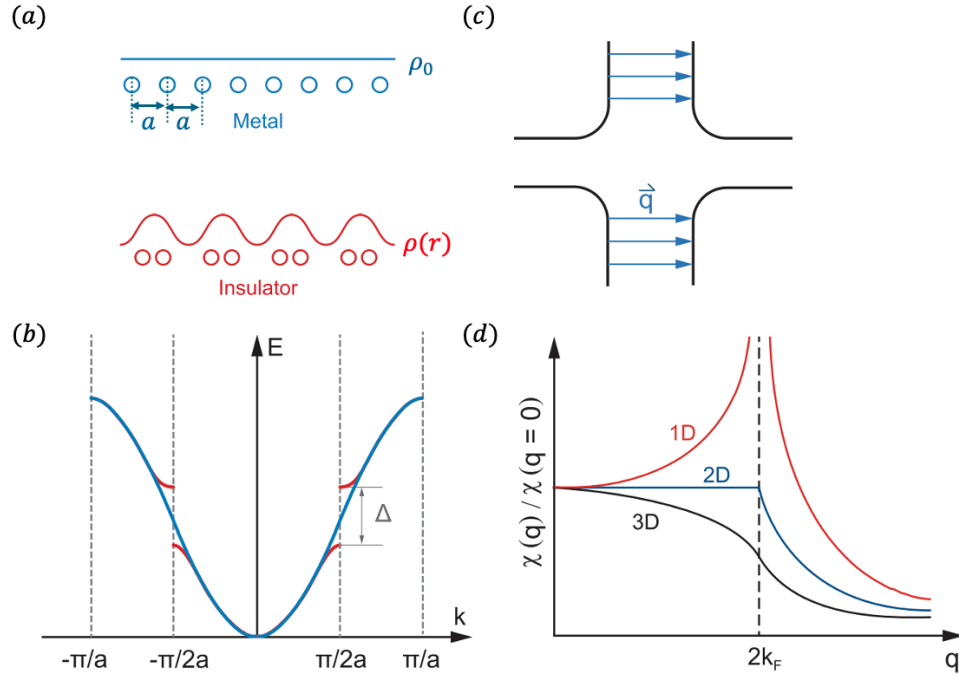


Figure 3.1: (a) Schematic representation of a Peierls transition in a one-dimensional material, blue (red) represents the system before (after) the Peierls transition. (b) A gap Δ opens up at the wavevector $\mathbf{q} = 2\mathbf{k}_F$ corresponding to the new lattice periodicity with dispersion before (after) the Peierls transition. (c) An illustration of Fermi surface nesting with a wavevector \mathbf{q} . (d) The Lindhard response function $\chi(\mathbf{q})$ as a function of wavevector \mathbf{q} for one, two, and three-dimensional free electron gases. Figure taken from Ref. [116].

In a CDW, large regions of the Fermi surface can be perfectly or nearly perfectly mapped onto each other by so-called “nesting” wave vectors, as shown in Figure 3.1(b).

The susceptibility Lindhard function response at the Fermi nesting vector also shows a discontinuity at this value of \mathbf{q} . In a 1D system with large regions of the Fermi surface nested by a wavevector $\mathbf{q} = 2\mathbf{k}_F$, i.e., $\epsilon_k = \epsilon_{k+2k_F}$ and the denominator of Equation 3.1-3 vanishes resulting in a divergence, as shown in Figure 3.1(b). This indicates that the electronic structure is not stable, and small perturbation will cause a charge density redistribution with Fermi surface reconstruction. Most importantly, periodic lattice modulation can overcome the Coulomb repulsion by lowering the energy of the system as a gap opens at the Fermi level. The lattice distortion drives the conduction electrons' density periodic modulation to maintain charge neutrality and form a CDW, as shown in Figure 3.1(c). Because the Fermi surface gaps, as shown in Figure 3.1(d), the 1D Peierls transition is accompanied by a metal-to-insulator/semiconductor transition. The first evidence of a Peierls distortion was observed at room temperature in the one-dimensional conductor $\text{K}_2\text{Pt}(\text{CN})_4\text{Br}_{0.30} \cdot x\text{H}_2\text{O}$ using X-ray diffuse scattering [117].

The Peierls transition can also be applied to higher dimensions. The first evidence for a CDW in transition metal dichalcogenides (TMDs) was reported in 1976 in NbSe_3 , which was observed through enhanced electrical conduction at increased electric fields [118]. Later on, many TMD materials such as 2H-TaS₂ [119], 2H-NbSe₂ [120], 1T-TaSe₂ [121], 1T-TaS₂ [122] were discovered to show evidence of a CDW instability, which were experimentally verified by new experimental techniques such as X-ray diffraction, neutron scattering and scanning tunneling microscopy.

The electron-phonon coupling driven Peierls transition in a one-dimensional system was originally considered the only mechanism for CDW formation. However, the existence of a pseudogap in NbSe_3 above the highest known Peierls transition temperature suggests the presence of other driving mechanisms [123]. In complex 2D and 3D systems, alternative driving mechanisms [22] and even multiple competing effects have been observed to be responsible for the formation of CDW. These alternative mechanisms are excitonic instability [124] and the Jahn-Teller effect [125]. In TMDs, many materials show a CDW

at low temperatures, but the microscopic mechanism behind them varies from system to system.

3.1.1 Excitonic Instability

An excitonic instability refers to a state in condensed matter physics where a system becomes unstable due to the formation of bound states of electrons and holes known as excitons. When the temperature decreases, there is a drop in the population of thermally excited electrons and their corresponding holes, leading to insufficient screening to prevent the formation of bound states; consequently, as the free electrons diminish completely, the material transitions into an insulator. In 1976, D. Jerome initially introduced the theoretical idea of a phase transition instability driven by exciton formation in semimetals or semiconductors characterized by a very small or even negative band gap [126].

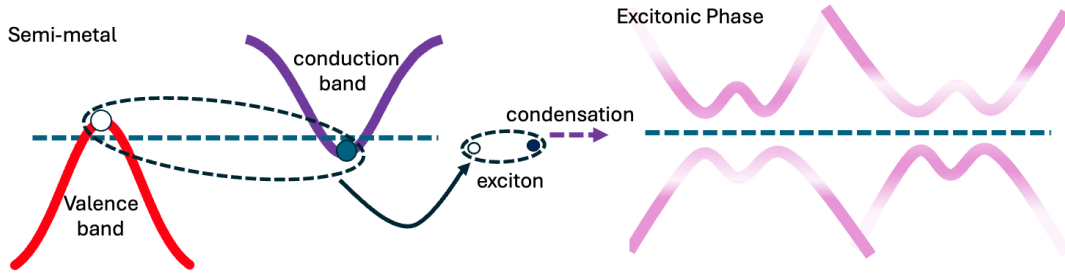


Figure 3.2: Figure for excitonic instability where electrons and holes form bound states and undergoes Bose-Einstein condensation.

The Hamiltonian for a semimetal system with Coulomb attraction $V(q)$ between the electron and hole at valence and conduction band separated by \mathbf{Q} in momentum space is,

$$H = \sum_{\mathbf{k}} \varepsilon_h(\mathbf{k}) a_{\mathbf{k}}^{\dagger} a_{\mathbf{k}} + \sum_{\mathbf{k}} \varepsilon_e(\mathbf{k}) b_{\mathbf{k}}^{\dagger} b_{\mathbf{k}} + \frac{1}{N} \sum_{\mathbf{k}, \mathbf{k}', q} V(q) b_{\mathbf{k}+q}^{\dagger} b_{\mathbf{k}} a_{\mathbf{k}'-q}^{\dagger} a_{\mathbf{k}'} \quad (3.1-4)$$

where the momentum space potential is given by

$$V(q) = \frac{4\pi e^2}{\eta(q)q^2} \quad (3.1-5)$$

In Equation 3.1-5, $\eta(q)$ is an effective dielectric constant. a_k (a_k^\dagger) and $\varepsilon_h(\mathbf{k})$ are the creation (annihilation) operators and energy dispersion respectively for the hole at the valence band, while b_k (b_k^\dagger) and $\varepsilon_e(\mathbf{k})$ are the creation (annihilation) operators and energy dispersion respectively for the electrons in the conduction band.

For simplicity, we assume the same effective mass of electrons and hole, i.e., $m_h = m_e = m$. The single-particle hole $\varepsilon_h(\mathbf{k})$ and $\varepsilon_e(\mathbf{k})$ energies can be written as

$$\varepsilon_h(\mathbf{k}) = -\frac{G}{2} + \frac{\mathbf{k}^2}{2m}, \quad \varepsilon_e(\mathbf{k}) = \frac{G}{2} - \frac{(\mathbf{k} - \mathbf{Q})^2}{2m} \quad (3.1-6)$$

where G is the energy gap. $G > 0$ indicates a system is semiconductor and $G < 0$ indicates a system is semimetal. For further simplification, let's assume $\mathbf{Q} = 0$, i.e., there is a direct band gap. In a semimetal, the valence and conduction bands cross, at Fermi momentum k_F i.e., $\varepsilon_h(\mathbf{k}_F) = \varepsilon_e(\mathbf{k}_F)$ using this in Equation 3.1-6, we obtain

$$\varepsilon = \varepsilon_h(\mathbf{k}) = \varepsilon_e(\mathbf{k}) = \frac{\mathbf{k}_F^2}{2m} - \frac{\mathbf{k}^2}{2m} \quad (3.1-7)$$

The gap parameter of the exciton condensation state is defined as [127],

$$\Delta(k) = -\frac{1}{\Omega} \sum V(\mathbf{k} - \mathbf{k}') \langle b_{\mathbf{k}'}^\dagger a_{\mathbf{k}} \rangle \quad (3.1-8)$$

In this equation, Coulomb interaction can be written in terms of screening parameter κ due to both electron and hole,

$$V(k) = \frac{4\pi e^2 / \eta}{\mathbf{k}^2 + \kappa^2}, \quad \kappa^2 = \frac{2m e^2}{\pi \varepsilon} k_F \quad (3.1-9)$$

From the Bogoliubov transformation [128] and Equation 3.1-8, the gap equation of the excitonic phase is given by,

$$\Delta(k) = \int V(k-k') \frac{\Delta(k')}{2E_{k'}} \tanh\left(\frac{\beta E_k}{2}\right) \frac{dk'}{(2\pi)^3} \quad (3.1-10)$$

$$\beta = K_B T \text{ and } E'_k = \sqrt{\left(\frac{\epsilon(k')_e + \epsilon(k')_h}{2}\right)^2 + \Delta(k')^2} \quad (3.1-11)$$

A non-zero value for self-consistent solutions of Equation 3.1-10 indicates the emergence of the excitonic phase. The function $\Delta(k)$ induces a hybridization gap between the valence and conduction bands, resulting in the system being either an insulator or a semiconductor. The STM and X-ray diffraction techniques in materials such as Sb(110) nanoflakes [129] and HfTe₂ [130] show evidence for a purely electronic origin of their CDW rather than a lattice-based origin. The two-dimensional material 1T-TiSe₂ also follows this excitonic phase instability due to the hole in the valence band near the center of BZ forming a bound state with the electron at the edge of the BZ, which will be discussed later in this Chapter.

3.1.2 Jahn-Teller Effect

Jahn-Teller effect occurs in electronically degenerate states in polyatomic systems where the nonlinear symmetrical nuclear configuration is unstable. As a result of this instability, the nuclei displace themselves to break the configuration's symmetry and lift the electronic degeneracy [131].

Let us assume that q_v and Q_α are the electronic and nuclear coordinates with $V(q_v, Q_\alpha)$ as the electron-nuclei interaction operator. Let the nuclei be displaced by a small displace-

ment from symmetric configuration $Q_{\alpha o}$. The small perturbation can be considered as

$$\delta V = V(q_V, Q_\alpha) - V(q_V, Q_{\alpha o}) \quad (3.1-12)$$

$$= \sum_{\alpha} \left(\frac{\partial V}{\partial Q_{\alpha}} \right) (Q_{\alpha} - Q_{\alpha o}) + \frac{1}{2} \sum_{\alpha, \beta} \left(\frac{\partial^2 V}{\partial Q_{\alpha} \partial Q_{\beta}} \right) (Q_{\alpha} - Q_{\alpha o})(Q_{\beta} - Q_{\beta o}) + \dots \quad (3.1-13)$$

For a f -fold degenerate electronic state, we obtain a f -rank secular equation

$$||V'_{ij} - \epsilon' \delta_{ij}|| = 0, i, j = 1, 2, \dots, f \quad (3.1-14)$$

from which the f roots $\epsilon'_k(Q_\alpha)$ can be obtained. By considering the atomic core interaction to be approximated by the harmonic term $\frac{1}{2} \sum_{\alpha} K_{\alpha} Q_{\alpha}^2$, the adiabatic potential can be written as,

$$\epsilon_k(Q_\alpha) = \frac{1}{2} \sum_{\alpha} K_{\alpha} Q_{\alpha}^2 + \epsilon'_k(Q_\alpha), k = 1, 2, \dots, f \quad (3.1-15)$$

where K_{α} is force constant.

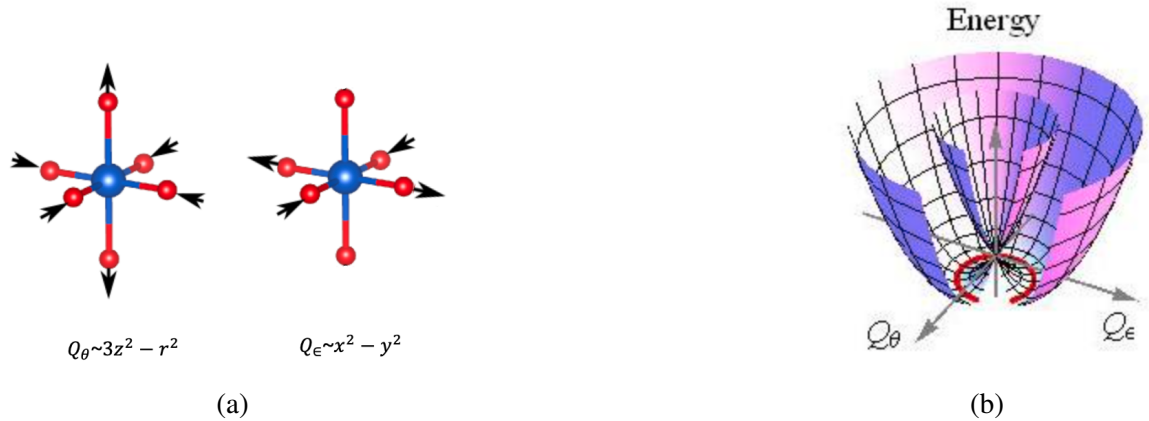


Figure 3.3: (a) Two vibrational components of the e_g mode, Q_{θ} and Q_{ϵ} , in octahedral symmetry which transform as $3z^2 - r^2$ and $x^2 - y^2$, respectively (b) The potential energy surfaces of a Jahn–Teller effect with distortions around the origin. Figure taken from [132].

Let us take a twofold degenerate e_g orbital type vibration represented by the coordinates $Q_\theta = \rho \cos(\phi)$ and $Q_e = \rho \sin(\phi)$ in a cylindrical coordinate system [In a cartesian coordinate system, the symmetry properties determined to be $3z^2 - r^2$ for Q_θ and $x^2 - y^2$ by Q_e]. Using this in Equation 3.1-14 we obtain

$$\varepsilon'_\pm(\rho, \phi) = \rho[A_1^2 + A_2^2\rho^2 + 2A_1A_2\rho \cos(3\phi)]^{\frac{1}{2}} \quad (3.1-16)$$

and adiabatic potential as;

$$\varepsilon_\pm(\rho, \phi) = \frac{1}{2}K_e\rho^2 \pm \rho[A_1^2 + A_2^2\rho^2 + 2A_1A_2\rho \cos(3\phi)]^{\frac{1}{2}} \quad (3.1-17)$$

where $A_1 = (\frac{\partial V_{\theta\theta}}{\partial Q_\alpha})_0$ and $A_2 = \frac{1}{2}(\frac{\partial^2 V_{\theta\theta}}{\partial Q_\theta^2})_0$ are the so-called linear (A_1) and second-order (A_2) vibronic coupling constants. At second order, the vibronic coupling terms are negligible, i.e., $A_2 = 0$. Thus,

$$\varepsilon_\pm(\rho, \phi) = \frac{1}{2}K_e\rho^2 \pm \rho A_1 \quad (3.1-18)$$

This equation shows that in Q_θ, Q_e coordinates, the adiabatic potential is independent of ϕ and has a rotation symmetry like the Mexican hat function shown in Figure 3.3b. The cone-like shape around the degeneracy point near the origin indicates the instability. The Jahn-Teller instability has been observed in cuprate-based superconductors such as $\text{YBa}_2\text{Cu}_3\text{O}_7$ [133] and TMDCs such as 1T-TiSe_2 [134, 135].

3.2 Transition Metal Dichalcogenides (TMDs)

TMDs are two-dimensional materials with the generic chemical MX_2 , where M is a transition metal and X is chalcogen. They consist of a transition metal layer sandwiched between two chalcogen atom layers. Depending on the stacking order, TMDs can exist in

two different structural phases. These phases are characterized by either trigonal prismatic (2H) or octahedral (1T) coordinates as shown in Figure 3.4. The 2H phases correspond to three atomic layers (chalcogen-metal-chalcogen) in which the chalcogen atoms in different atomic planes occupy the same position and are located on top of each other in the direction perpendicular to the layer. By contrast, in the 1T phase, the chalcogen atoms in the top and bottom layers are not located on top of each other. Bulk TMDs are composed of many stacking layers held together by weak van der Waals forces.

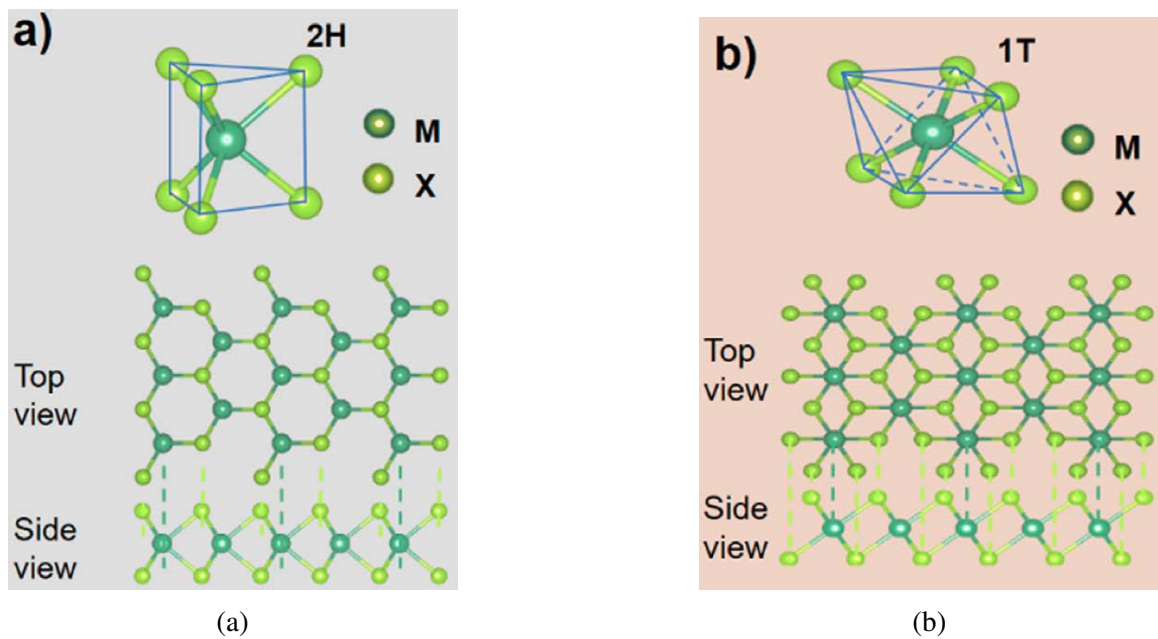


Figure 3.4: The schematic model for (a) 2H and (b) 1T phase of TMDs. Figure taken from Ref. [136]

While Linus Pauling first determined the structure of TMDs in 1923 [137], interest in them increased after the fabrication of a single atomic layer of graphene in 2004 [8]. TMDs address some limitations of graphene, such as the existence of intrinsic band gaps. TMDs exhibit a wide spectrum of electronic behavior from insulating HfS_2 , through semi-conducting WS_2 , and semimetallic WTe_2 to true metallic like NbS_2 , depending on their composition and structure [138]. TMDs are also well known for hosting collective behav-

iors such as superconductivity, spin density waves, and CDW in materials like, e.g., NbSe₂ [139], MoS₂ [140], TaS₂ [141].

In this thesis, we have studied 1T–TiSe₂, which is a layered TMD with a trigonal crystal structure that hosts the CDW phase below 200 K. Experimentally, it has been observed by transport experiments that either intercalation of Cu between layers or application of hydrostatic pressure suppresses the CDW and induces a superconducting phase at transition temperatures up to ~ 3 K [30, 142]. While not a focus of this thesis, this is a suitable material to interplay between the superconductivity and CDW phase in a single material. Here, our interest is exclusively in the CDW phase.

3.3 Overview of the Properties of 1T–TiSe₂

3.3.1 Lattice and Electronic Structure

1T–TiSe₂ is a layered material that crystallizes in a hexagonal structure with space group $P\bar{3}m1$ (No. 164). Each layer consists of a sublayer of Se–Ti–Se in which each Ti atom is coordinated by six Se atoms in an octahedral configuration. Figure 3.5b shows the first Brillouin Zone (BZ) defining the high symmetry position points.

Structurally, neutron diffraction at room temperature has obtained the lattice parameters for 1T–TiSe₂ as $a = b = 3.54$ Å and $c = 6.00$ Å [32]. The electronic band structure of 1T–TiSe₂ is shown in Figure 3.5c; the conduction band mainly comes from Se-4*p* orbitals and the valence band mainly comes from Ti-3*d* orbitals. Angle-resolved photoemission spectroscopy (ARPES) measurements have been used to explore the band gap of 1T–TiSe₂. However, due to resolution limitations, the exact energy values of the minima of the conduction band and the maxima of the valence band are not known [33]. Nevertheless, photoemission experiments by Kidd et al. have revealed a small indirect band gap [143], while measurements by Cercellier et al., as well as ab initio density functional theory calculations suggest that the system has a semimetallic nature [144, 145]. This is evidenced

by a band overlap between valence bands, which have hole-like characteristics near the Γ point, and conduction bands, which have electron-like characteristics near the L (M) point. The semimetallic phase is commonly acknowledged as the stage for investigating the CDW.

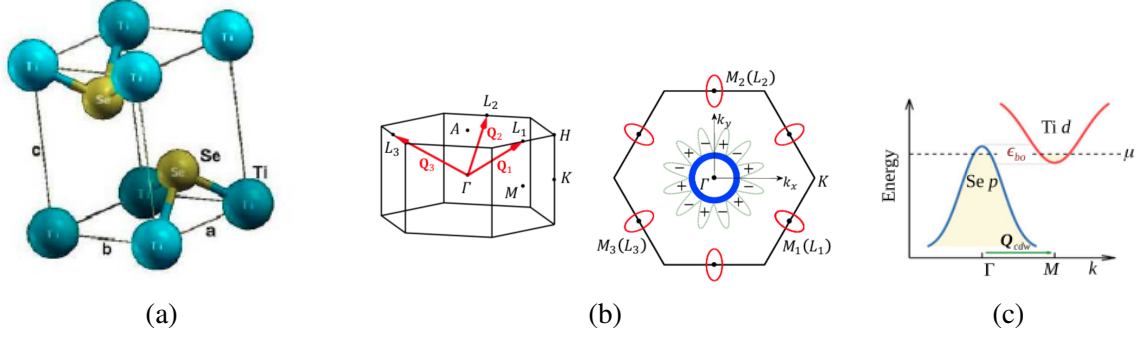


Figure 3.5: Electronic structures of 1T–TiSe₂ (a) Crystal structure (b) Brillouin zone with high symmetry points having hole pocket at Γ and electron pocket at L/M point, and (c) band topology near Γ and M point. Figure taken from Ref. [146, 147].

3.3.2 CDW in 1T–TiSe₂

1T–TiSe₂ undergoes a second-order phase transition into the CDW phase below the 200 K. X-ray diffraction scattering measurements indicate that the CDW is commensurate [27], but under pressure or intercalation of Cu atoms, it becomes incommensurate [148, 149]. The charge density is defined by the three wave vectors that connect the Γ and L points in the hexagonal Brillouin zone (BZ). The charge density modulation is given by,

$$\rho(\mathbf{r}) = \rho_0(\mathbf{r}) \left[1 + \sum_{i=1}^3 \rho_i \cos(\mathbf{q}_i \mathbf{r} + \phi) \right] \quad (3.3-19)$$

with ordering vectors $\mathbf{q}_1 = \frac{1}{2}(\mathbf{a}^* + \mathbf{c}^*)$, $\mathbf{q}_2 = \frac{1}{2}(\mathbf{b}^* + \mathbf{c}^*)$, and $\mathbf{q}_3 = \frac{1}{2}(\mathbf{b}^* - \mathbf{c}^*)$, where \mathbf{a}^* , \mathbf{b}^* and \mathbf{c}^* are the reciprocal lattice vectors [146]. These three charge density wave vectors are shown in Figure 3.5b. The first signature of the CDW phase transition is an anomalous increase in resistivity near the transition temperature of 200 K, which is consistent with the Fermi nesting description of a metal-to-insulating (MIT) transition [150]. However,

ARPES and DFT calculations rule out this case due to a lack of parallel Fermi surface sheets for nesting.

3.4 Mechanism Behind the Phase Transition

In a 1D metallic system, the CDW is defined by the Peierls transition, which is explained by the mechanism of Fermi surface nesting that is also applied to higher dimensional systems. In 1976, Di Salvo proposed that electron-phonon interaction with Fermi nesting [150] was the most likely origin of the CDW in 1T-TiSe₂. However, it was later observed that Fermi nesting is not favorable in 1T-TiSe₂ due to the fact that both Γ and L/M points have too much a 3D spherical shape [151]. In a higher dimensional system, the behavior of the Lindhard function is different than the 1D system, as shown in Figure 3.1(b) and does not favor a CDW instability. Consequently, an alternative explanation for the CDW is required. In 1977, Wilson et al. suggested that the CDW is purely electronic due to the excitonic insulator mechanism [36]. However, the same year, Hughes proposed a new mechanism behind the CDW, which is a band-type Jahn-Teller effect, based on the effects of the detailed atomic movements involved in the *d*-band electronic energy bands [152]. Thus, the debate on the driving mechanism behind the CDW in 1T-TiSe₂ is ongoing.

Jerome and coworkers proposed theoretically that the condition for an excitonic phase transition in a semimetal or semiconductor is a small or negative band gap [126]. If the Coulomb interaction is weakly screened, it may be sufficient to bind together electrons from the conduction band (CB) and holes from the valence band (VB) to form excitons. The formation of the exciton is depicted in Figure 3.6. If the binding energy of the exciton is greater than the gap, the material undergoes a CDW transition. 1T-TiSe₂ meets all the criteria defined by Jerome et al., for the formation of exciton. It exists either as a semiconductor or semimetal with an indirect band gap between the Γ and L points in the band structure with a small band gap $\Delta \sim 20$ meV and a very small number carrier density

$\sim 10^{20} \text{ cm}^{-3}$ [153]. The Coulomb interaction between the holes at Γ and electrons at L is weakly screened, leading to the formation of excitons. This formation lowers the overall energy of the system, which undergoes a structural distortion that doubles the lattice period. The observation of a soft electronic mode near q_{CDW} in momentum-resolved electron energy-loss spectroscopy (M-EELS) data provides evidence of excitonic condensation coexisting with the periodic lattice distortion (PLD) [154]. This is among the large collection of theoretical and experimental evidence in favor of the excitonic insulator scenario as the pure driving force for the CDW transition in 1T-TiSe₂ [144, 155].

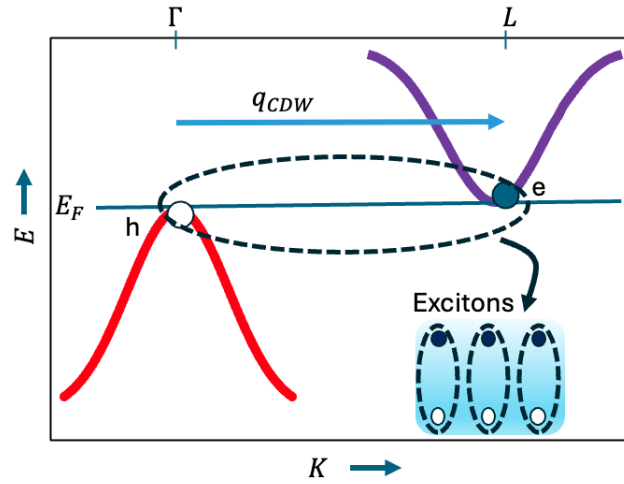


Figure 3.6: Excitonic insulator mechanism. Weakly screened electrons (e) and holes (h) in the conduction and valence bands of a semiconductor with a small band gap or a semimetal with band overlap couple via the Coulomb interaction to form a condensate of excitons at low temperature.

Another mechanism behind the geometrical distortion on 1T-TiSe₂ lattice is the Jahn-Teller mechanism described above. In the crystal field, the Ti d orbital manifold is split into three t_{2g} orbitals and two e_g orbitals. This d orbital-based band dominates the electron pocket at M. At Γ , the two low energy t_{2g} orbitals hybridize with the Se- p orbitals to determine the electron distribution and orbital arrangement in 1T-TiSe₂. At low temperatures, the atoms are displaced from their original position, which is known from neutron diffraction experiments [156], and the charge is transferred between the t_{2g} and Se- p orbitals through along the ordering vector [157]. Within the framework of the Jahn-Teller mech-

anism in 1T–TiSe₂, two different approaches arise to define the distortion pattern. The first approach is given by Hughes, who noted that for transition-metal dichalcogenides, the lowest-lying *d*-band is slightly lower in the 2H-type structure compared with the 1T structure [152]. The atomic displacements observed during the phase transition of 1T–TiSe₂ show a change from octahedral (1T) to trigonal prismatic (2H) local coordination. Such a transformation would lead to a downward shift of the Ti 3*d* band, thereby reducing the total energy. Contrary to Hughes, Whangbo and Canadell argued that within the Jahn-Teller mechanism framework, the energy reduction leading to structural modulation in 1T–TiSe₂ should be attributed not to changes in the Ti 3*d* bands but to the Se 4*p* bands [158]. They suggested that this *p*-band energy reduction is linked with Ti-Se bond shortening in the displacement pattern observed during the phase transition.

One mechanism is purely electronic, focusing on exciton condensation, and the other is driven by electron-phonon interactions, following a Jahn-Teller type mechanism. However, while exciton condensation and Jahn-Teller-type mechanisms are separate mechanisms for the CDW, their combined contribution is also possible. Much theoretical and experimental evidence supports the existence of both hypotheses [159–161]. Some are focusing on clarifying how much of the CDW phenomenon in this material is due to the collective behavior of excitons, purely electronic effect, and how much is due to the Jahn-Teller type effect driven by electron-phonon interaction. In 2006, Morosan et al. observed that the critical temperature of CDW can be suppressed by doping with Cu [30]. A follow-up experiment by Kogar and coworkers suggests that an incommensurate CDW emerges with doping [29], as shown in Figure 3.7. They suggest that Cu doping affects the Ti-3*d* conduction band, which suppresses excitonic correlations while leaving the electron-phonon interaction less affected. Therefore, at low doping levels, both excitonic and electron-phonon coupling contribute, while at high doping levels, only electron-phonon coupling is important.

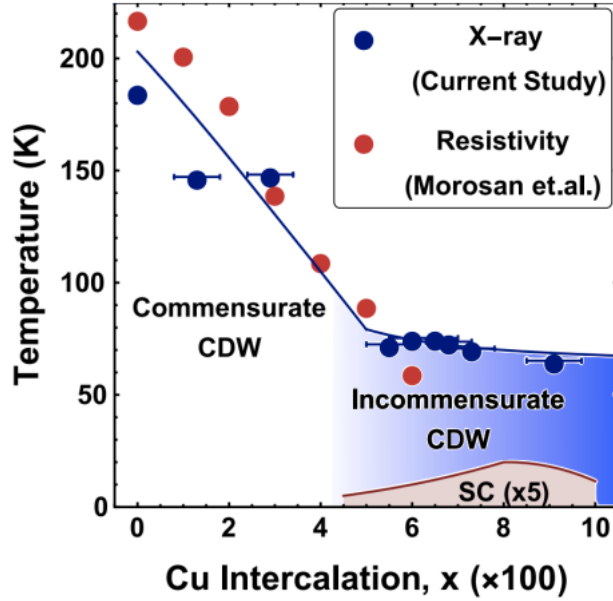


Figure 3.7: CDW transition temperature as a function of Cu intercalation in TiSe_2 . The phase diagram shows the commensurate and incommensurate phases along with the superconductive phase. Figure taken from [29].

3.5 Recent Study on the Nature of CDW Phase Transition

Chirality in solids refers to a geometric property of certain materials where the structure breaks mirror reflection, space inversion, and roto inversion symmetries. Chirality in CDWs refers to a pattern of electron density modulation that lacks mirror symmetry. Such a chiral CDW has been reported in TMDCs, topological semimetals, and Kagome lattices such as Ti-doped TaS_2 [162], 1T-TiSe_2 [34, 163, 164], $(\text{TaSe}_4)_2\text{I}$ [165] and KV_3Sb_5 [166], respectively. Fourier transform analyses of Scanning Tunneling Microscopy (STM) images from Ti-doped 1T-TaS_2 revealed the existence of a chiral CDW from doping-enhanced orbital order.

In 1T-TiSe_2 , a chiral CDW was allegedly observed in STM measurements, which is due to a phase shift of the electronic function by $2\pi/3$ between the layers along the crystalline axis c [34]. The STM image and amplitude of the line profile along the CDW vectors are shown in Figure 3.8. It has been noted that the three intensity peaks of CDW decrease clockwise and anticlockwise, which rotates the relative phase shift between CDW

vectors. In real space, that shift makes a helical structure in CDW unit cells with the periodicity of $2c_0$, which is shown in Figure 3.9.

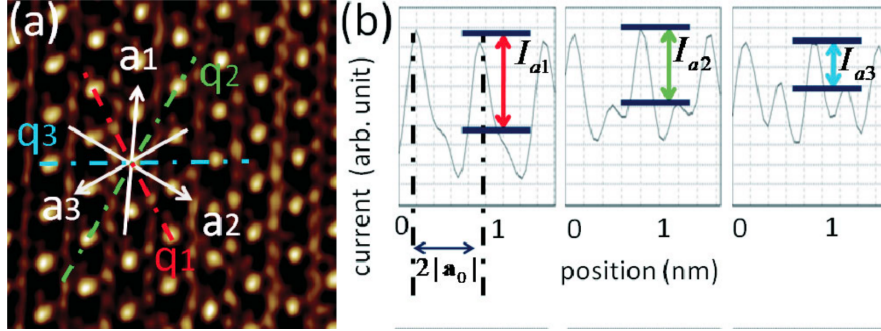


Figure 3.8: (a) STM image of 1T–TiSe₂ with unit vectors a_1 , a_2 and a_3 (b) amplitude of line profile along unit vectors of panel (a). Figure taken from [34].

Chiral CDWs with gyrotropic order may be observed and manipulated via circularly polarized light [163]. However, Hildebrand et al. found that CDW modulations on neighboring layers were identical in 1T–TiSe₂, thus contradicting the helical stacking model [37]. Hildebrand et al. combine the STM with a low density of buried defects to measure the PLD distortion beyond the single STM measurement. CDWs across adjacent layers maintain a uniform CDW modulation with defects induced by interstitial Ti atoms, as shown in Figure 3.10. This disproves the earlier claim concerning chirality due to helical stacking layers.

Further, an X-ray diffraction study indicates an emergent chiral atomic configuration occurring below the CDW transition temperature [164]. A mechanism for the formation of this scalar chirality in 1T–TiSe₂ was recently proposed, in which the chiral phase is interpreted to be simultaneously charged and orbitally ordered with experimental evidence for a sequence of two transitions, i.e., the well-known CDW transition at 192 K and a novel transition at 183 K, which is shown in Figure 3.11 as a change in slope in specific heat.

In the debate over chirality in 1T–TiSe₂, a new proposal has been examined that attributes chirality to a structural distortion induced by an elevation in the electronic temperature [31]. 1T–TiSe₂ has a soft mode at the M and L point. The high temperature structure

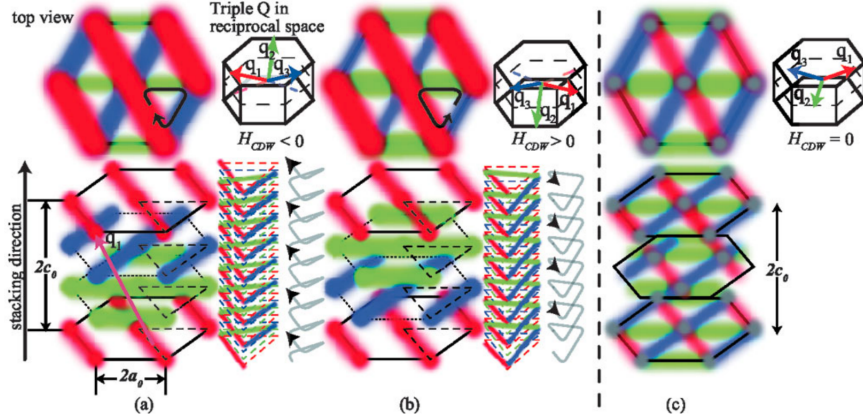


Figure 3.9: Schematic representation of (a) left-handed chiral CDWs (b) right-handed chiral CDWs in a TiSe_2 CDW unit cell in real space and (c) typical 2D CDW. The strong coloration indicates high concentration. Figure taken from [34].

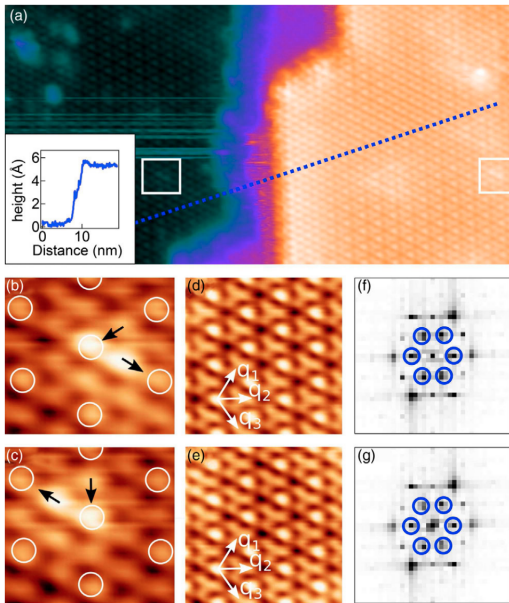


Figure 3.10: (a) STM image of 1T-TiSe₂ two adjacent 1T-TiSe₂ layers with height difference of approximately 6 Å (b), (c) Enlargements on the defects of the bottom and top layer, respectively, with white circles indicating the position of the maxima of the CDW charge modulation and black arrows indicating the corresponding PLD-induced atomic displacements (d), (e) CDW modulation in the bottom and top layer, respectively, with arrows indicating the orientations of the CDW q vectors (f), (g) are FFT-amplitude plots of (d) and (e) with blue circles highlighting the extra spots originating from the CDW charge modulation. Figure taken from [37].

of 1T-TiSe₂, which belongs to space group $P\bar{3}m1$ can undergo a structural change into another achiral space group $P\bar{3}c1$ with a $2 \times 2 \times 2$ structure that has a soft mode at the M

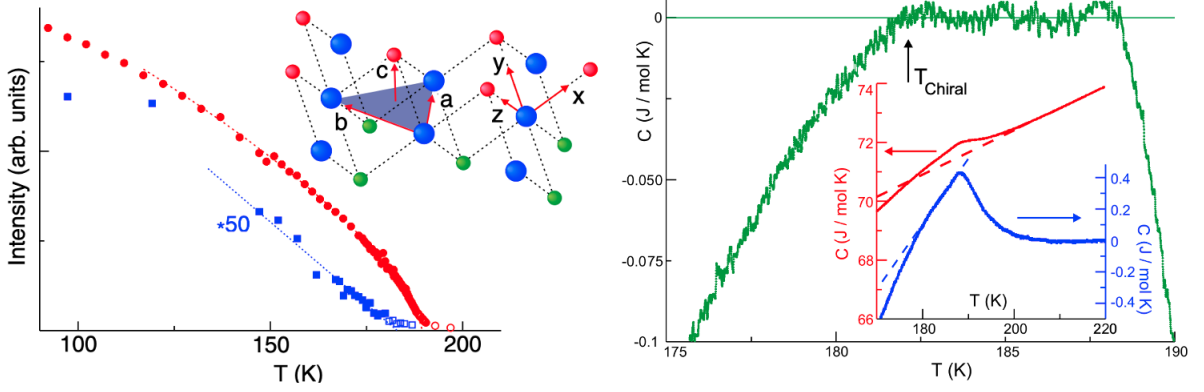


Figure 3.11: Integrated intensities of the superlattice reflections in 1T–TiSe₂ at $[\frac{3}{2}, \frac{3}{2}, \frac{1}{2}]$ (red) and $[\frac{5}{2}, 1, 0]$ (blue) amplified by a factor of 50). (inset) Schematic depiction of a single layer of 1T–TiSe₂.The plane of Ti atoms (large and blue) is indicated along with the crystallographic axes a, b, and c. The orbital basis instead uses x, y, and z axes, which connect the Ti and Se atoms (smaller, red, and green). Figure taken from [164].

point, or into a chiral space group $P321$ with $2 \times 2 \times 1$ structure that has a soft mode at the L point. In the $2 \times 2 \times 2$ reconstruction, the Ti atom moves along the crystalline c-axis in the opposite direction, so the CDW phase is structurally achiral, while in the $2 \times 2 \times 1$ reconstruction, there is a single layer along the crystalline c-axis, so chirality is observed in bulk structure, as shown in Figure 3.12. Evidence for the nonthermal melting and chiral symmetry breaking under optical excitation for a finite range of laser fluences has been observed, which is consistent with the measurements of Möhr-Vorobeva et al. [167]. Under a critical laser fluence, when the electronic temperature is increased above a lower critical temperature T_1 and above a higher critical temperature T_c , the $P321$ structure will be established as the ground state. Below T_1 the ground state structure is $P\bar{3}c1$. The maximum energy difference between the two ground states is about 0.5 meV/TiSe₂ [31]. Above T_2 , the ion-electron interaction will be sufficiently weak, and a high-temperature phase of $P\bar{3}m1$ exists. The evidence for the existence of a chiral phase has been observed through time-resolved circular dichroism measurements, which are presented in Chapter 6.

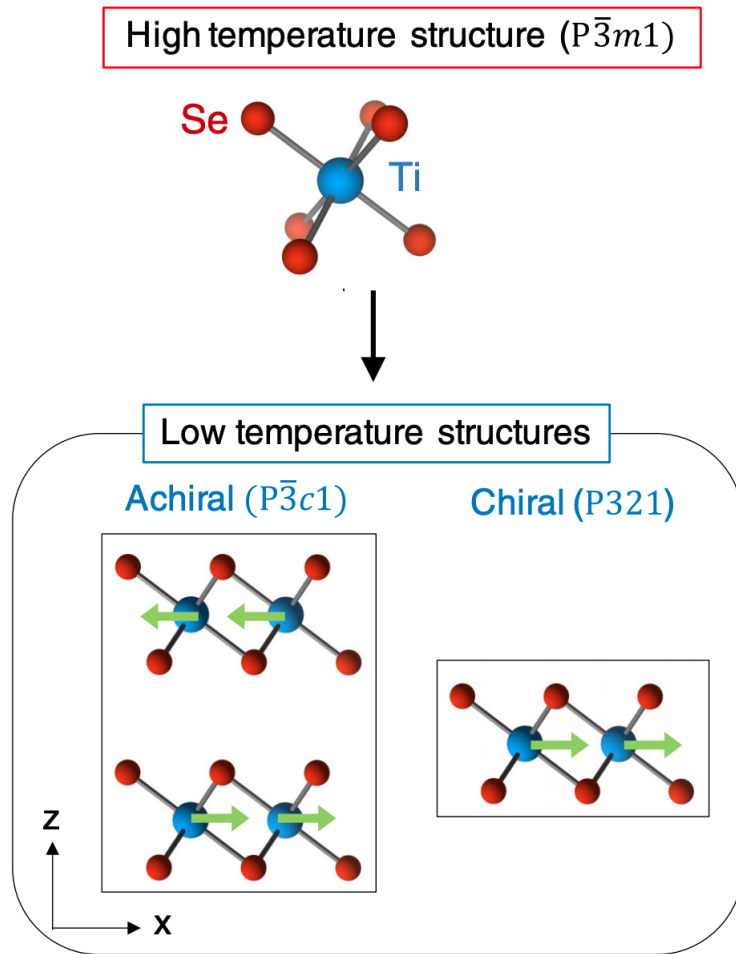


Figure 3.12: A diagram for how the achiral centrosymmetric high temperature $P\bar{3}m1$ structure transform into either the achiral centrosymmetric $P\bar{3}c1$ CDW structure or the chiral noncentrosymmetric $P321$ CDW at low temperature. The green arrows indicate the direction in which the Ti atoms are displaced in the CDW phase. Figure taken from [31].

CHAPTER 4

EXPERIMENTAL METHODS

This chapter provides a brief overview of the experimental methods used in this thesis. Our experimental methodology uses nonlinear spectroscopy techniques, such as harmonic generation and the photogalvanic effect, as well as time-resolved pump-probe spectroscopy. Fundamentally, a nonlinear optical process occurs when a system's response to incident light is not linearly proportional to the applied field. Nonlinear optical features can exist in both centrosymmetric and non-centrosymmetric materials. However, the order of nonlinear responses generated are intimately dependent on the material's symmetry. For example, centrosymmetric materials do not support even-order nonlinear optical processes such as photogalvanic effects and second harmonic generation, but they can be present in noncentrosymmetric materials. Here, we will discuss the principles of time-resolved pump-probe spectroscopy, as well as concepts related to second and third-order nonlinear optics and THz emission spectroscopy.

4.1 Time Resolved Pump-Probe Spectroscopy

Pump-probe spectroscopy is an experimental technique used to study the electronic relaxation dynamics in materials or molecules over varying time scales, (e.g., 10^{-3} - 10^{-15} sec) after the optical perturbation. This method is used to study the electronic properties such as electronic states, vibrational, or optical properties followed by excitation.

The absorption of a short, intense laser pulse disrupts the electronic equilibrium of a sample via excitation of carriers from the ground state to higher energy states. The population of excited states has an impact on optical properties, such as reflectance and

absorbance. In the subsequent picosecond, the hot carriers go thermalized via electron-electron [168] and electron-phonon scattering [169], which will redistribute the excited carrier energies [170]. The carriers relax back to the ground state through radiative recombination, such as emitting photons, or non-radiative recombination, such as transferring energy to the lattice or to other carriers [171]. The process of relaxation depends on the material system and the nature of the excitation state [172].

During photoexcitation and relaxation, transitions to higher energy states can change dielectric function and reflectivity. In the most extreme cases, the redistribution of the electronic propagation is great enough to photoinduced phase or structural change in a material, which drastically changes both absorption and reflectivity [168]. For example, the topological insulator is driven into a Dirac semimetal, which significantly alters its optical properties [173].

The photoinduced changes in a material's optical properties induced by the pump are typically read through the low-power probe beam, which interacts with the material after it has been excited by the pump and is typically monitored as a function of time by mechanically delaying its arrival at the sample with reflecting optics on a linear stage. If the pump beam has altered the material's absorption or reflection characteristics, the probe beam's intensity will be modified after interacting with the excited medium. By measuring absorption/reflection at various delay times between the pump and probe pulse, one can track how the material's electronic or structural properties evolve with time. The delay between the pump and probe pulses also allows for the study of the temporal resolution of the changes induced by the pump. Systematically varying the delay allows the construction of a time-resolution picture of the response of the material to the excitation, carrier recombination, thermalization, etc.

A schematic diagram of the pump-probe apparatus used in this thesis is shown in Figure 4.1a. To read the change by the pump beam, the pump and probe beam must precisely overlap at the sample. In order to achieve the sensitivity needed for this kind of measure-

ment, the pump beam is chopped with an optical modulator such as, e.g., a chopper wheel or electro-optic modulator at frequency f_m . The change in reflectivity due to the excitation

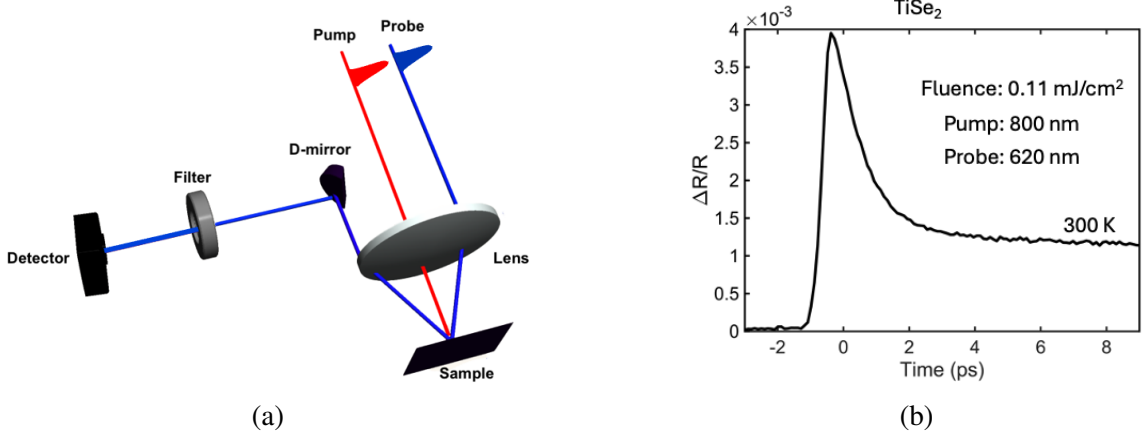


Figure 4.1: (a) experimental setup for time-resolved pump-probe measurement where pump (red) and probe (blue) beam incidence on the sample and modulation in probe beam is measured through the detector (b) change in reflectivity on 1 T–TiSe₂ measured using time-resolved pump-probe experimental setup with 800 nm pump beam having fluence 0.11 mJ/cm² and 620 nm probe beam at room temperature.

of the pump beam is then measured as;

$$\frac{\Delta R(t)}{R} = \frac{R_{\text{pump on}} - R_{\text{pump off}}}{R_{\text{pump off}}} \quad (4.1-1)$$

where $R_{\text{pump off}}$ is the intensity of the probe beam when the optical modulator blocks the pump beam, and $R_{\text{pump on}}$ is the intensity of the probe beam when the optical modulator allowed to reach the sample. The signal is then recovered either through lock-in detection [174] or through the use of data acquisition card [175] as detailed below. Example time-resolved pump-probe experimental data on 1 T–TiSe₂ is shown in the Figure 4.1b, where change in reflectivity on 1 T–TiSe₂ measured with 800 nm pump beam having fluence 0.11 mJ/cm² and 620 nm probe beam at room temperature. The relaxation time for the excited quasiparticles is about one picosecond.

4.1.1 Experimental Alignment and Challenges

Proper experimental alignment of the pump and probe beam is crucial for accurate time-resolved pump-probe measurement. The most common experimental challenge in aligning the pump-probe setup is ensuring spatial and temporal overlap of the pump and probe beams on the sample, eliminating pump scatter, and removing coherent artifacts through appropriate choice of pump and probe polarizations.

Temporal overlap can be achieved by adjusting the optical path of the pump/probe beam using a delay stage and monitoring for a cross-correlation signal to appear from interaction in a BBO crystal. Spatial overlap obtained by adjusting the mirror of the pump/probe path such that both beams pass through a common pinhole aperture at their common focus and visualizing through an IR card or CCD camera.

Pump scattering reduces the signal-to-noise ratio (SNR) in the measurement, and it is discovered that it can arise if the detector is able to measure both pump and probe wavelengths. We can mitigate this effect by proper spectral filtering, spatial filtering, and polarization control of the pump beam both before and after the sample. Using the proper optical filters, which block the pump beam and only pass the probe, greatly reduces the detector detection of the pump beam. However, if the pump and probe wavelength are close, getting the proper filters is very challenging. In this case, blocking the pump beam using spatial filtering, such as irises, pinholes, and other physical barriers, before it reaches the detector will minimize this effect. If the pump and probe beam are collinear and overlap or intersect at a small angle before the sample, spatial filtering may not be practicable. In this case, polarization control with mutually orthogonal polarized pump and probe beams is the most realistic method. In this thesis, I have used a wire grid polarizer, which has a high extinction ratio $> 1000 : 1$ over the wavelength $0.6 \mu\text{m}$ to $4 \mu\text{m}$ with a transmission axis parallel to the polarization of the probe beam.

The coherent artifact is due to interference between the pump and probe beam within the sample or in optical components that can cause artifacts that appear like diffraction

grating patterns at the time zero ($t = 0$). This artifact can mask the signal and complicate the interpretation of the data. The effect can be minimized using polarization grating, sensitive detection, or changing the ratio between the probe and pump power [176].

4.1.2 Pump-Probe Data Detection Method

While lock-in detection is usually favored in pump-probe measurements, the detection method used for the experiment here is a balanced detection scheme and a data acquisition (DAQ) card, which is depicted in Figure 4.2. Balanced detection in which $\Delta R(t)$ is

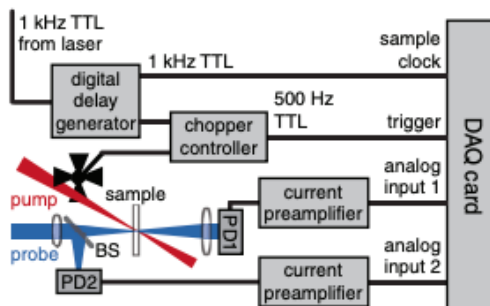


Figure 4.2: The experimental setup for pump-probe traces with the DAQ card. The pump is modulated at half the laser repetition rate with a chopper that is synchronized with the laser. A beamsplitter (BS) splits the probe beam into two parts to implement balanced detection. The current outputs of both photodiodes are converted to voltage and amplified by the current preamplifiers prior to digitization by the DAQ card. The DAQ card sampling clock is synched to the laser so that every laser pulse energy is measured at each photodiode. The trigger signal from the chopper controller assures that the pump is always blocked when the first pulse energy is acquired. Figure taken from Ref. [175].

calculated for the difference between two copies of the probe amplitude, one of which has interacted with the photoexcited sample while the other has not. This method improved the signal-to-noise ratio and reduced the effect of laser intensity fluctuations. The pump beam is modulated with a frequency f distinct from the laser repetition frequency, causing a material change at the signal frequency f as measured either by a lock-in amplifier or the DAC-based technique.

The signal delay generator (SDG) of the laser provides a synchronized transistor-transistor logic (TTL) signal at the repetition rate to the DAC and the optical chopper. Here, the pump

beam is modulated by a chopper wheel at half of the laser repetition rate so that every other pump pulse is blocked. Because SDG functions as the clock of the experiment, we measure every probe pulse arriving at each photodiode. The $f/2$ output of the chopper was then input into the DAC so that every, e.g., the even-numbered pulse had the pump present, and odd-numbered pulses had the pump blocked such that the average of all present- all every blocked could provide the value of $\Delta R(t)$.

The normalized value of change in reflectivity ΔR from the sample is obtained as follows [175];

$$\frac{\Delta R}{R_0} = \frac{PD1_a / PD2_a}{PD1_b / PD2_b} - 1 \quad (4.1-2)$$

where $PD1_a(PD1_b)$ and $PD2_a(PD2_b)$ are signals from each photodiode for a pulse when the pump is present (block).

4.2 Nonlinear Harmonic Generation

Nonlinear harmonic generation is a phenomenon observed in nonlinear optics where n photons with the same frequency ω_i interact with a nonlinear medium to generate a new photon with frequency n times greater than the initial photon, *i.e.*, $\omega_f = n\omega$ as shown in Figure 4.3.

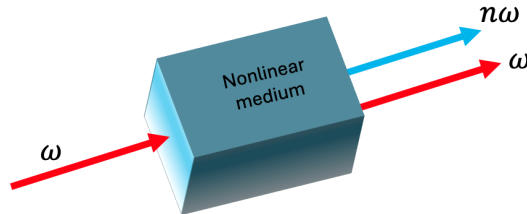


Figure 4.3: Schematic view of the N^{th} harmonic conversion of an incidence beam of frequency ω interacting with nonlinear medium and generating a higher harmonic beam of frequency $n\omega$ along with incidence beam.

Even order harmonics ($\omega_f = n_e \omega$, $n_e = 2, 4, 6, \dots$) only can be generated from noncentrosymmetric crystal structures. The surface or interface of materials can always generate even-order nonlinear harmonic generation, even when forbidden in the bulk, since an interface is a locus of inversion symmetry breaking. This makes the study of even-order nonlinear harmonic generation extremely useful for the characterization of interfaces and surfaces, as well.

When a medium is subjected to a weak electric (magnetic) field, the electrons in the medium undergo a displacement. In the case of weak electric (magnetic) fields, the polarization (magnetization) observed in an isotropic paramagnetic or diamagnetic medium is directly proportional to the magnitude of the applied field as

$$P_i = \chi_{ij}^{ee} E_j \quad (4.2-3)$$

$$M_i = \chi_{ij}^{mm} H_j \quad (4.2-4)$$

where χ_{ij}^{ee} and χ_{ij}^{mm} are linear electric and magnetic susceptibility tensors respectively. These tensors must mathematically transform with the symmetry properties of the crystal as dictated by Neumann's Principle [177].

Linear polarization (magnetization) is an approximation of the full effect of the electric (magnetic) field on the medium. The full effect is given by a Taylor expansion of polarization (magnetization) in terms of electric (magnetic) field as:

$$P_i = \chi_{ij}^{ee} E_j + \chi_{ijk}^{eee} E_i E_j + \chi_{ijkl}^{eeee} E_j E_k E_l + \dots \quad (4.2-5)$$

$$M_i = \chi_{ij}^{mm} H_j + \chi_{ijk}^{mmm} H_i H_j + \chi_{ijkl}^{mmmm} H_j H_k H_l + \dots \quad (4.2-6)$$

where χ_{ijk}^{eee} and χ_{ijkl}^{eeee} are the second and third-order nonlinear susceptibilities, respectively, and are responsible for many interesting optical phenomena such as second-harmonic

generation [178], third-harmonic generation [179], optical rectification [180], and sum frequency generation [181]. In this thesis, we are primarily interested in the second-harmonic generation and the third-harmonic generation.

4.2.1 Second Harmonic Generation

Second Harmonic Generation (SHG) is a nonlinear optical process in which two photons with the same frequency interact with a nonlinear material and combine to form a new photon with twice the energy, and therefore twice the frequency, of the original photons. The second term of the Equation 4.2-5 defines the SHG nonlinear process where E_i and E_j are identical. If ω is the frequency of the incidence beam, SHG polarization is defined as:

$$P_i(2\omega) = \chi_{ijk}^{eee} E_i(\omega) E_j(\omega) \quad (4.2-7)$$

Under the inversion in centrosymmetric materials, Equation 4.2-7 can be written as;

$$\begin{aligned} -P_i(2\omega) &= \chi_{ijk}^{eee} E_i(-\omega) E_j(-\omega) \\ &= P_i(2\omega) \end{aligned} \quad (4.2-8)$$

This condition is only true if $\chi_{ijk}^{eee} = 0$, *i.e.*, it is not allowed in centrosymmetric materials and is present only if materials lack inversion symmetry. So, this experimental method is beneficial for studying structural change in material from centrosymmetric to noncentrosymmetric or vice versa.

The magnetic field of radiation also can generate SHG. When electromagnetic waves travel through a nonlinear medium, the generalized SHG polarization $P_i(2\omega)$ which accounts for both electric and magnetic field components of the incident light, is given by

$$P_i(2\omega) = \chi_{ijk}^{eee} E_j(\omega) E_k(\omega) + \chi_{ijk}^{em} E_j(\omega) H_k(\omega) + \chi_{ijk}^{emm} H_j(\omega) H_k(\omega) \quad (4.2-9)$$

The second term of the Equation 4.2-9 accounts for a mixed electric-magnetic dipole interaction, i.e., it is a nonlinear magneto-electric effect in which the combined action of electric and magnetic fields induces polarization. The materials that show this effect exhibit phenomena such as the optical magnetoelectric effect [182]. The third term of the equation accounts for the induced polarization due to pure magnetic dipole transitions. This effect is less common in optical transition because magnetic susceptibilities are generally much weaker at optical frequencies.

Similarly, the generalized SHG magnetization $M_i(2\omega)$ with accounts for both electric and magnetic field components of incident light is given by

$$M_i(2\omega) = \chi_{ijk}^{mee} E_j(\omega) E_k(\omega) + \chi_{ijk}^{mem} E_j(\omega) H_k(\omega) + \chi_{ijk}^{mmm} H_j(\omega) H_k(\omega) \quad (4.2-10)$$

The first term on the right-hand side represents SHG magnetization due to a pure electric dipole-driven transition. The second term represents magnetization due to a mixed electric/magnetic dipole interaction, and the third term represents magnetization due to a pure magnetic dipole-driven transition.

In a bi-isotropic chiral medium, an electromagnetic wave's electric and magnetic fields interact in an unusual way, even at the first order. The electric field and polarization field (magnetization and inductive magnetic field) are not parallel. In these chiral media, electric and magnetic fields are coupled. The most general linear relation that describes this effect can be written by adding the electromagnetic coupling term [19],

$$P_i = \chi_{ij}^{ee} E_j + \chi_{ij}^{em} H_j \quad (4.2-11)$$

$$M_i = \chi_{ij}^{mm} H_j + \chi_{ij}^{me} E_j \quad (4.2-12)$$

These equations describe media with a trivial crystallographic magnetoelectric cross-coupling where χ_{ij}^{me} and χ_{ij}^{em} denote the tensorial coupling coefficient between the electric and magnetic field.

In SHG, the magnetic dipole interaction can result in the absorption of a photon at the fundamental frequency or in the emission of a photon at the second harmonic generation. Electric dipole polarization and magnetization polarization of atoms inside a nonlinear chiral medium induced by electric and magnetic field of incidence light at second order interaction is thus given by:

$$P_i = \chi_{ijk}^{eee} E_j E_k + \chi_{ijk}^{eem} E_j H_k + \chi_{ijk}^{emm} H_j H_k \quad (4.2-13)$$

$$M_i = \chi_{ijk}^{mee} E_j E_k + \chi_{ijk}^{mem} E_j H_k + \chi_{ijk}^{mmm} H_j H_k \quad (4.2-14)$$

The strength of magnetic dipole transitions is typically smaller than the electric dipole transition by a factor of the fine structure constant $\alpha^2 \approx (1/137)^2$. χ_{ijk}^{emm} , χ_{ijk}^{mem} , and χ_{ijk}^{mmm} are much smaller than other terms in Equations 4.2-13 and 4.2-14. In this approximation, the nonlinear polarization and magnetization for the chiral medium can be rewritten as,

$$P_i = \chi_{ijk}^{eee} E_j E_k + \chi_{ijk}^{eem} E_j H_k \quad (4.2-15)$$

$$M_i = \chi_{ijk}^{mee} E_j E_k \quad (4.2-16)$$

which is consistent with the result of Maki et al. [183]. This equation describes the second-order correlation between electric polarization and magnetization, showing how a material's polarization is impacted by a magnetic field and its magnetization is influenced by an electric field. In a subsequent chapter, we will discuss how a resonant magnetic dipole transition induces the nonlinear constitutive relation of Equations 4.2-15 and 4.2-16. This effect is responsible for the emission of helical SHG from normally incident linearly polarized

fundamental. We used a rotating retarder polarimetry technique to study the polarization state of this SHG beam, as described below.

4.2.1.1 Polarimetry

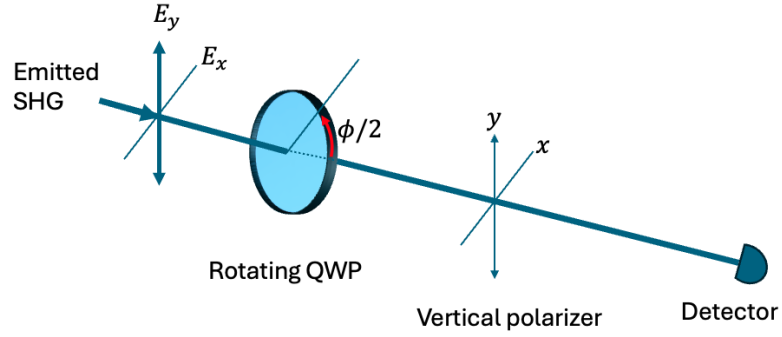


Figure 4.4: A schematic experimental diagram for rotating quarter waveplate (QWP) polarimetry measurement. The emitted SHG passes through a rotating QWP with phase retardation ϕ , then through a vertical polarizer, before being collected by the detector.

A schematic of the polarimetry setup used to measure the polarization state of SHG emitted from the sample is shown in Figure 4.4. The beam emitted from the sample passes through a rotating quarter-wave plate and a fixed vertical polarizer and is later collected by the detector. The polarization state is recovered from the amplitude as a function of the polarizer angle as derived below:

The Stokes vector of the beam is [184]

$$S = \begin{pmatrix} S_0 \\ S_1 \\ S_2 \\ S_3 \end{pmatrix} \quad (4.2-17)$$

The Muller matrix for the quarter wave plate is [184]

$$M_{QWP} = \begin{pmatrix} 1 & 0 & 0 & 0 \\ 0 & 1 & 0 & 0 \\ 0 & 0 & \cos(\phi) & \sin(\phi) \\ 1 & 0 & -\sin(\phi) & \cos(\phi) \end{pmatrix} \quad (4.2-18)$$

where ϕ is the phase retardation of the quarter-wave plate.

Mueller matrix for rotation by angle θ is given by

$$M_R = \begin{pmatrix} 1 & 0 & 0 & 0 \\ 0 & \cos(2\theta) & \sin(2\theta) & 0 \\ 0 & -\sin(2\theta) & \cos(2\theta) & 0 \\ 1 & 0 & 0 & 1 \end{pmatrix} \quad (4.2-19)$$

The Muller matrix for the rotating quarter-wave plate is thus [184]

$$M'' = M_R(-2\theta)M_{QWP}M_R(2\theta) \quad (4.2-20)$$

$$M'' = \begin{pmatrix} 1 & 0 & 0 & 0 \\ 0 & \cos^2(2\theta) + \cos(\phi) \sin^2(2\theta) & \sin(4\theta) \sin^2(\frac{\phi}{2}) & -\sin 2\theta \sin \phi \\ 0 & \sin(4\theta) \sin^2(\frac{\phi}{2}) & \cos^2(2\theta) \cos \phi + \sin^2(2\theta) & \cos(2\theta) \sin(\phi) \\ 0 & \sin 2\theta \sin \phi & -\cos 2\theta \sin \phi & \cos \phi \end{pmatrix}$$

This makes the Stokes vector of the emerging beam from the rotating quarter wave plate

$$S'' = M''S$$

$$\begin{aligned}
\mathbf{S}'' &= \begin{pmatrix} 1 & 0 & 0 & 0 \\ 0 & \cos^2(2\theta) + \cos(\phi) \sin^2(2\theta) & \sin(4\theta) \sin^2(\frac{\phi}{2}) & -\sin 2\theta \sin \phi \\ 0 & \sin(4\theta) \sin^2(\frac{\phi}{2}) & \cos^2(2\theta) \cos \phi + \sin^2(2\theta) & \cos(2\theta) \sin(\phi) \\ 0 & \sin 2\theta \sin \phi & -\cos 2\theta \sin \phi & \cos \phi \end{pmatrix} \times \begin{pmatrix} S_0 \\ S_1 \\ S_2 \\ S_3 \end{pmatrix} \\
\mathbf{S}'' &= \begin{pmatrix} S_0 \\ S_1(\cos^2(2\theta) + \cos(\phi) \sin^2(2\theta)) + S_2(\sin(4\theta) \sin^2(\frac{\phi}{2})) - S_3(\sin 2\theta \sin \phi) \\ S_1(\sin(4\theta) \sin^2(\frac{\phi}{2})) + S_2(\cos^2(2\theta) \cos \phi + \sin^2(2\theta)) + S_3(\cos(2\theta) \sin(\phi)) \\ S_1(\sin 2\theta \sin \phi) - S_2(\cos 2\theta \sin \phi) + S_3 \cos \phi \end{pmatrix}
\end{aligned}$$

The vertical polarizer, Muller matrix is given by

$$M_P = 1/2 \begin{pmatrix} 1 & -1 & 0 & 0 \\ -1 & 1 & 0 & 0 \\ 0 & 0 & 0 & 0 \\ 0 & 0 & 0 & 0 \end{pmatrix} \quad (4.2-21)$$

Thus Stokes vector of the beam that emerges from the combination of a rotating quarter-wave retarder and a vertical polarizer is:

$$\begin{aligned}
S_F &= 1/2 \begin{pmatrix} 1 & -1 & 0 & 0 \\ -1 & 1 & 0 & 0 \\ 0 & 0 & 0 & 0 \\ 0 & 0 & 0 & 0 \end{pmatrix} \times \\
&\begin{pmatrix} S_0 \\ S_1(\cos^2(2\theta) + \cos(\phi) \sin^2(2\theta)) + S_2(\sin(4\theta) \sin^2(\frac{\phi}{2})) - S_3(\sin 2\theta \sin \phi) \\ S_1(\sin(4\theta) \sin^2(\frac{\phi}{2})) + S_2(\cos^2(2\theta) \cos \phi + \sin^2(2\theta)) + S_3(\cos(2\theta) \sin(\phi)) \\ S_1(\sin 2\theta \sin \phi) - S_2(\cos 2\theta \sin \phi) + S_3 \cos \phi \end{pmatrix}
\end{aligned}$$

$$\mathbf{S}_F = \frac{1}{2}[S_0 - S_1(\cos^2(2\theta) + \cos(\phi)\sin^2(2\theta)) - S_2(\sin(4\theta)\sin^2(\frac{\phi}{2})) + S_3(\sin 2\theta \sin \phi)] \times \begin{pmatrix} 1 \\ -1 \\ 0 \\ 0 \end{pmatrix}$$

$$\mathbf{S}_F = I(\theta, \phi) \times \begin{pmatrix} 1 \\ -1 \\ 0 \\ 0 \end{pmatrix}$$

where $I(\theta, \phi)$ represents the intensity of the beam that has been detected by the detector. Fitting the experimental data with this mathematical expression gives the value of Stokes parameters of the incoming beam. The polarization state of light can be obtained as below
The Degree of polarization is given by

$$DOP = \frac{\sqrt{S_1^2 + S_2^2 + S_3^2}}{S_0} \quad (4.2-22)$$

It varies from 0 (unpolarized) to 1 (fully polarized).

The orientation angle of an incident beam is given by ψ , where

$$\tan(2\psi) = \frac{S_2}{S_1} \quad (4.2-23)$$

The ellipticity angle of the beam is χ

$$\sin(2\chi) = \frac{S_3}{S_0} \quad (4.2-24)$$

$$\implies \chi = \frac{1}{2} \sin^{-1} \frac{S_3}{S_0} \quad (4.2-25)$$

It varies from $\chi = 0^\circ$ (fully linear polarized) to $\chi = 45^\circ$ (fully circular polarized).

4.2.2 Third Harmonic Generation

Third harmonic generation (SHG) is a nonlinear optical process in which three photons with the same frequency simultaneously interact in a nonlinear material to produce a photon with triple the energy, and therefore three times the frequency, of the original photons. The third term on the right side of Equation 4.2-5 defines the THG nonlinear process where E_i , E_j , and E_k are time coincident and degenerate in energy. For incident beams of frequency ω , the THG signal due to pure electric polarization is defined as;

$$P_i(3\omega) = \chi_{ijkl}^{eeee} E_j(\omega) E_k(\omega) E_l(\omega) \quad (4.2-26)$$

THG is allowed in both centrosymmetric and noncentrosymmetric materials.

The THG susceptibility tensor is a tensor of rank-4 whose general form is given by

$$\chi_{ijkl}^{eeee} = \begin{bmatrix} \chi_{x1} & \chi_{x2} & \chi_{x3} \\ \chi_{y1} & \chi_{y2} & \chi_{y3} \\ \chi_{z1} & \chi_{z2} & \chi_{z3} \end{bmatrix}$$

$$\text{With; } \chi_{i1} = \begin{bmatrix} \chi_{ixxx} & \chi_{ixxy} & \chi_{ixxz} \\ \chi_{ixyx} & \chi_{ixyy} & \chi_{ixyz} \\ \chi_{ixzx} & \chi_{ixzy} & \chi_{ixzz} \end{bmatrix}, \chi_{i2} = \begin{bmatrix} \chi_{iyxx} & \chi_{iyxy} & \chi_{iyxz} \\ \chi_{iyyx} & \chi_{iyyy} & \chi_{iyyz} \\ \chi_{iyzx} & \chi_{iyzy} & \chi_{iyzz} \end{bmatrix}, \chi_{i3} = \begin{bmatrix} \chi_{izxx} & \chi_{izxy} & \chi_{izxz} \\ \chi_{izyx} & \chi_{izyy} & \chi_{izyz} \\ \chi_{izzx} & \chi_{izzy} & \chi_{izzz} \end{bmatrix}$$

where $i = x, y, z$.

Knowing each susceptibility tensor element is important to understand the origin of the generated THG signal. For the third-order susceptibility tensor, there are 81 cartesian components, but in THG, all fields are identical, which allows for permutation symmetry in the last three indices *i.e.*, $\chi_{ijkl}^{eeee} = \chi_{iljk}^{eeee} = \chi_{iklj}^{eeee}$ which reduces the number of tensor elements to 54. Further, constraining the THG susceptibility by the materials' structured symmetry reduces the number of independent tensor elements.

4.2.3 Rotational Anisotropy Nonlinear Harmonic Generation

The rotational anisotropy nonlinear harmonic generation is an experimental technique to analyze the change in intensity of the nonlinear signal generated by a material as the polarization of the incoming laser light is rotated. This technique is highly sensitive to the structures and electronic symmetry of the material. It also allows for the determination of the individual tensor elements.

When a laser is incident on a sample, the sample emits a nonlinear signal. The intensity of the emitted signal depends on the angle of polarization of the incident light due to the anisotropy nature of the material structure as given by χ_{ijk} and χ_{ijkl} . By measuring all the components of the susceptibility tensors through various combinations of the incident and emitted polarizations, as well as different scattering geometry, the lattice and electronic symmetries can be identified and resolved statically. They can further be measured as a function of temperature or as a function of time following photoexcitation.

The experimental setup for the rotational anisotropy nonlinear harmonic generation experiment is shown in Figure 4.5.

In this experiment, the beam's polarization was first refined by passing it through a linear wire grid polarizer. Next, to create circularly polarized light, the beam was directed through a quarter-wave plate. A mechanically driven wire grid polarizer further processed the beam, while a long-pass filter was employed to eliminate unwanted wavelengths produced by the optical setup. The spherical mirror then focuses the beam onto the sample, inducing the emission of higher harmonic signals. Reflections from the sample were guided to a D-shaped mirror, then a mechanically driven analyzer and a short-pass filter, which removed the fundamental wavelength and passed the nonlinear response. The experiment data was recorded with the detection of the beam's intensity using a fast-sampling technique based on a data acquisition card [185]. We used the analysis of four polarization configurations using the mechanically driven polarizer and analyzer: (a) corotating and

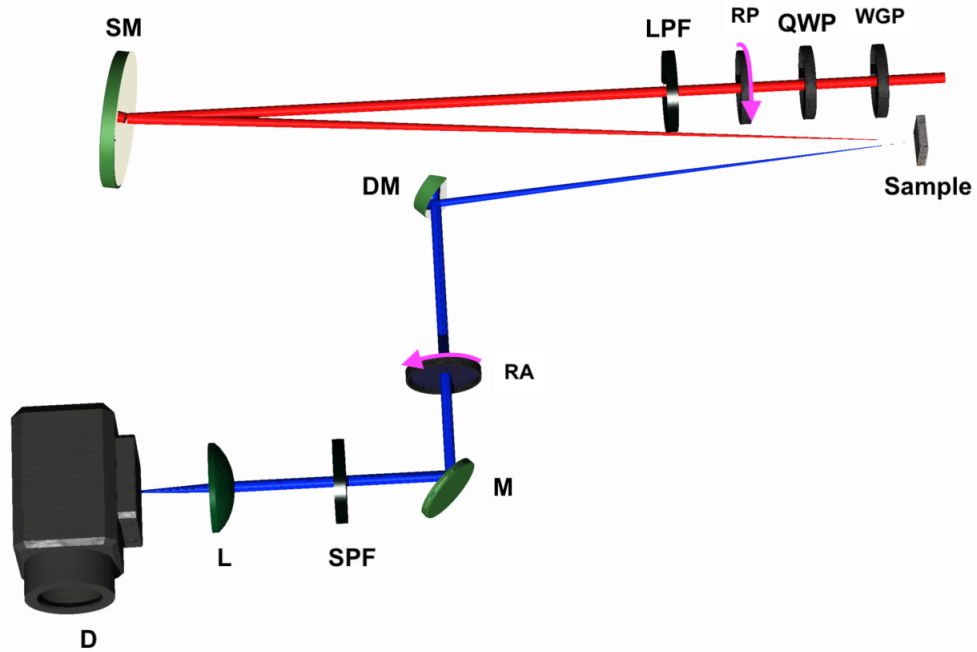


Figure 4.5: Schematic diagram of setup used in rotational anisotropy measurements. Optics are: P - polarizer, QWP - quarter waveplate, LP - longpass filter, SM - spherical mirror, S - sample, DM - D-shaped mirror, A - analyzer, M- mirror, SP - shortpass filter, L - lens, D - detector.

parallel, (b) corotating and perpendicular, (c) incoming rotation with fixed horizontal outgoing, and (d) incoming rotation with fixed vertical outgoing.

In Chapter 5, RA-SHG technique used to study nonlinear response on LnAlSi ($\text{Ln} = \text{La}, \text{Ce}, \text{Pr}$ and Nd) where I observe the magnetic dipole transition from the trivalent state of Ln^{+3} and in Chapter 6 RA-THG study reveals the hidden order phase transition on 1T-TiSe_2 .

4.3 Photogalvanic Effect

The photogalvanic effect (PGE) is a second-order nonlinear optical material response in which DC current is generated due to the mixing of two degenerate fields driven by light-induced electron excitation [99]. The direction of flow of the generated current depends on

crystalline symmetry and the nature of the incident of light on noncentrosymmetric materials. For example, PGE current in structurally chiral media flows in opposite directions with different helicity of light. Similar to an SHG, the PGE is only allowed in noncentrosymmetric materials and is defined in a similar manner as SHG.

The PGE photocurrent j_i is defined as,

$$j_i = \beta_{ijk} E_j E_k^* \quad (4.3-27)$$

Since DC current cannot be an imaginary quantity, the photogalvanic tensor β_{ijk} must be Hermitian in its last two indices, i.e., $\beta_{ijk} = \beta_{ikj}^*$. The Hermitian photogalvanic tensor β_{ijk} includes all information about PGE and can be decomposed into a real symmetric part β_{ijk}^s and an imaginary antisymmetric part β_{ijk}^{as} as;

$$\beta_{ijk} = \beta_{ijk}^s + i\beta_{ijk}^{as}$$

where β_{ijk}^{as} is antisymmetric in the last two indices, which are the direction of the applied field.

The photogalvanic current can be thus rewritten as,

$$j_i = \beta_{ijk}^s E_j E_k^* + i\beta_{ijk}^{as} E_j E_k^* \quad (4.3-28)$$

or

$$j_i = \beta_{ikj}^s E_k E_j^* + i\beta_{ikj}^{as} E_k E_j^*$$

For linearly polarized light, the electric field is purely real. Thus, $E_j E_k^* = E_k E_j^* = E_j E_k$ and the asymmetric parameter is $\beta_{ikj}^{as} = -\beta_{ijk}^{as}$. Thus, we can rewrite the condition for linear polarized incidence beam from equation 4.3-28 as,

$$\beta_{ijk}^s E_j E_k + i\beta_{ijk}^{as} E_j E_k = \beta_{ijk}^s E_j E_k - i\beta_{ijk}^{as} E_j E_k \quad (4.3-29)$$

This condition holds only if the assymetic term $\beta_{ijk}^{as} = 0$. Thus, only the real part of the photogalvanic tensor β_{ijk}^s contributes linearly polarized light. The symmetric tensor β_{ijk}^s describes the linear photogalvanic effect (LPGE) current, and its direction depends on the polarization direction of the incidence light as well as crystalline symmetry and gives the pattern of rotational anisotropy of the flow of current.

The circular photogalvanic effect (CPGE) is defined from the the imaginary asymmetric part $i\beta_{ijk}^{as}E_jE_k$ of the photogalvanic current where the antisymmetric parameter β_{ijk}^{as} must satisfy the condition $\beta_{iij}^{as} = 0$. We can explicitly write out the i^{th} component of the CPGE response as,

$$j_i^{cpge} = i \sum_{j \neq k} \beta_{ijk}^{as} E_j E_k^* \quad (4.3-30)$$

$$= \frac{i}{2} \sum_{j \neq k} \beta_{ijk}^{as} (E_j E_k^* - E_k E_j^*) \quad (4.3-31)$$

$$= \frac{i}{2} \sum_{j \neq k} \sum_{p,r} \beta_{ijk}^{as} (\delta_{jp} \delta_{kr} - \delta_{jr} \delta_{kp}) E_p E_r^* \quad (4.3-32)$$

$$= \frac{i}{2} \sum_{j \neq k} \sum_{p,q,r} \beta_{ijk}^{as} \epsilon_{qmn} \epsilon_{qab} E_p E_r^* \quad (4.3-33)$$

$$= \frac{i}{2} \sum_{j \neq k} \sum_{p,q,r} \beta_{ijk}^{as} \epsilon_{qmn} (\mathbf{E} \times \mathbf{E}^*)_q \quad (4.3-34)$$

$$= \beta_{iq}^{cpge} (\mathbf{E} \times \mathbf{E}^*)_q \quad (4.3-35)$$

Where ϵ_{ijk} is the Levi-Civitas tensor.

The CPGE tensor β_{iq}^{cpge} is purely imaginary. The index i gives the direction of the photocurrent, while q defines the propagation of the incident light through $(\mathbf{E} \times \mathbf{E}^*)_q$

Figure 4.6 shows a schematic experimental geometry we used to measure the LPGE and CPGE currents from the bulk of the structurally chiral Weyl semimetal PdGa, which is discussed in Chapter 8.

The femtosecond pulses used induce photocurrent in PdGa samples, typically lasting for a few picoseconds, which generates THz frequency. The emitted THz field was gathered

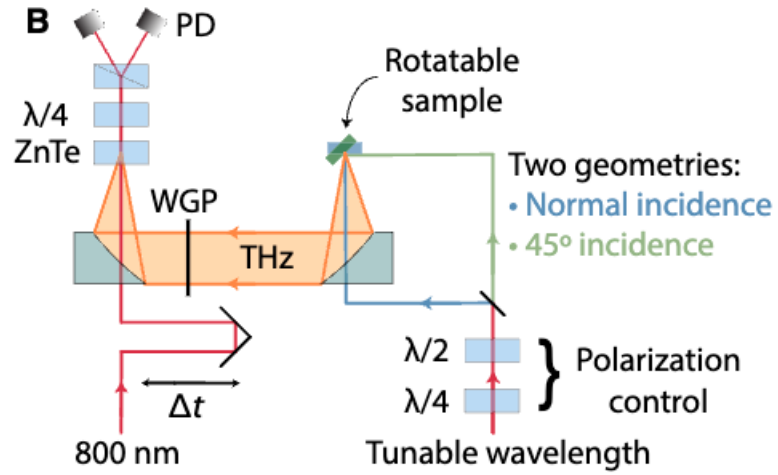


Figure 4.6: Schematic experimental geometry for THz emission spectroscopy measurement. Figure taken from Ref. [105].

and aligned using off-axis parabolic reflectors before being focused on ZnTe. The electro-optic sampling technique was utilized to quantify the terahertz electric field generated from the sample.

CHAPTER 5

QUANTUM INTERFERENCE-DRIVEN NONLINEAR ELECTROMAGNETICALLY INDUCED CHIRALITY IN THE LnAlSi ($\text{Ln}=\text{La, Ce, Pr AND Nd}$) WEYL SEMIMETALS

In this chapter, we present a spectroscopic second harmonic generation (SHG) study of the LnAlSi ($\text{Ln}=\text{La, Ce, Pr, Nd}$) series of magnetic Weyl semimetals, a material group introduced in Chapter 2. The LnAlSi series is paramagnetic at room temperature with each member, except for LaAlSi , hosting a different magnetically ordered phase at low temperatures [107, 110, 186, 187]. While the coexistence of magnetism and topological order is an important focus of study, here we are concerned with the Ln^{+3} trivalent lanthanides that host strong magnetic dipole (MD) transitions [188]. Generally, in solids, the electric component of light drives electric dipole (ED) transitions, while the magnetic component is responsible for drives the MD transition. From the classical point of view, the electric field induces a radiating polarization P_i (i.e., electric dipole moment per unit volume), and the magnetic field creates a radiating magnetization M_i (i.e., magnetic dipole moment per unit volume).

However, under special circumstances, the electric field can induce magnetization, and the magnetic field can induce polarization. There are many sources of this so-called magnetoelectric effect whose consequences may be observed statically as in multiferroic systems [20] or at optical frequencies in metamaterials or in specially prepared ordered states [189], where a form of emergent electromagnetic chirality can be realized. In condensed phase

systems, the former has typically been observed, with the latter reserved for atoms in the gaseous phase. Here, we describe how such a nonlinear magnetoelectricity is observable in condensed matter with the consequence of emergent nonlinear electromagnetic chirality due to the presence of strong MD transitions.

In order to study these MD transitions, we conducted optical SHG measurements over the 1.24 - 1.78 eV incoming photon energy range in the samples LaAlSi, CeAlSi, PrAlSi, Pr_{1-x}Nd_xAlSi and NdAlSi. Our data are consistent with a strong MD transition resonance at ~ 1.5 eV in the paramagnetic phase of all samples studied. Importantly, the energy-resolved resonance spectra revealed a quantum interference between the narrow-band f orbitals hosting the MD transition and a broadband ED active resonance that we deduce from density functional calculations [190] that are derived from d - and p -orbitals. This resonance takes the form of a Fano lineshape in the MD SHG susceptibility χ_{zxy}^{eem} for all five samples studied. Comparison of our fitted data with first-principles atomic calculations on free trivalent lanthanide ions revealed that the MD resonance derived from unassigned transitions in LaAlSi and CeAlSi, the excited state to excited state $^1D_2 \rightarrow ^3F_2$ transition in PrAlSi [191] and the $^4I_{\frac{9}{2}} \rightarrow ^2H_{\frac{9}{2}}$ ground state to excited state transition in NdAlSi [191]. The hybridization between energy band that leads to the Fano resonance was also observed to drive a second-order analog to the phenomenon of electromagnetically induced chirality (EIC) wherein an achiral medium obeys the constitutive relations of chiral media. Polarimetry measurements of the emitted SHG in the spectral range of the MD resonance were approximately half circularly polarized from near-normal linearly polarized incident light for all samples studied.

5.1 Introduction

The magnetoelectric effect is an induced magnetization in response to an applied electric field that can spring from either a trivial or topological origin. In topologically ordered matter, its origin lies in the Chern-Simons term that gives rise to the axion electrodynamics

that produces magnetoelectric cross-coupling in Maxwell's Equations. Among the topologically trivial sources of magnetoelectricity, one more common to atomic systems is the coupling between a resonant ED transition and a resonant MD transition, which must be driven by an external coupling field [19]. The result of this magnetoelectric cross-coupling is that the medium adopts the constitutive relations of chiral media, giving rise to the phenomenon of EIC [65], a close cousin of electromagnetically induced transparency.

To be more precise, we begin by considering the linear electromagnetic constitutive relation. In a chiral medium, the polarization and magnetization are given by [192]

$$P_i = \chi_{ij}^{ee} E_j + \chi_{ij}^{em} H_j \quad (5.1-1)$$

$$M_i = \chi_{ij}^{mm} H_j + \chi_{ij}^{me} E_j \quad (5.1-2)$$

where the linear susceptibilities χ_{ij}^{ee} and χ_{ij}^{mm} relate to the permittivity and permeability respectively. χ_{ij}^{me} denotes the tensorial coupling coefficient between the electric field and the induced magnetization, while χ_{ij}^{em} relates the incident magnetic field to the induced polarization.

EIC has mainly been investigated in the context of metamaterials since the magnetoelectric cross-coupling term in Equations 5.1-1 and 5.1-2 are input to the refractive index. As such, these terms can induce a negative refractive index without requiring a negative permittivity under coherently controlled circumstances [21]. Realization of this effect in the solid state has been limited to collective excitations at linear order [19]. At nonlinear order, magnetoelectric effects have only been observed in magnetically ordered systems, such as Cr_2O_3 [193], but never as an intrinsic material property. The corresponding electromagnetic effect has also not yet been observed.

The lack of these intrinsic effects in solids is due to the fact that MD transitions are several orders of magnitude weaker than their electric dipole (ED) counterparts, making them difficult to observe. Since MDs occur between two quantum states that do not fol-

low the ED selection rules, their excited state lifetimes are often longer than those associated with ED transitions, leading to proposals that they could be useful to real-world applications for novel lasing media [194, 195], while the sensitivity of MD transitions to magnetic fields could permit their use in optically active magnetic field sensors [196–201]. Furthermore, strong resonant MD transitions can create strong dispersive features in the frequency-dependent magnetic permeability $\mu(\omega)$, which could aid in the design of optical frequency metamaterials applicable to numerous device applications [202–207].

Despite the interest in discovering and developing resonant materials for MD transitions, separating an MD response from the overwhelming ED background is extremely difficult in linear response since the intensity radiation dipole patterns of the two are identical [208]. The earliest methods comprised a polarization selection technique that depended upon the difference in the parity of the emitted electromagnetic field on opposite sides of the radiating atom; on two sides of an ED radiator, the electric field phase difference is $\psi = 0$, while for MD transitions, $\psi = \pi$, permitting their observation through interferometry [209]. More recent measurements on atomic systems have relied on structured light in which the very central region of a radially polarized beam comprised a null electric field component while simultaneously supporting a strong magnetic field that was observed to drive ${}^7F_0 \rightarrow {}^5D_1$ transitions in Eu^{3+} atoms [18]. Measurement of MD radiation from bulk crystalline materials is even more challenging, however, since extensive hybridization between various atomic orbitals in these systems can occlude MD selection rules, leaving ED transitions to dominate. However, one effective scheme, proposed by T. H. Taminiau et al., [210] and R. A. DeCrescent et al., [211] uses an energy and momentum resolved spectroscopic technique to observe the difference between the cross-sectional emission profiles of ED and MD emission.

The nonlinear optical tool of rotational anisotropy-second harmonic generation (RA-SHG) can allow for a clear separation between MD and ED transitions in condensed phase systems through a simple symmetry analysis of the polarization dependence of the emitted

fields. Briefly, SHG is a nonlinear optical process in which two photons of energy ω combine within a medium to produce a single photon of energy 2ω . This response is usually written as $P_i(2\omega) = \chi_{ijk}^{eee} E_j(\omega) E_k(\omega)$, where the χ_{xyz}^{eee} is the nonlinear optical susceptibility, subscripts $i, j, k = x, y, z$ determine the field polarization, the superscript eee refers to the three contained ED transitions, $P_i(2\omega)$ represents the radiating polarization at the second harmonic frequency 2ω , and the $E_j(\omega)$ represents the incoming electric fields. When SHG is measured as a function of rotation of the incoming electric field polarization angle, emitted polarization angle, or the sample crystallographic axes relative to the scattering plane, the resulting rotational anisotropy (RA) patterns are typically highly constrained by the material's point group symmetry with higher specificity than afforded by linear measurement. Such RA-SHG measurements have been used to determine crystallographic, magnetic, and exotic electronic ordering symmetries of a wide array of materials [20, 212–214]. They can also provide a tool easily separating ED and MD transition.

Implicit in the relationship between polarization and an electric field is that all three electronic transitions are mediated by ED transitions deriving from the polar ED vector operator $\mathbf{p}_i = e\mathbf{r}_i$ ($i = x, y, z$), fixes the symmetry of the nonlinear optical susceptibility tensor χ_{xyz}^{eee} as polar. However, MD transitions may also contribute to the nonlinear optical susceptibility through the magnetic field $H_i(\omega)$ and/or through the radiating magnetization $M_i(2\omega)$ in a form of nonlinear magnetoelectricity. Microscopically, magnetic dipole transitions are mediated by the axial magnetic dipole operator given in terms of the orbital angular momentum operator \mathbf{L} and spin momentum operator \mathbf{S} as $\mathbf{L} + 2\mathbf{S}$. Neglecting quadrupolar contributions to SHG, the full relationship between the incoming and outgoing radiation is thus given by

$$P_i = \chi_{ijk}^{eee} E_j E_k + \chi_{ijk}^{eem} E_j H_k + \chi_{ijk}^{emm} H_j H_k \quad (5.1-3)$$

$$M_i = \chi_{ijk}^{mee} E_j E_k + \chi_{ijk}^{mem} E_j H_k + \chi_{ijk}^{mmm} H_j H_k \quad (5.1-4)$$

where each m superscript represents a MD transition while e the superscript refers to an ED transition. Significantly, Equations 5.1-3 and 5.1-4 represent the next (second) order terms in the expansion of the constitutive relations given by Equations 5.1-1 and 5.1-2. Thus, a chiral medium is expected to respect Equations 5.1-3 and 5.1-4, which we now proceed to examine more closely.

The overall response must conserve axial or polar symmetry on either side of Equations 5.1-3 and 5.1-4. Thus, SHG deriving from an odd number of axial input fields will result in an axial susceptibility tensor if the emission is via a polarization P_i and a polar susceptibility tensor if emission is via a radiating magnetization M_i . Since axial tensors must satisfy the transformation criterion $\chi_{lmn} = \det|a| a_{il} a_{jm} a_{kn} \chi_{ijk}$, where $\det|a|$ refers to the determinant of the transformation tensor a_{ij} , axial nonlinear susceptibility tensors in achiral point groups may comprise independent components different from the corresponding polar response, even permitting centrosymmetric point groups to support second-order optical processes that would otherwise be forbidden.

MD transitions are typically weaker than ED transitions by a factor of the fine structure constant squared, i.e., $\alpha^2 \approx (\frac{1}{137})^2 \approx 5 \times 10^{-5}$ [215]. Thus, responses that involve two or more MD transitions are small enough that they may be ignored in the absence of coincident resonance. Thus the second order constitutive relations are, to an excellent approximation

$$P_i = \chi_{ijk}^{eee} E_j E_k + \chi_{ijk}^{eem} E_j H_k \quad (5.1-5)$$

$$M_i = \chi_{ijk}^{mee} E_j E_k \quad (5.1-6)$$

which are accepted as the lowest order terms in the SHG constitutive relations for structurally chiral media with approximation which are analogous to those at linear order defined by Equations 5.1-1 and 5.1-2 [183].

At linear order, it is known that the constitutive relations the Equations 5.1-1 and 5.1-2 can be imposed upon atoms using external laser fields that couple MD and ED transi-

tions. However, such coupling can exist naturally in condensed phase systems. Here, we report on the observation of a nonlinear form of EIC driven by MD transitions of equal strength to ED transitions in the SHG responses of the LnAlSi (Ln = La, Ce, Pr, Nd) family of Weyl semimetals. Although of no consequence here, these materials, whose band structures harbor both type I and type II Weyl points, can also host various forms of unconventional magnetic order, including a canted antiferromagnetic phase in CeAlSi [186] and a nesting-driven spin-density wave order in NdAlSi that onsets at 7.2(1) K and transitions from incommensurate to commensurate at 3.3(1) K [107]. While prior study has examined showing the impact of magnetic order on SHG emission [216–218], here we exclusively study the paramagnetic phase in order to demonstrate an intrinsic effect of the band structure. Due to the quantum interference between the f -orbitals probed by the MD transition and the highly dispersive bands in LnAlSi that respond to ED transition and derive from d and p orbitals, we observed a Fano resonance in the MD spectrum using RA-SHG. As a consequence, polarimetry of the emitted SHG at or near the resonance energy revealed that it comprised up to 50% circularly polarized light depending upon the input linearly polarized fundamental field at near normal incidence. Taken together, these observations describe a novel, nonlinear form of EIC at second order that is intrinsic to this material system.

5.2 Experiment

A schematic representation of the setup used in this study is shown in Figure 5.1. The output of a regeneratively amplified Ti:sapphire laser seeded a TOPAS Twins with continuously tunable output from 490 nm - 16.6 μm . The setup used here is identical to that described in Ref. [92]. As in the Reference, the beam was focused at near-normal incidence (angle of incidence $< 1^\circ$) with a large spot size to enable high photon yield at relatively low incident fluence.

First, the polarization state of the beam was purified using a linear wire grid polarizer (Thorlabs, WP25M-UB). A quarter wave plate (Thorlabs, AHWP05M-980) made the polarization state circular. A mechanically driven wire grid polarizer spinning at 5 Hz produced a time varying incoming polarization angle ϕ . In order to suppress wavelengths spuriously generated by the optics, a long-pass filter (Thorlabs, FELH0700) was used. A spherical mirror was used to focus the beam onto the sample in order to avoid the effects of chromatic dispersion. The reflected beam from the sample was directed towards a D-shaped mirror and passed through another mechanically driven analyzer. After passing through the analyzer, the beam is passed through a shortpass filter to eliminate the fundamental wavelength while preserving the SHG response from the sample. Finally, the beam was measured by a photomultiplier tube (Hamamatsu, R12829), and the intensity was recorded using a data acquisition card-based fast sampling technique [185].

The four polarization configurations we used to measure the emitted SHG were: (a) incoming and outgoing polarizations co-rotating and parallel ($I_{\parallel}^{2\omega}$); (b) incoming and outgoing polarizations co-rotating and perpendicular ($I_{\perp}^{2\omega}$); (c) incoming polarization rotating, outgoing polarization fixed at horizontal ($I_H^{2\omega}$); (d) incoming polarization rotating, outgoing polarization fixed at vertical ($I_V^{2\omega}$).

We studied high-quality, as grown single crystal samples of LaAlSi, CeAlSi, PrAlSi, Pr_{0.8}Nd_{0.2}AlSi and NdAlSi. Details of crystal growth and quality are provided in Refs. [107, 186, 219]. Since normal incidence on the (001) face did not produce SHG by symmetry, we studied the large (101) facets. The bulk polar and axial SHG susceptibilities $\chi^{(2)}$ for materials in this space group are given by

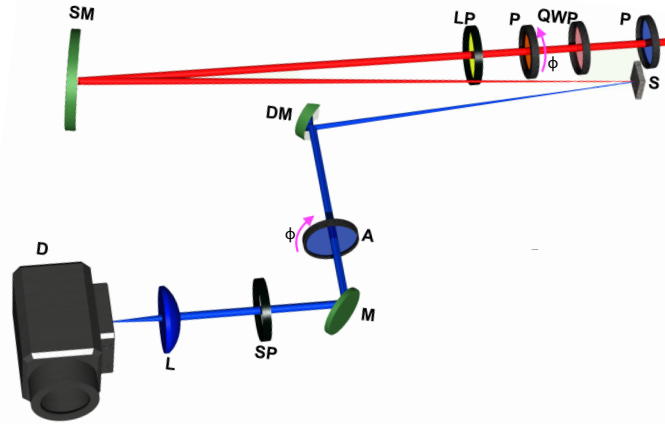


Figure 5.1: Schematic diagram of setup used in SHG measurements. Optics are: P - polarizer, QWP - quarter waveplate, LP - longpass filter, SM - spherical mirror, S - sample, DM - D-shaped mirror, A - analyzer, M - mirror, SP - shortpass filter, L - lens, D - detector.

$$\chi_{ED}^{eee} = \begin{bmatrix} \begin{pmatrix} 0 \\ 0 \\ xxz \end{pmatrix} \\ \begin{pmatrix} 0 \\ 0 \\ 0 \end{pmatrix} \\ \begin{pmatrix} xxz \\ 0 \\ 0 \end{pmatrix} \\ \begin{pmatrix} 0 \\ zxx \\ 0 \end{pmatrix} \\ \begin{pmatrix} 0 \\ 0 \\ 0 \end{pmatrix} \\ \begin{pmatrix} 0 \\ 0 \\ xxz \end{pmatrix} \\ \begin{pmatrix} zxx \\ 0 \\ 0 \end{pmatrix} \\ \begin{pmatrix} 0 \\ zxx \\ 0 \end{pmatrix} \\ \begin{pmatrix} 0 \\ 0 \\ zzz \end{pmatrix} \end{bmatrix} \quad \chi_{MD}^{eee} = \begin{bmatrix} \begin{pmatrix} 0 \\ 0 \\ 0 \end{pmatrix} \\ \begin{pmatrix} 0 \\ 0 \\ xzy \end{pmatrix} \\ \begin{pmatrix} 0 \\ xyz \\ 0 \end{pmatrix} \\ \begin{pmatrix} 0 \\ 0 \\ -xzy \end{pmatrix} \\ \begin{pmatrix} 0 \\ 0 \\ 0 \end{pmatrix} \\ \begin{pmatrix} -xyz \\ 0 \\ 0 \end{pmatrix} \\ \begin{pmatrix} 0 \\ -zxy \\ 0 \end{pmatrix} \\ \begin{pmatrix} zxy \\ 0 \\ 0 \end{pmatrix} \\ \begin{pmatrix} 0 \\ 0 \\ 0 \end{pmatrix} \end{bmatrix}$$

The polar signal deriving from ED sources is given as a function of incoming polarization angle ϕ for the (101) facet as

$$I_{\parallel}^{eee}(\phi) = \frac{1}{32} \cos^2(\phi) [(-2\chi_{xxz}^{eee} - \chi_{zxx}^{eee} + \chi_{zzz}^{eee}) \cos(2\phi) + 6\chi_{xxz}^{eee} + 3\chi_{zxx}^{eee} + \chi_{zzz}^{eee}]^2 \quad (5.2-7)$$

$$I_{\perp}^{eee}(\phi) = \frac{1}{8} \sin^2(\phi) [(-2\chi_{xxz}^{eee} + \chi_{zxx}^{eee} + \chi_{zzz}^{eee}) \cos^2(\phi) + 2\chi_{zxx}^{eee} \sin^2(\phi)]^2 \quad (5.2-8)$$

$$I_H^{eee}(\phi) = \frac{1}{8} [(2\chi_{xxz}^{eee} + \chi_{zxx}^{eee} + \chi_{zzz}^{eee}) \cos^2(\phi) + 2\chi_{zxx}^{eee} \sin^2(\phi)]^2 \quad (5.2-9)$$

$$I_V^{eee}(\phi) = 2 [\chi_{xxz}^{eee} \sin(\phi) \cos(\phi)]^2 \quad (5.2-10)$$

while the axial response is given by

$$I_{\parallel}^{em}(\phi) = \frac{1}{4} [(\chi_{xzy} + \chi_{zxy}) \cos(\phi)]^2 \quad (5.2-11)$$

$$I_{\perp}^{em}(\phi) = \frac{1}{4} [(\chi_{xzy} - \chi_{zxy}) \sin(\phi)]^2 \quad (5.2-12)$$

$$I_H^{em}(\phi) = \frac{1}{16} (-\chi_{xyz} + \chi_{xzy} + 2\chi_{zxy} + (\chi_{xyz} + \chi_{xzy}) \cos(2\phi))^2 \quad (5.2-13)$$

$$I_V^{em}(\phi) = \frac{1}{16} [(\chi_{xyz} + \chi_{xzy}) \sin(2\phi)]^2 \quad (5.2-14)$$

In contrast with the polar SHG tensor elements χ_{ijk}^{eee} , the axial elements χ_{xyz}^{em} , and χ_{xzy}^{em} are distinct because permutation symmetry is not allowed between E_i and H_j fields.

Rotational anisotropy data were acquired over the 1.1 – 1.8 eV incoming photon energy range. Representative data at a wavelength $\lambda = 800$ nm (1.5 eV) are shown in Figure 5.3a for the material NdAlSi. We observed a strong SHG response on par with the standard candle material GaAs. Data for all the polarization configurations described above were taken in quick succession (all traces were acquired within 1.5 minutes of one another) without realignment and with negligible laser drift, permitting a global fit to a single set of parameters.

A global fit using the parameters of the ED only response, shown in Figure 5.3b, clearly cannot describe the data alone, and the individual traces also cannot be fit by ED only responses separately. In order to rule out a structural origin of the response, we relaxed the point group symmetries of the material to its nearest structural subgroups, i.e., C_4 , C_{2v} , and C_s and repeated this procedure. The results of these fits are presented in the Appendices, where we demonstrate that we were not able to account for the effects using any lower symmetry candidate point group. This is highly suggestive of an axial, resonant response, which we ascribe to MD transitions.

5.3 Results and discussion

5.3.1 MD Transition and Fano Resonance Effect

In order to isolate the MD response, we fit the raw data at the lower bound in the studied energy interval with a single set of fitting parameters for the χ_{ijk}^{eee} that provided good fits in the ED channel (representative fits shown in Figure A.1 of the appendix). In the middle of the studied energy interval, we used floating MD parameters to fit the raw data along with the bounded ED fitting parameters obtained at the lower bound in the studied energy interval. In so doing, we have assumed that the ED contribution does not exhibit a large resonance or change appreciably across this energy range. This approach is also consistent with a π -phase shift between the ED and MD responses, as would be expected when the latter is at optical resonance while the former is not; it is also consistent with previous studies of SHG on individual ions where a magnetic resonance was evident in a phase shift for only the MD component of the response [220].

We may also justify our data reduction procedure in the following way:

In a simple atomic picture, SHG derives from a series of optical transitions between ground state $|g\rangle$, intermediate excited state $|n'\rangle$, and excited state $|n\rangle$, giving an axial tensor element χ_{ijk}^{em} as

$$\chi_{ijk}^{em} \propto \sum_{g,n,n'} \left[\frac{(\hat{P}_i)_{gn}(\hat{P}_j)_{nn'}(\hat{M}_k)_{n'g}}{(2\omega - \omega_{ng})(\omega - \omega_{n'g})} + \dots \right] p_g^{(0)} \quad (5.3-15)$$

where, e.g., $(\hat{P}_i)_{gn} = e\langle g|\mathbf{x}_i|n\rangle$ is an electric dipole emission between states $\langle g|$ and $\langle n|$ polarized in the i direction, and $(\hat{M}_k)_{n'g} \propto \langle n'|\mathbf{L}_k + 2\mathbf{S}_k|g\rangle$ is a magnetic dipole mediated absorption between states $|g\rangle$ and $|n\rangle$ polarized in k . $p_g^{(0)}$ represents the thermally controlled equilibrium population of the ground state. Thus, the nonlinear response can encode individual linear responses within it, e.g., the MD matrix element $(M_k)_{n'g}$. In other words, χ_{zxy}^{em} is linear in the MD transition provided the spectral features encoded in the ED transition vary slowly over the MD resonance, this is a means of conducting a quasi-linear spectroscopy.

We thus proceed to analyze the MD transition in linear response, meaning that we will fit the MD energy-resolved spectra to linear spectroscopic lineshapes. The asymmetric Fano lineshape is described by the Breit–Wigner–Fano (BWF) function

$$I(E) = I_0 \left[1 - \frac{(q \frac{\Gamma_{res}}{2} + E - E_{res})^2}{(\frac{\Gamma_{res}}{2})^2 + (E - E_{res})^2} \right] \propto \left[1 - \frac{(q + \epsilon)^2}{1 + \epsilon^2} \right], \quad \epsilon = \frac{2(E - E_{res})}{\Gamma_{res}} \quad (5.3-16)$$

Where q is a dimensionless parameter that characterizes the nature of the interaction between a discrete resonance and a continuum. Γ_{res} and E_{res} are the linewidth and central energy of discrete resonance, respectively. Its sign and magnitude are determined by the separation in energy between the discrete MD resonance and the central energy of the interfering continuum. When q is negative, the spectrum's structure shows a dip on one side of the peak and a rise on the other side, while $q = 0$ results in a symmetric Lorentzian lineshape as shown in Figure 5.2.

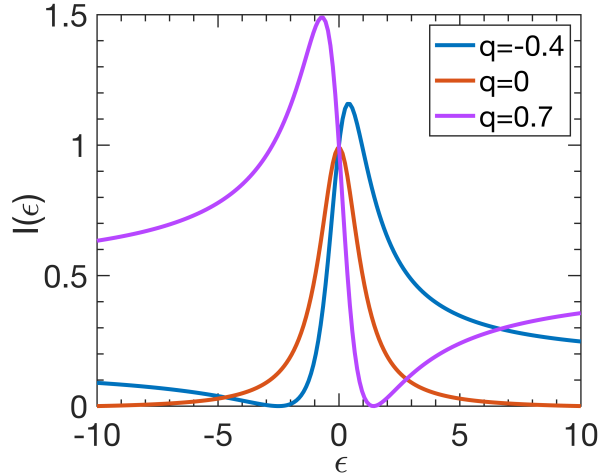


Figure 5.2: Plot of the Fano lineshape Equation 5.3-16 with energy ϵ and asymmetric parameters $q = -0.4$ (blue), $q = 0$ (red) and $q = 0.7$ (purple). Changing the sign of the q parameter changes the nature of the asymmetry. For $q = 0$, the Fano lineshape reduces to the Lorentzian lineshape.

Using Equations 5.2-7 - 5.2-14, we obtained an excellent fit for the MD parameters using global fit parameters and bounded ED values. A representative example of these fits is shown in Fig. 5.3c. This process was repeated across the entire energy range to produce

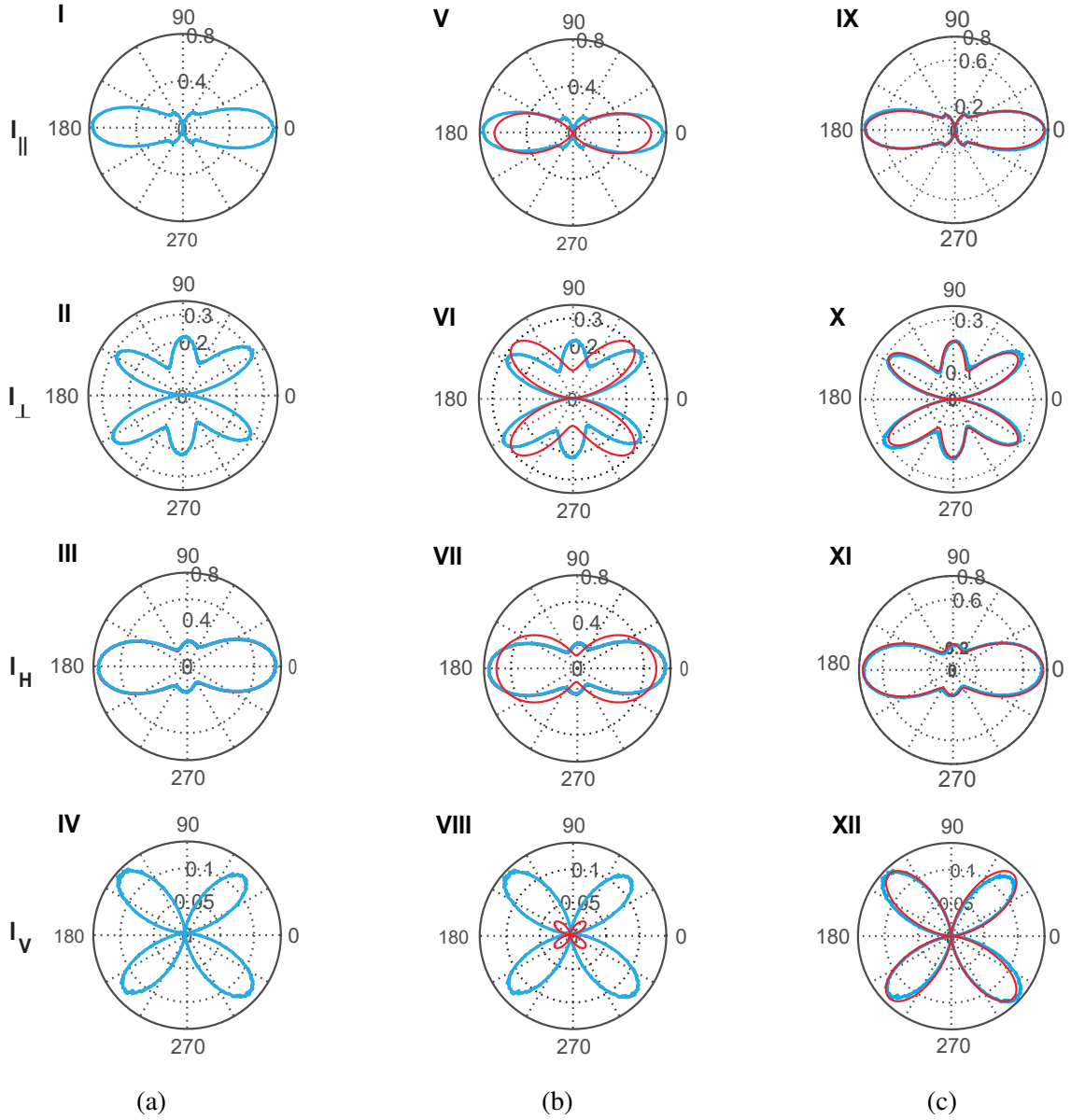


Figure 5.3: Second-harmonic generation data (blue) and fit (red) for NdAlSi. (a) Second-harmonic generation (SHG) data for incoming wavelength 800 nm and outgoing wavelength 400 nm. (b) Data and fits to only the bulk ED SHG in the C_{4v} point group as given by Equations 5.2-7 - 5.2-10 for (V) $I_{||}$, (VI) I_{\perp} , (VII) I_H , and (VIII) I_V . (c) Data and fits to both bulk ED and MD SHG in the C_{4v} point group as given by Equations 5.2-7 - 5.2-10 and 5.2-11 - 5.2-14 for (IX) $I_{||}$, (X) I_{\perp} , (XI) I_H , and (XII) I_V . Both ED and MD responses are required to fit the data.

spectra for each of the axial tensor components, shown in Figure 5.4. A resonance peak is clearly evident for all tensor components and all materials, most notably for the tensor component χ_{zxy}^{em} , which is driven by an MD transition oriented along the crystallographic

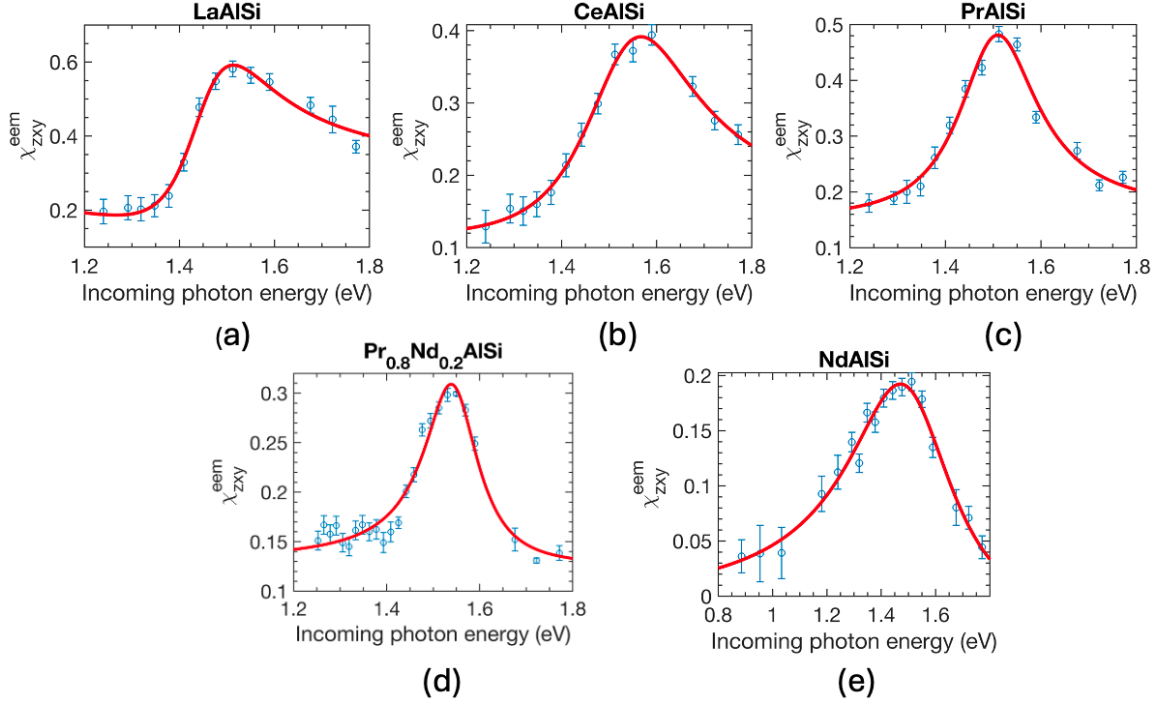


Figure 5.4: Experimentally measured spectra with error bars (blue) and Fano fit (red) to the Fano lineshape given by Equation 5.3-16 for magnetic SHG susceptibility χ_{ijk}^{eem} in LnAlSi (Ln = La, Ce, Pr, Pr_{0.8}Nd_{0.2} and Nd).

y-axis and an ED transition along the x -axis with ED radiation emitted along the crystallographic z -axis. The q , Γ_{res} , and E_{res} parameters of the LnAlSi series of materials with MD resonance E_{pred} predicted by C.M. Dodson et al. [191], are shown in Table A.1. We note there was also resonance in the χ_{zzz}^{eee} ED tensor parameter as show in Figure 5.5. This is to be expected for the Fano lineshape. We thus are able to observe the resonance through the excitation and its coupling to either ED or MD transition.

Sample	q	Γ_{res} (eV)	E_{res} (eV)	E_{pred} (eV)
LaAlSi	-0.57	0.21	1.45	-
CeAlSi	-0.25	0.29	1.53	-
PrAlSi	-0.08	0.20	1.50	1.48 [191]
Pr _{0.8} Nd _{0.2} AlSi	0.09	0.14	1.54	-
NdAlSi	0.16	0.47	1.51	1.51 [191]

Table 5.1: Asymmetry parameter (q), resonance linewidth (Γ_{res}), and resonance energy (E_{res}) of magnetic dipole transition χ_{zxy}^{eem} on LnAlSi series of Weyl semimetals. E_{pred} —predicted resonance energy from Ref. [191].

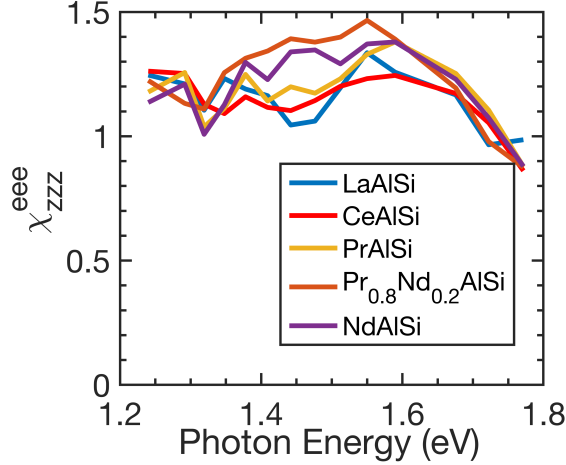


Figure 5.5: Experimentally measured spectra for electric SHG susceptibility χ_{zzz}^{eee} in LnAlSi (Ln = La, Ce, Pr, Pr_{0.8}Nd_{0.2} and Nd). In LnAlSi materials, the resonance observes ~ 1.5 eV due to excitation coupled to both ED and MD.

We compare the asymmetry parameters q of different LnAlSi series materials and observe that it switches sign between the PrAlSi and Pr_{0.8}Nd_{0.2}AlSi, implying that the resonance energy of the continuum lies between the transitions probed in each material. The discrete transition in NdAlSi and Pr_{0.8}Nd_{0.2}AlSi are situated on different sides of continuum's resonance, as shown in the representative Figure 5.6.

Due to the large negative value of q , the transition in LaAlSi lies far below the center of the broad spectrum compared to the other samples studied. The linear dependence of q with atomic number is shown in Figure 5.7 and indicates that q parameters depend on the number of f electrons in trivalent states of rare earth ions.

As LnAlSi crystallizes with the rare earth ion in the trivalent state, we may compare the central energy of the observed MD transitions E_{res} with prior calculations in isolated trivalent rare earth ions as performed by Dodson and Zia [17] and Carnell [221]. We note that only two of the measurements matched the calculations: the $^1D_2 \rightarrow ^3F_2$ spontaneous emission line at 839 nm (1.48 eV) in Pr³⁺ matched the observed MD transition in the SHG response of PrAlSi; in the atomic calculation, this transition's emission rate is the strongest of all calculated. Similarly, the calculated $^4I_{9/2} \rightarrow ^2H_{9/2}$ absorption line at 822 nm

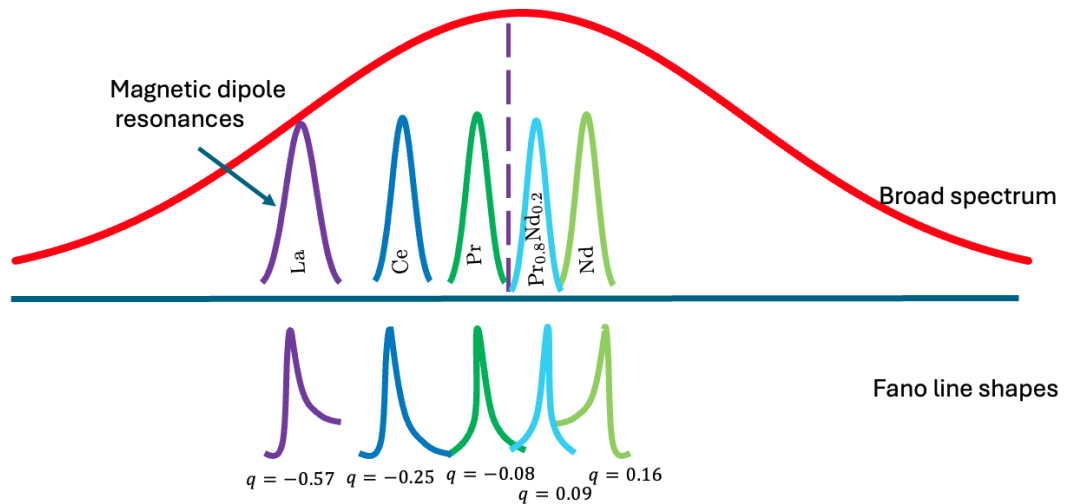


Figure 5.6: Diagram that representing Fano resonance in LnAlSi. LaAlSi has a large negative Fano asymmetric parameter, so its discrete resonance lies far below the resonant energy of the broad continuum. It has the most asymmetric lineshape. CeAlSi and PrAlSi have lower negative asymmetry parameters. Thus, their MD resonance is also lower in energy than the resonance of the interfering continuum. Thus, their lineshapes are asymmetric. Pr_{0.8}Nd_{0.2}AlSi and NdAlSi have positive asymmetry parameters, implying their resonance energy is higher than the background continuum, and their lineshapes tilt in the opposite direction accordingly.

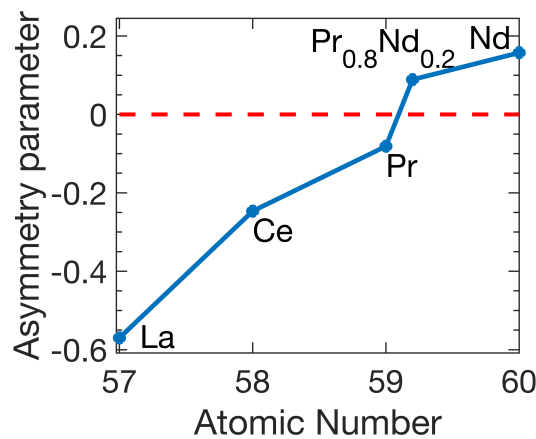


Figure 5.7: Plot for Fano fitting asymmetry parameter q with atomic number. The asymmetry parameter is approximately linearly dependent on the atomic number.

(1.51 eV) in Nd^{3+} has the largest oscillator strength of all calculated in the visible range and matches the measured MD SHG resonance at 1.51 eV. We also note that the measured bandwidth of the MD resonance in PrAlSi is $\sim 2\times$ smaller than in NdAlSi , suggesting that the f -electron-derived band structure of these materials is of narrower bandwidth.

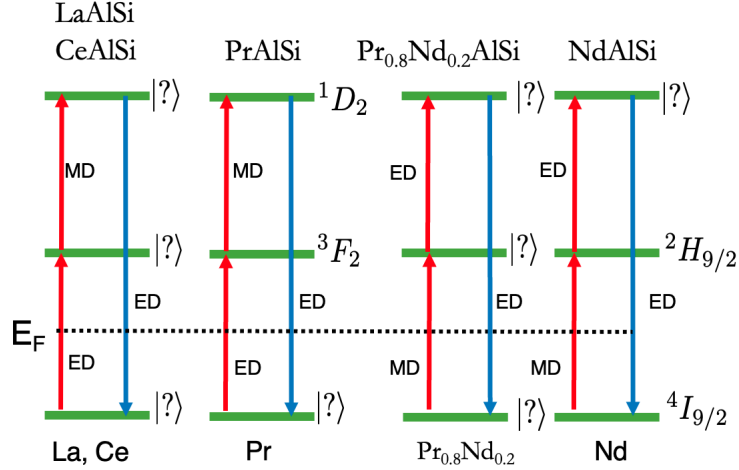


Figure 5.8: Schematic diagram of the electronic transition hierarchy in LnAlSi . In LaAlSi and CeAlSi , the first transition is ED, and the second transition is MD with ED emission. In PrAlSi , the first transition is ED transition, and the second transition is MD transition between ${}^1D_2 \rightarrow {}^3F_2$ with ED emission. In $\text{Pr}_{0.8}\text{Nd}_{0.2}\text{AlSi}$ and NdAlSi the first transition is MD transition, and the second transition is ED transition with ED radiation.

Notably, the measured MD transitions in LaAlSi and CeAlSi do not match atomic calculations; in the former case, the La^{3+} ion has no f -electron occupancy, while in the latter, there is only one allowed transition at the very low photon energy of 0.28 eV. This is highly suggestive that the MD transition occurs either between the intermediate state $|n'\rangle$ and final state $|n\rangle$ or upon emission. Two factors rule out the MD transition occurring upon emission. First, there are no available MD transitions available at ~ 400 nm in these samples. Second, the continuity in the q parameter is highly suggestive that the transition is between the same two energy levels in all ions, the lower energy of which is finally occupied in Nd^{3+} . This observation is further bolstered by measurements on SmAlSi (not shown) where no significant MD contribution exists in this energy range as the upper level involved in the ${}^4I_{9/2} \rightarrow {}^2H_{9/2}$ transition of Nd^{3+} is Pauli blocked in Sm^{3+} . We note that it would only be

possible to experimentally assign the MD transition to either the first or second transitions through the use of coherent two-dimensional spectroscopy [222].

5.3.2 Electromagnetically Induced Chirality (EIC) at Nonlinear Order

The existence of strong MD transition leads to a novel electromagnetic effect, which is a form of EIC at second order. This effect is manifest through the polarization state of the emitted SHG. Since the background ED and resonant MD driven terms interact coherently in the material, their overall effect is to produce two dipoles that radiate with $\frac{\pi}{2}$ phase shift. These two dipoles also do not radiate with their axes aligned, leading to the possibility of elliptically polarized emission that must be characterized by polarimetry. A schematic representation of the polarimeter measurement we used to obtain the Stokes parameters of the beam is shown in Figure 5.9a. This setup comprises a spinning quarter waveplate after the sample to allow measurement of Stokes parameters in a standard manner. The output of the 810 nm laser beam from the OPA was used since all LnAlSi samples were on resonance in the MD channel at this wavelength. As with our SHG measurements, we used linearly polarized light at near-normal incidence (angle of incidence $< 1^\circ$) with a large spot size and measured the emitted SHG.

In our experimental setup, the beam passed through a linear wire grid polarizer (Thorlabs, WP25M-UB) to purify the beam's incoming polarization state. A 30 cm lens (Thorlabs, LA1484-B) was used to focus the beam onto the sample at near-normal incidence. The reflected fundamental and emitted SHG were directed toward a shortpass filter (Thorlabs, FESH0500, and FBH400-40) to eliminate the fundamental wavelength while preserving the nonlinear response from the sample. Then, the beam was passed through a true zero-order quarter-wave plate (Thorlabs, WPQ05ME-405), spinning at 5 Hz and then passed through a fixed wiregrid polarizer. Finally, the beam was collected by a Hamamatsu R12829 photomultiplier tube, and the intensity was recorded using a data acquisition card-based fast sampling technique [185]. Using a mechanically driven polarizer and analyzer, data were

measured by varying the incoming linear polarization angle of the incident beam on the sample. Fits to these data, described below, allowed for extraction of the Stokes parameters for the emitted SHG.

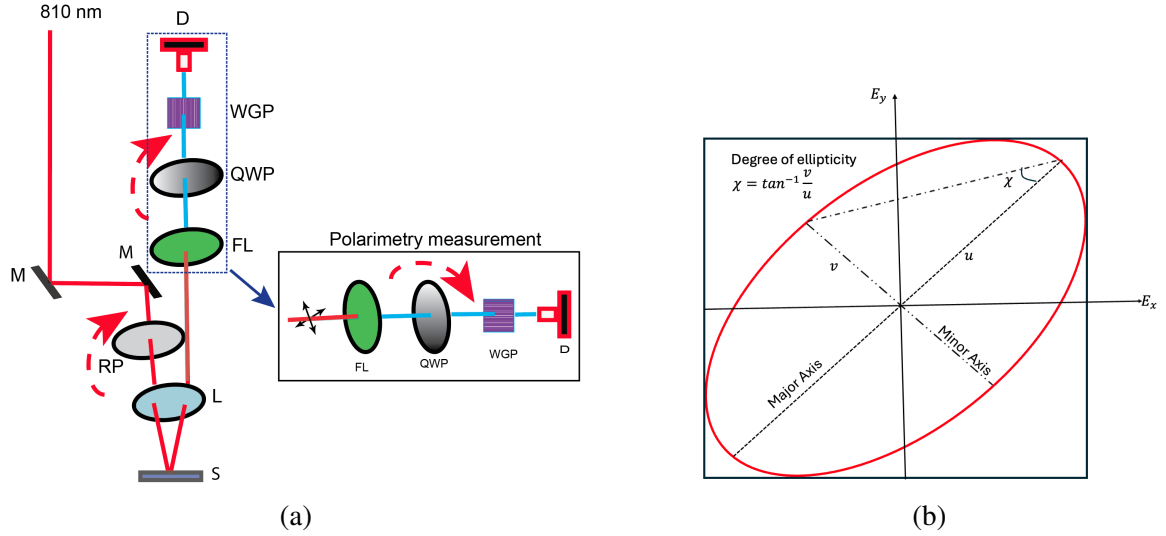


Figure 5.9: (a) Schematic diagram of the setup used in polarimetry measurements to determine the polarization state of SHG emitted from LnAlSi at normal incidence. Optics are: M - mirror, RP - rotating polarizer, S - sample, L - lens, BPF - bandpass filter, QWP - quarter waveplate, WGP - wire grid polarizer, D - detector. (b) Diagram defining the measured polarization state of the emitted SHG: $\chi = \pm 45^\circ$ for circularly polarized light and 0° for linearly polarized light.

The Stokes parameters S_0, S_1, S_2 are a set of values describing the polarization state of light. They are contained in the 4-component Stokes vector

$$S = \begin{pmatrix} S_0 \\ S_1 \\ S_2 \\ S_3 \end{pmatrix} \quad (5.3-17)$$

The effect of the emitted SHG interacting with the individual polarizing elements is computed by using Muller matrices. The matrices M_{WGP}, M_{QWP} and M_R are Muller's matrices

for the fixed wire grid polarizer (WGP), quarter wave plate (QWP), and rotational matrix for the QWP, respectively [184], as defined in Chapter 4. The Stokes vector S_F for beam emerging from this optical configuration of Figure 5.9a with phase retardation ϕ and angle θ with respect to the laboratory x axis is

$$S_F = M_{WGP}M_R(-2\theta)M_{QWP}M_R(2\theta)S \quad (5.3-18)$$

$$= I(\theta, \phi) \times \begin{pmatrix} 1 \\ -1 \\ 0 \\ 0 \end{pmatrix} \quad (5.3-19)$$

$$I(\theta, \phi) = \frac{1}{2}[S_0 - S_1(\cos^2(2\theta) + \cos(\phi)\sin^2(2\theta)) - S_2\sin(4\theta)\sin^2(\frac{\phi}{2}) + S_3\sin(2\theta)\sin(\phi)] \quad (5.3-20)$$

$I(\theta, \phi)$ is the intensity of the beam recorded by the PMT. By fitting the measured signal to Equation 5.3-20 we can define the polarization state of the emitted SHG. Raw SHG polarimetry data taken with a linearly polarized incident fundamental beam whose polarization was parallel to the crystallographic [100] axis and corresponding fit to Equation 5.3-20 are shown in Figure 5.10a. The four-fold symmetry of data is consistent with a linear polarization state for emitted SHG since only the ED transitions are activated. Raw SHG polarimetry data taken using a linearly polarized to beam whose polarization axis was 45° relative to the [100] crystallographic axis and the corresponding fit to Equation 5.3-20 are shown in Figure 5.10b. In this configuration, both ED and MD transitions are activated, and the data indicate that the emitted SHG is elliptically polarized.

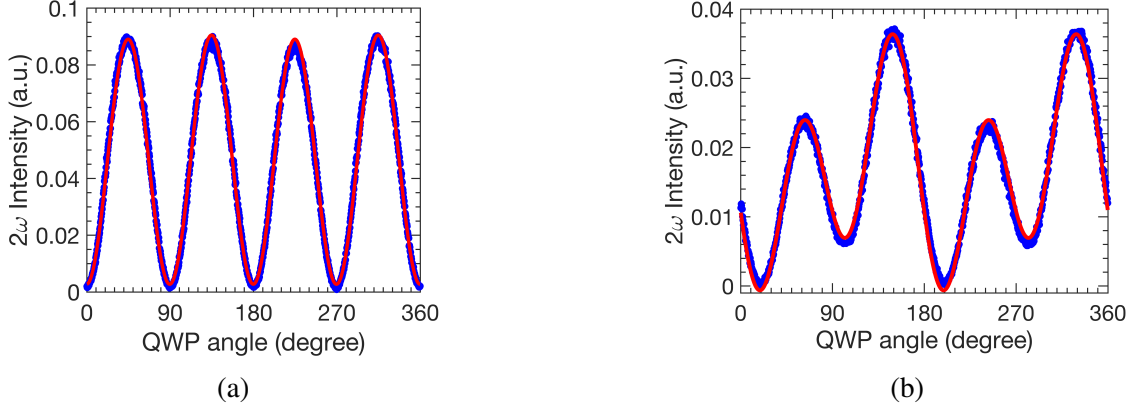


Figure 5.10: Polarimetry data of emitted SHG from $\text{Pr}_{0.8}\text{Nd}_{0.2}\text{AlSi}$ sample when the polarization axis of the incident beam is (a) parallel to and (b) 45° to the crystallographic [100] axis. Data are in blue and fits to Equation 5.3-20 are shown in red.

Quantitative analysis of the degree of ellipticity χ of this beam is given through Stokes parameters by

$$\chi = \frac{1}{2} \sin^{-1} \frac{S_3}{S_0} \quad (5.3-21)$$

The degree of ellipticity χ measures the shape of the polarization ellipse, which describes the path traced by the beam's electric field in one cycle of oscillation, as shown in Fig.5.9b. Its value ranges from -45° to 45° , where 0° represents a linear polarization state, -45° represents a left-circular polarization, and 45° represents a right-circular polarization state.

The plot of the ellipticity of the SHG signal as a function of the polarization angle of the linearly polarized incident beam is shown in Figure 5.11a. We observe that elliptical emission alternates between right and left elliptical polarized as a function of the incoming linear polarization relative to the crystallographic [100] axis with a maximum ellipticity angle of 22° for the mixed sample $\text{Pr}_{0.8}\text{Nd}_{0.2}\text{AlSi}$. We also note that the right elliptically polarized emission is slightly more circular than the left, which we currently ascribed to an experimental artifact. The average of maximum measured right and left elliptical polarized degree of ellipticity as a function of atomic number is shown in Figure 5.12. This plot shows that the angle of ellipticity increases with the increase in atomic number until the

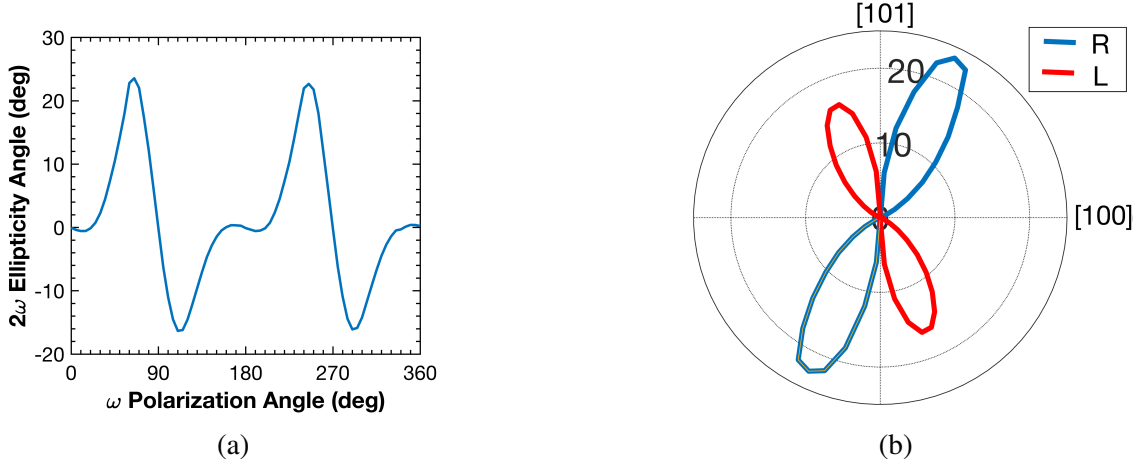


Figure 5.11: Cartesian and polar plot of the ellipticity angle of the emitted SHG due to linearly polarized incident light on $\text{Pr}_{0.8}\text{Nd}_{0.2}\text{AlSi}$. (a) Cartesian plot as a function of the incident linear polarization angle with respect to the laboratory x-axis. (b) polar plot of the data in (a) showing the crystallographic axes.

Fano asymmetric parameter q changes sign with $\text{Pr}_{0.8}\text{Nd}_{0.2}\text{AlSi}$ at which point it begins to decrease again. This is reminiscent of electromagnetically induced transparency, where the degree of transparency is inversely proportional to q .

5.4 Conclusion

We have measured strong MD transitions in the LnAlSi family of Weyl semimetals at paramagnetic phase that reveal the presence of a Fano resonance due to the quantum interference of Ln f -orbitals with d and p -orbitals. These MD transitions are due to the trivalent rare earth ion in the material and were observed to drive nonlinear electromagnetically induced chirality characterized by elliptically polarized emitted SHG from linearly polarized, normally incident fundamental.

Significantly, the presence of strong MD transitions in band solid allows for application platforms to be developed over a much broader energy bandwidth than is allowed for doped, transparent media. Further, the observation of MD transitions in a metallic system is of note because it indicates the robustness of atomic selection rules in the presence of many other bands; this further supports the band structure calculations that indicate poor mixing of f -

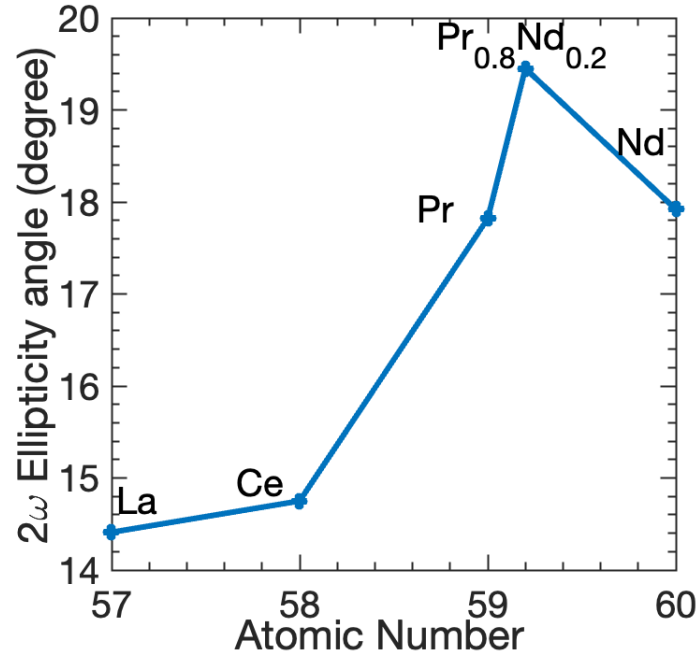


Figure 5.12: Dependence of the degree of ellipticity with Ln atomic number in LnAlSi. The degree of ellipticity increases with the increase in atomic number except for Pr_{0.8}Nd_{0.2}AlSi to NdAlSi transition. This trend is reminiscent of the strength of electromagnetically induced transparency as a function of asymmetry parameter q .

block electrons with those from other orbitals since such mixing would significantly dilute these selection rules or suppress them altogether. Further work on these materials will focus on examining their low temperature behavior in the vicinity of the MD resonance. The addition of magnetic ordering will activate the $M_i = \chi_{ijk}^{mee} E_j E_k$ term (and possibly the $M_i = \chi_{ijk}^{mem} E_j H_k$ term) bringing the electromagnetic response falling in line with the chiral second order constitutive relations of Equation 5.1-5 and 5.1-6. Work toward this objective is currently underway.

CHAPTER 6

TIME RESOLVED CIRCULAR DICHROISM AND NON-LINEAR OPTICAL HARMONIC GENERATION STUDY OF THE CHARGE DENSITY WAVE PHASE OF THE TRANSITION METAL DICHALCOGENIDE (1T – TiSe₂)

This chapter describes time-resolved circular dichroism (tr-CD), pump-probe (pp-), static second harmonic generation (SHG), and third harmonic generation (THG) spectroscopy measurements on the transition metal dichalcogenide (TMD) 1T – TiSe₂, a material introduced in Chapter 3. Our study is motivated by the uncertainty surrounding the symmetry of the low-temperature phase of 1T – TiSe₂, which remains poorly understood. First, tr-CD measurements on 1T – TiSe₂ were conducted with 800 nm (1.55 eV) pump and 620 nm (2.00 eV) and 680 nm (1.82 eV) probe wavelengths. Our data show evidence of a photoinduced chiral CDW in 1T – TiSe₂ as predicted by density functional theory calculations which persist for ~ 1 -3 ps. We also used SHG and THG spectroscopy to study 1T – TiSe₂ below its CDW phase transition temperature at $T_{CDW} \simeq 200$ K. In contrast with our tr-CD data, lack of pp-SHG and SHG signals below and above the transition temperature indicated that the low-temperature symmetry-breaking phase is, in fact, achiral. Further measurements using rotational anisotropy THG (RA-THG) revealed that 1T – TiSe₂ undergoes a non-trivial phase transition at $T_* \simeq 180$ K within the charge density phase that comprises at least two separate domain types that randomly rearrange upon thermal cycling both for the CDW and for the secondary phase transition at $T_* \simeq 180$ K. Taken together,

our data may appear contradictory in the sense that support the onset of orbital ordering at 180 K without the emergence of an electronically chiral state.

6.1 Background

After the discovery of graphene in 2004, there has been an explosion of research in the field of two-dimensional (2D) materials due to their remarkable properties, including high conductivity [223], mechanical strength [224], and flexibility [225]. The TMDCs, which may be considered 2D due to weak van der Waals bonding between covalently bonded layers, also exhibit giant spin-orbital coupling [226] in those species from periods, as well as a direct bandgap, making them promising candidates for next-generation spintronics and optoelectronic devices [227]. TMDCs crystallize in centrosymmetric trigonal prismatic (2H) and octahedral (1T) structural phases, each of which exhibits various electronic symmetry breaking phases, including charge density wave (CDW) and superconducting order [228]. Investigating the nature of their low-temperature electronically ordered states, as well as their photo-excited quasiparticles are crucial for an understanding of these systems that could lead to their widespread application.

An example of such a TMDC is 1T–TiSe₂ which hosts a CDW instability in the bulk form below $T_{CDW} \simeq 200$ K with ordering vectors $\mathbf{q}_1 = \frac{1}{2}(\mathbf{a}^* + \mathbf{c}^*)$, $\mathbf{q}_2 = \frac{1}{2}(\mathbf{b}^* + \mathbf{c}^*)$, and $\mathbf{q}_3 = \frac{1}{2}(\mathbf{b}^* + \mathbf{c}^*)$, where \mathbf{a}^* , \mathbf{b}^* and \mathbf{c}^* are reciprocal lattice vectors [146]. These CDW ordering vectors connect the center of the Brillouin zone Γ to the three inequivalent L points in the hexagonal Brillouin zone (BZ) [146], as shown in Figure 6.1. The origin of this CDW is still unclear. The Fermi surfaces at both the Γ and L points are 3D and spherical in shape, which is not favorable to Fermi surface nesting as described by the Peierls transition [229]. This necessitates different explanations to account for CDW formation. Some studies observed that transverse optical phonon along the M-L direction softens, suggesting that the CDW derives from electron-phonon coupling [134, 230]. However, others argue that the CDW is

driven by an excitonic pairing mechanism due to the formation of a bound state of holes at Γ and electrons at M/L in first BZ [154].

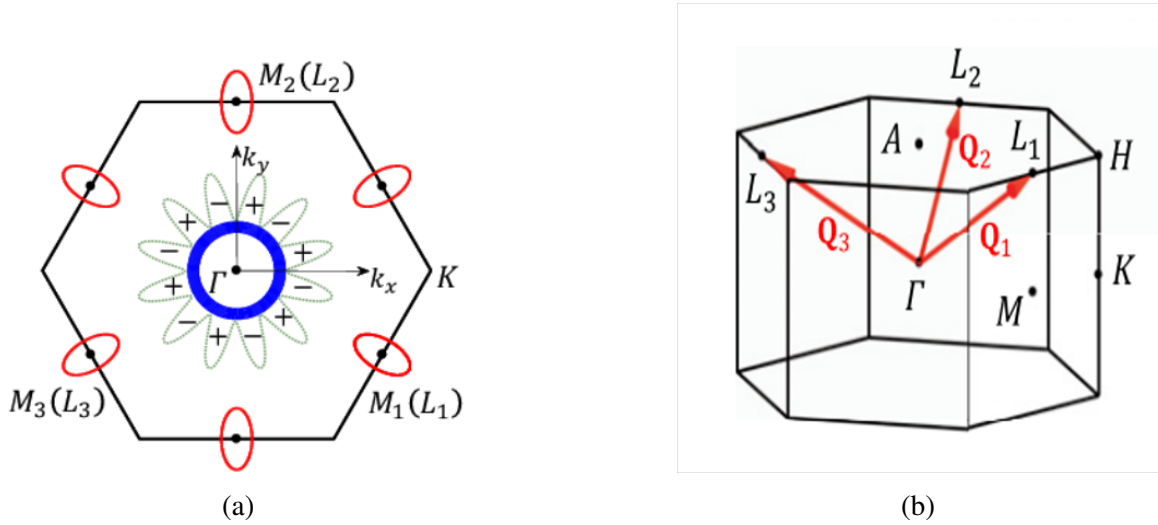


Figure 6.1: Fermi surface and CDW vectors in 1T–TiSe₂ (a) Fermi surface (b) first BZ with CDW ordering vectors. Figure taken from Ref. [146]

In addition to the driving mechanism, the symmetry of the CDW phase is also not fully understood, as there is vigorous debate concerning whether or not the CDW becomes chiral below the phase transition temperature. Scanning tunneling microscopy (STM) and time domain optical polarimetry studies reported a chiral CDW phase due to an electronic phase shift of $\frac{2\pi}{3}$ between CDW layers along the crystalline axis c [34]. Chiral CDWs with gyrotropic order were also observed via measuring a nonzero circular photogalvanic effect after field cooling under illumination by circularly polarized light [163]. Further, an X-ray diffraction study indicates an emergent chiral atomic configuration occurring below the CDW transition temperature [164]. However, a study combining STM with a low density of buried defects observed uniform CDW modulation, challenging [34] the notion that the CDW is chiral in nature.

In an attempt to reconcile these two different views, some researchers have argued that the CDW may be driven from achiral to chiral by an external stimulus such as via photoexcitation. In this scenario, heating of the electronic population results in motion of the Ti

atoms. The direction and displacement of the Ti atoms in the CDW phase either generate a chiral [164] or achiral phase [31]. These configurations are shown in Figure 6.2, where the two possible structural distortions that can occur from the high-temperature $P\bar{3}m1$ structure are depicted. The reconstruction due to the soft mode at the L point or the M point is thus predicted to transition the high-temperature structure either to the centrosymmetric $P\bar{3}c1$ or the noncentrosymmetric $P321$ CDW structure where the $P\bar{3}c1$ structural energy is slightly lower than that of $P321$ [31]. Upon photoexcitation past a critical fluence, the non-centrosymmetric structure is predicted to become nearly degenerate in energy with the centrosymmetric phase, leading to a structural transition into the acentric, chiral phase that exhibits circular dichroism (CD) [31]. However, this assertion remains to be proven.

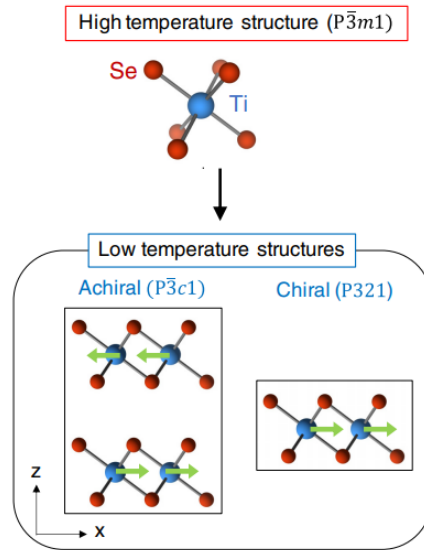


Figure 6.2: Diagram depicting the transformation of the achiral centrosymmetric high-temperature $P\bar{3}m1$ structure into either the achiral centrosymmetric $P\bar{3}c1$ CDW structure or the chiral noncentrosymmetric $P321$ CDW at low temperature. The green arrows indicate the direction in which the Ti atoms are displaced in the CDW phase. Figure taken from Ref. [31].

In order to study the effects of electronic temperature on the structural symmetry of the CDW phase of 1T-TiSe₂, we have used ultrafast time-resolved spectroscopy and non-linear optical techniques [231–233]. In particular, since chiral media absorb left and right circularly polarized light at different magnitudes, these time-resolved pump-probe tech-

niques can be combined with circular dichroism to search for chirality in the CDW phase in response to photoexcitation. In this technique, an intense pump beam excites the sample, while a low-power probe beam interacts with the excited sample, and the change in absorbance is measured for both left and right circularly polarized probe beams. Equivalently, even order nonlinear harmonic generation may be used to probe for chirality since, in the electric dipole approximation, these responses are only generated in non-centrosymmetric structures and electronically ordered phases, as well as at surfaces and interfaces because these are loci of inversion symmetry breaking.

Below, we describe experiments using time-resolved and nonlinear optical methods to examine if the low-temperature centrosymmetric $1T\text{-TiSe}_2$ structure can be driven into a noncentrosymmetric structure by excitation past critical electronic temperature [31]. Furthermore, we also employed pump-probe SHG and rotational anisotropy SHG and THG to study the structural and electronic symmetries of $1T\text{-TiSe}_2$ as a function of temperature. Our results are conflicting. While we do observe a tr-CD signal indicative of a structural transition from an achiral to a chiral structure, these observations are at odds with the null response seen in pump-probe SHG data that show no evidence of a laser-driven noncentrosymmetric phase compatible with structural chirality. Similarly, static SHG measurements yielded no measurable signal, while static THG measurements clearly showed evidence of two transitions, one at $T_{\text{CDW}} \approx 200$ K and another at $T^* \simeq 180$ K. While a single explanation that brings all observations into mutual agreement is currently lacking. We argue that the data are consistent with an orbital ordering transition into a cluster multipole that couples to third order optical probes.

6.2 Time-Resolved Pump-Probe Circular Dichroism

6.2.1 Experimental Setup

A brief overview of time-resolved pump-probe spectroscopy has already been given in Chapter 4. In this technique, a $\sim 10 - 100$ fs laser pulse (pump) is incident upon the sample, photoexciting it at time $t = 0$. Another relatively weak laser pulse (probe) is reflected off the sample to monitor the change in optical properties due to the pump beam as a function of delay time t . This technique can be used to measure time-resolved laser-driven changes to photo-optical properties such as, e.g., reflectivity [234], transmissivity [235], SHG [172], among a multitude of other responses.

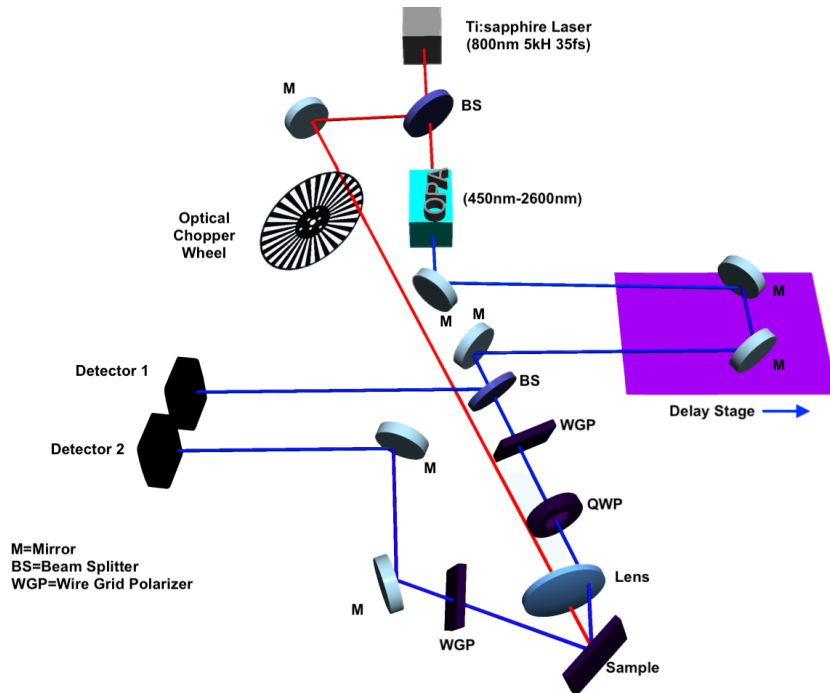


Figure 6.3: Experimental Setup for time-resolved pump-probe measurement. Optics are M - mirror, BS - beam splitter, WGP - Wire grid polarizer, and QWP - quarter waveplate.

A schematic diagram of the setup is shown in Figure 6.3. The output of a 800 nm wavelength Ti:sapphire laser system with a 35 fs pulse duration and a 5 kHz repetition rate was split into two beams using a beam splitter. One beam was used as a pump that was mechanically chopped using an optical chopper wheel at half the laser repetition rate so

that changes in optical properties due to photoexcitation could be measured with sensitivity detection techniques. Another beam was used to seed an optical parametric amplifier (OPA) to produce continuously tunable output over the 450 - 2600 nm wavelength range. OPA output at 620 nm and 680 nm spacing were used as two separate probe wavelengths to study the resulting time-resolved phenomena. The output from the OPA was mechanically delayed by a precision delay stage (SmarAct, SLLV42Ic-339) to build up the time-domain trace. This beam was further split into separate arms, one of which was directly sent to a detector as a reference while the other was used as a probe to record the excitation that was initiated by the pump. The optical reflectivity data were acquired by using a balanced detection scheme [175] in which the reference beam was subtracted from the signal beam to remove the pulse-to-pulse energy variation in the laser, as described in Chapter 4.

In order to measure the CD response, the detection arm was passed through a wire grid polarizer (WGP) (Thorlabs, WP12L-UB) and emerged horizontally polarized, after which an achromatic quarter-wave plate (QWP) (Thorlabs, AQWP05M-600) made the linearly polarized probe light either right or left circularly polarized. The circularly polarized beam was focused onto the sample using a lens, and the reflected beam then passed through another WGP whose transmission axis was aligned perpendicular to the first WGP before QWP. Data were taken for the left-handed circularly polarized light and right-handed circularly polarized light and then subtracted from one another to recover the CD signal.

6.2.2 Results of tr-CD Experiments

An example of tr-CD, as measured from the difference in reflectivity between left circularly polarized (CPL) and right circularly polarized (CPR) probe beams, is shown in Figure 6.4 at 50.3 K. There is a small (order $\sim 10^{-3}$) degree of CD typical of illustrating the presence of circular dichroism (CD) that persists of ~ 3 ps.

tr-CD data taken with 620 nm and 680 nm probe beams and a 800 nm pump beam (fluence 0.11 mJ/cm²) are shown in Figures 6.5a and 6.5b. A non-zero CD response is ob-

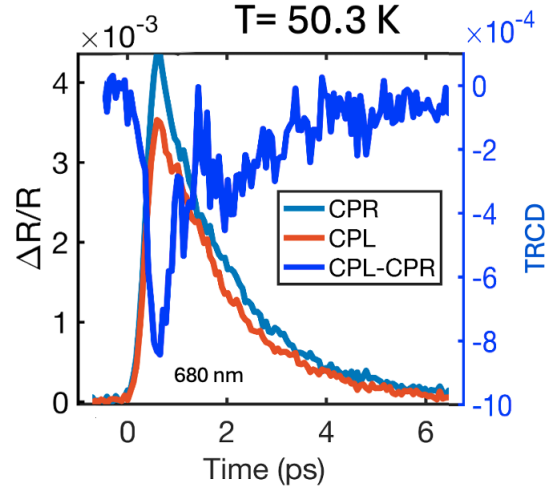


Figure 6.4: Time-resolved change in reflectivity with 680 nm CPL and CPL probe beam with 800 nm pump beam along with TRCD data obtained from subtraction between CPL and CPR at 50.3 K.

served only below $T_{\text{CDW}} = 200$ K, disappearing above the T_{CDW} . This observation implies that the increase in electronic temperature, produced by the pump has appeared to generate a transient non-centrosymmetric structure with different signs for either wavelength, as described in Ref. [31]. Our data thus suggest a photo-induced achiral to chiral transition in the CDW phase of 1T-TiSe₂.

6.3 Rotational Anisotropy Nonlinear Harmonic Generation (RA-NHG)

Nonlinear harmonic generation (NHG) is a widely applied technique for studying exotic symmetry breaking phases, here we used it to investigate 1T-TiSe₂. An incident beam of frequency ω interacts with a nonlinear medium and emits photons of higher harmonics $n\omega$, where n is an integer. The nonlinear response is determined by the material's nonlinear optical susceptibility tensor at order n which is of rank $n + 1$. These techniques have been successfully applied to study lattice symmetry [236] and electronic symmetry breaking [237] that may be hidden to more conventional scattering probes. By measuring all the components of the second order nonlinear susceptibility tensor through various combinations of incident and emitted polarizations, the lattice and electronic symmetries can

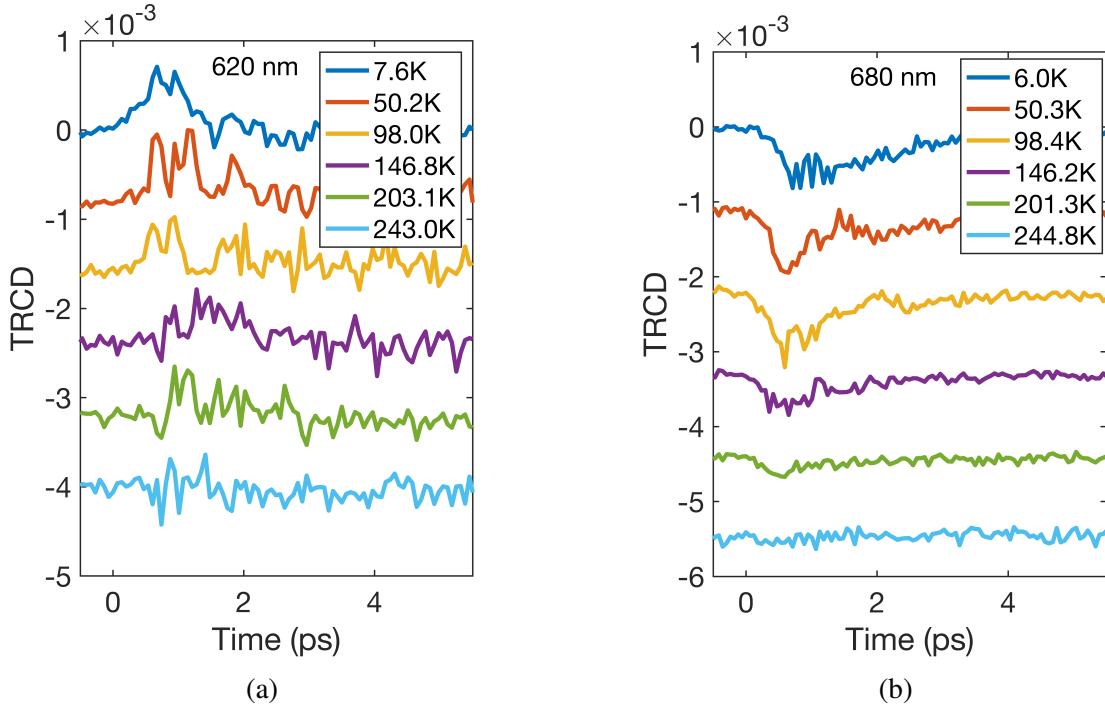


Figure 6.5: (a) Transient circular dichroism (Tr-CD) measured on the picosecond timescale as a function of temperature using (a) 620 nm and (b) 680 nm probe wavelengths.

be identified and resolved as a function of temperature or as a function of time following photoexcitation [238].

The static scattering plane rotational anisotropy apparatus used here is depicted in Figure 6.6. 1830 nm light from the idler output of the OPA was used to study the RA-NHG response. The OPA beam's output was purified using a wire grid polarizer (WGP) (Thorlabs, WP12L-UB). In order to generate a circularly polarized probe field, the beam was passed through a quarter wave plate (QWP) (Thorlabs, AQWP05M-1600). Subsequently, the beam passed through a rotating polarizer (RP) spinning at 5 Hz to achieve a continuously varying polarization angle. In order to suppress wavelengths spuriously generated by the optics, long pass filters (Thorlabs, EFLH 1300, and EFLH 1500) were used to further purify the beam. A spherical mirror (SM) (Thorlabs, CM254-500-P01) then focused the beam onto the sample. The reflected beam from the sample was directed towards a D-shaped mirror (DM) and passed through an analyzer. The analyzer could be set to re-

main stationary in either a vertical or horizontal orientation or to rotate in synchrony with the incoming polarization with its polarization axis either parallel or perpendicular to the polarization state of the incoming beam, as detailed below. After passing through the analyzer, the beam was directed through a shortpass filter (SPF) (SHG: Thorlabs, FESH1000 and Semrock, FF01-1326/SP-25, THG : Thorlabs, FB610-10, and FESH0650) to eliminate the fundamental wavelength while preserving the nonlinear response from the sample. Finally, the beam was collected by a photomultiplier tube (Hamamatsu, R12829). The intensity of the detected beam was recorded using a data acquisition card-based fast-sampling technique as described in Ref. [185].

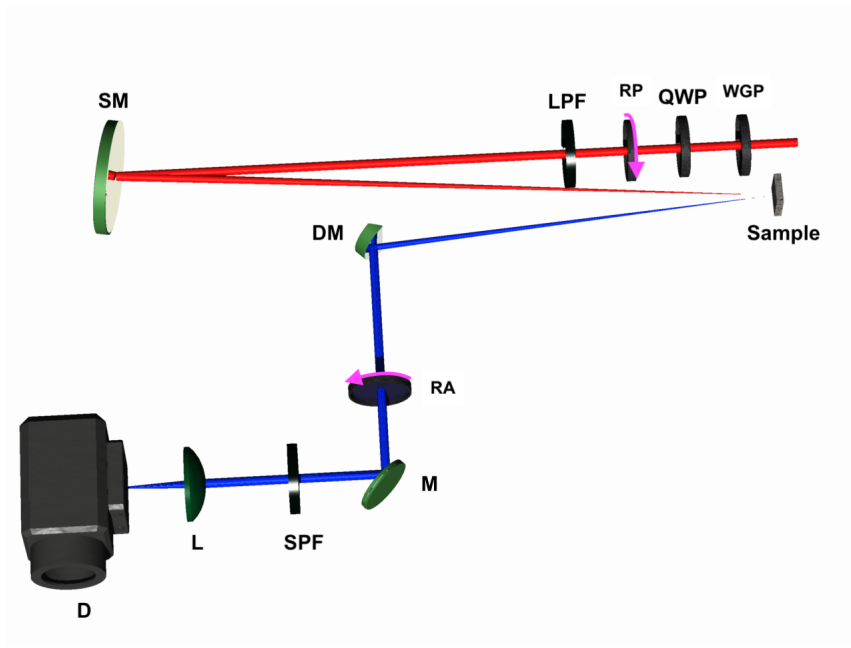


Figure 6.6: Static scattering plane RA-SHG experimental setup. Optics are WGP - wire grid polarizer, QWP - quarter waveplate, RP - rotating polarizer, LPF - long pass filter, SM - spherical mirror, DM - D-shape mirror, RA - analyzer, M - mirror, SPF - shortpass filter, L - lens, D - detector.

In order to study structural change, we also performed pump-probe SHG using with 1300 nm pump and 800 nm probe in the experimental setup shown in Figure 6.3 albeit without the use of balanced detection. To measure any potential time-resolved second

harmonic generation (SHG) signals, a bandpass filter (Thorlabs, BP400-40) was used to pass the SHG signal, if any, and finally collected by a photomultiplier tube.

6.3.1 Static Scattering Plane Rotational Anisotropy Second and Third Harmonic Generation

In order to study RA-SHG on 1T–TiSe₂ at low temperatures, we used wavelengths in the 700 - 1800 nm range using different polarization configurations of incoming and outgoing SHG beams: 1) incoming polarization rotating with outgoing SHG polarization static and horizontally polarized ($I_H^{2\omega}$) 2) incoming polarization rotating with outgoing SHG polarization static and vertically polarized ($I_V^{2\omega}$) 3) incoming and SHG polarization co-rotating and parallel ($I_{\parallel}^{2\omega}$) 4) incoming and SHG polarization co-rotating and perpendicular ($I_{\perp}^{2\omega}$). Data were acquired both above and below the CDW transition temperature T_{CDW} . No SHG was observed at any temperature, as shown in Figure 6.7. This suggests that the low-temperature structure of 1T–TiSe₂ does not belong to a non-centrosymmetric space group and therefore is unlikely to be chiral. More importantly, we obtained the same result in our pump-probe SHG measurements. Here, too, there was an absence of an SHG response from the sample.

Although pp-SHG and SHG experiments yielded no measurable response, we may still take advantage the sensitivity of THG experiments to subtle electronic and lattice ordering using THG. THG signal is allowed in both centrosymmetric and non-centrosymmetric systems. In THG, the induced radiating polarization $P_i(3\omega)$ is given by

$$P_i(3\omega) = \chi_{ijkl}^{(3)} E_j(\omega) E_k(\omega) E_l(\omega) \quad (6.3-1)$$

where $\chi_{ijkl}^{(3)}$ is the fourth rank THG nonlinear susceptibility tensor and is

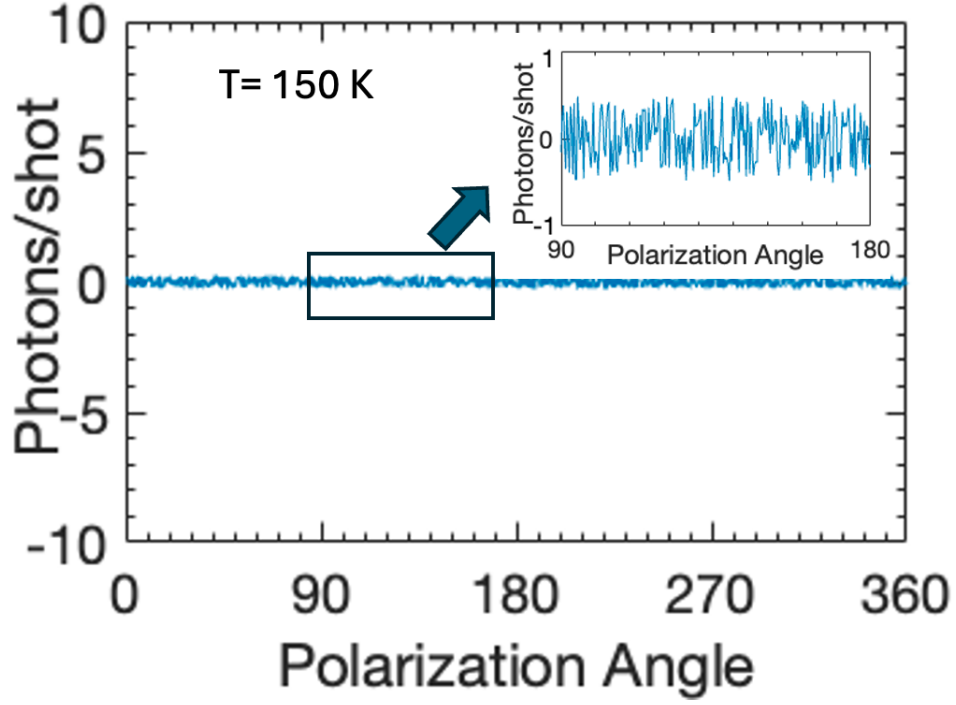


Figure 6.7: SHG Experimental data at 150 K showing no response to within less than one photon/shot on average. This suggests that chiral symmetry breaking does not occur.

$$\chi_{ijkl}^{3\omega} = \begin{pmatrix} \begin{pmatrix} \chi_{xxxx} & 0 & 0 \\ 0 & \frac{\chi_{xxxx}}{3} & \chi_{xxyz} \\ 0 & \chi_{xxyz} & \chi_{xxzz} \end{pmatrix} & \begin{pmatrix} 0 & \frac{\chi_{xxxx}}{3} & \chi_{xxyz} \\ \frac{\chi_{xxxx}}{3} & 0 & 0 \\ \chi_{xxyz} & 0 & 0 \end{pmatrix} & \begin{pmatrix} 0 & \chi_{xxyz} & \chi_{xxzz} \\ \chi_{xxyz} & 0 & 0 \\ \chi_{xxzz} & 0 & 0 \end{pmatrix} \\ \begin{pmatrix} 0 & \frac{\chi_{xxxx}}{3} & \chi_{xxyz} \\ \frac{\chi_{xxxx}}{3} & 0 & 0 \\ \chi_{xxyz} & 0 & 0 \end{pmatrix} & \begin{pmatrix} \frac{\chi_{xxxx}}{3} & 0 & 0 \\ 0 & \chi_{xxxx} & -\chi_{xxyz} \\ 0 & -\chi_{xxyz} & \chi_{xxzz} \end{pmatrix} & \begin{pmatrix} \chi_{xxyz} & 0 & 0 \\ 0 & -\chi_{xxyz} & \chi_{xxzz} \\ 0 & \chi_{xxzz} & 0 \end{pmatrix} \\ \begin{pmatrix} 0 & \chi_{zxy} & \chi_{zxxz} \\ \chi_{zxy} & 0 & 0 \\ \chi_{zxxz} & 0 & 0 \end{pmatrix} & \begin{pmatrix} \chi_{zxy} & 0 & 0 \\ 0 & -\chi_{zxy} & \chi_{zxxz} \\ 0 & \chi_{zxxz} & 0 \end{pmatrix} & \begin{pmatrix} \chi_{zxxz} & 0 & 0 \\ 0 & \chi_{zxxz} & 0 \\ 0 & 0 & \chi_{zzzz} \end{pmatrix} \end{pmatrix}$$

Through trial and error, we determined that 1830 nm was the best wavelength for studying the transition. We used a 610 nm bandpass optical filter (Thorlabs, FBH600-10) before the PMT to transmit the THG from the sample and block the fundamental.

To verify our data fit the theoretical expectation for the D_{3d} point group, we calculated the mathematical expressions for the THG signal in the same polarization configurations and rotation as described above for SHG. The relevant expressions are

$$I_{\parallel}^{3\omega} = \frac{1}{1024} \cos^2(\phi) ((-9\sqrt{2}\chi_{xxyz} + 20\chi_{xxzz} - 3\sqrt{2}\chi_{zxy} + 10\chi_{zxxz} + 6\chi_{zzzz}) \cos(\phi) + (21\sqrt{2}\chi_{xxyz} - 4\chi_{xxzz} + 7\sqrt{2}\chi_{zxy} - 2\chi_{zxxz} + 2\chi_{zzzz}) \cos(3\phi) + 2(\chi_{xxyz} + \chi_{zxy})) (3 \sin(\phi) - 5 \sin(3\phi))^2 \quad (6.3-2)$$

$$I_{\perp}^{3\omega} = (-6(4\sqrt{2}\chi_{xxxx} + \chi_{xxyz} + 4\sqrt{2}\chi_{xxzz} - 3\chi_{zxy}) + 8(\sqrt{2}\chi_{xxxx} + 3\chi_{xxyz} - 3\sqrt{2}\chi_{xxzz} - 6\chi_{zxy}) \cos(2\phi) + 30(\chi_{xxyz} + \chi_{zxy}) \cos(4\phi) + 6(9\sqrt{2}\chi_{xxyz} - 4\chi_{xxzz} - 5\sqrt{2}\chi_{zxy} + 6\chi_{zxxz} + 2\chi_{zzzz}) \sin(2\phi) + 3(21\sqrt{2}\chi_{xxyz} - 4\chi_{xxzz} + 7\sqrt{2}\chi_{zxy} - 2\chi_{zxxz} + 2\chi_{zzzz}) \sin(4\phi))^2 \quad (6.3-3)$$

$$I_V^{3\omega} = \frac{1}{576} \cos^2(\phi) ((\sqrt{2}\chi_{xxxx} + 9\chi_{xxyz} - 3\sqrt{2}\chi_{xxzz}) \cos(2\phi) - 3(\sqrt{2}\chi_{xxxx} + \chi_{xxyz} + \sqrt{2}\chi_{xxzz} + (-6\sqrt{2}\chi_{xxyz} + 4\chi_{xxzz}) \sin(2\phi)))^2 \quad (6.3-4)$$

$$I_H^{3\omega} = \frac{1}{4680} (3(3\chi_{xxyz} + 6\sqrt{2}\chi_{xxxx} - 3\chi_{zxy} + \sqrt{2}(5\chi_{zxxz} + 3\chi_{zzzz})) \cos(\phi) + 3(9\chi_{xxyz} + 2\sqrt{2}\chi_{xxzz} + 7\chi_{zxy} + \sqrt{2}(\chi_{zxxz} + \chi_{zzzz})) \cos(3\phi) - 2(7\chi_{xxxx} + 12(\sqrt{2}\chi_{xxyz} + \chi_{xxzz}) \cos^2(\phi) + 3\sqrt{2}\chi_{zxy}(1 + 5 \cos(2\phi)) \sin(\phi) + 2\chi_{xxxx} \sin^2(3\phi))) \quad (6.3-5)$$

RA-THG data and global fits to Equations 6.3-2 to 6.3-5 are shown in Figure 6.8. The good agreement between the model and RA-THG data is consistent with 1T–TiSe₂ belonging to the D_{3d} point group, which is, incidentally, achiral.

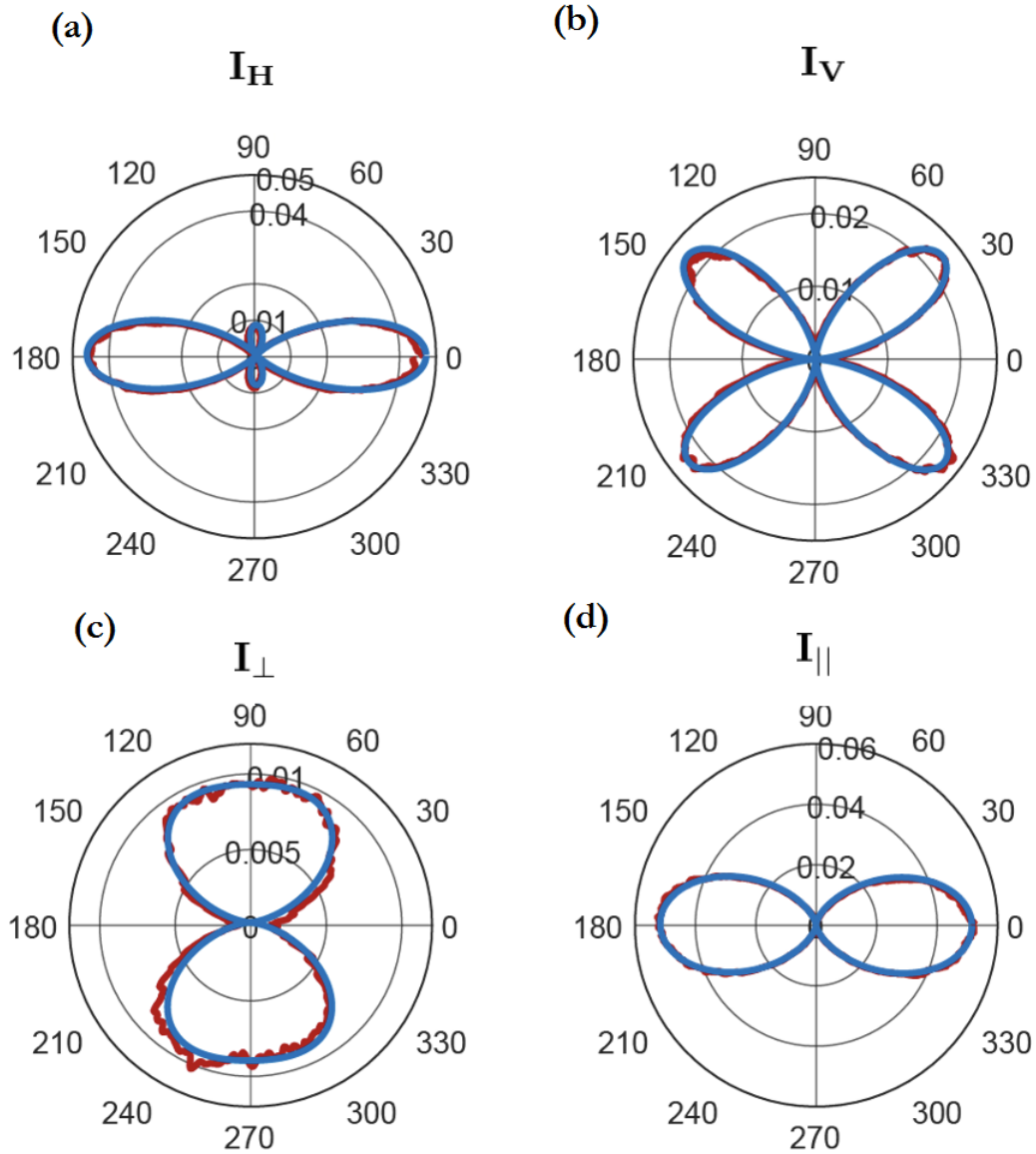


Figure 6.8: THG data from 1T–TiSe₂ at 150 K using 1830 nm incident wavelength are shown in red for the four experimental configurations mentioned above. Fits to Equations 6.3-2 - 6.3-5 in blue using global fit parameters closely match the data.

We next conducted RA-THG measurements in a static scattering plane geometry as a function of temperature and fit all the data to the expression of Equations 6.3-2 and 6.3-5

using global fit parameters. The resulting tensor elements obtained from the fits are shown in Figure 6.9.

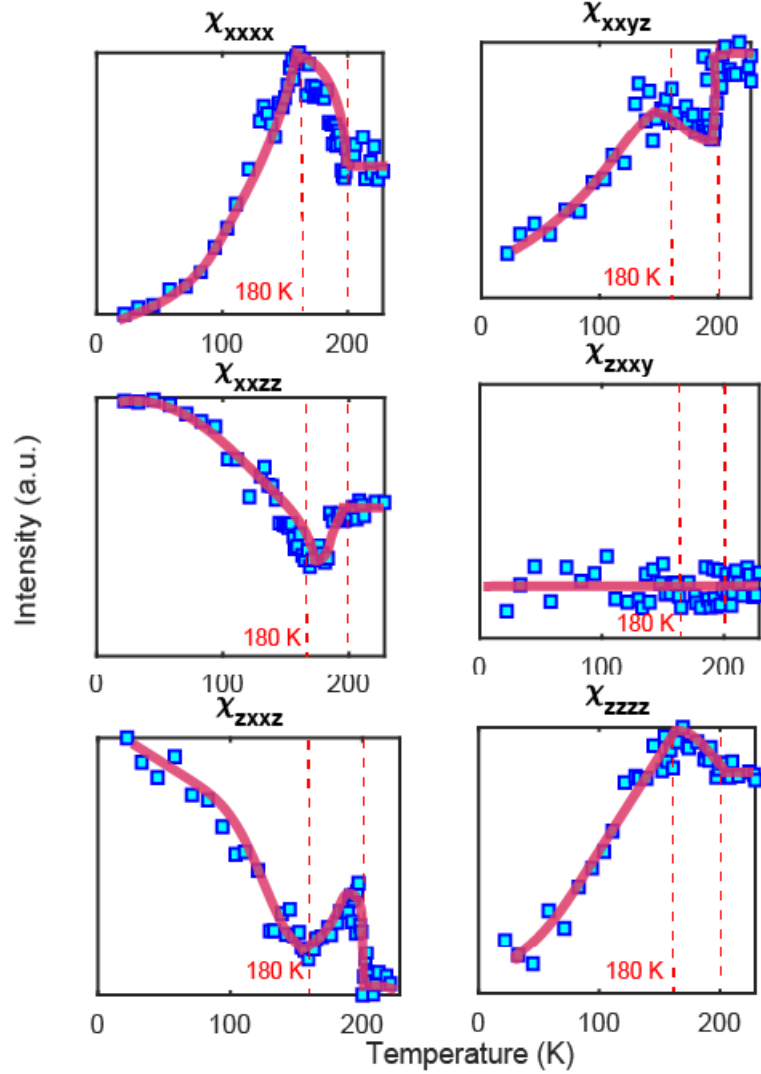


Figure 6.9: THG tensor elements $\chi_{ijk}^{(3)}$ as a function of temperature. The blue squares are data and the red lines are guides for the eye. We note that the transition at $T_{CDW} \approx 200$ K and $T_* \approx 180$ K clearly evolve independently of one another.

The data clearly show two distinct second order transitions, $T_{CDW} \approx 200$ K and at $T_* \approx 180$ K. The transition at 200 K may be unambiguously assigned to the formation of CDW. More importantly, a new transition that is barely perceptible in X-ray scattering [164] was observed at 180 K. In order to verify that this transition was independent of the CDW transition, we performed temperature cycling experiments as shown for the χ_{xxxx} tensor element

in Figure 6.10. Significantly, the data did not follow a consistent trend with each cycle. The THG signal strength at both transitions was observed to either increase or decrease independently, suggesting the presence of domains of each kind of ordered phase at low temperatures that were rearranged following each thermal cycle. Importantly, we emphasize that the trends observed below T_{CDW} and T_* were independent from one another for all thermal cycles.

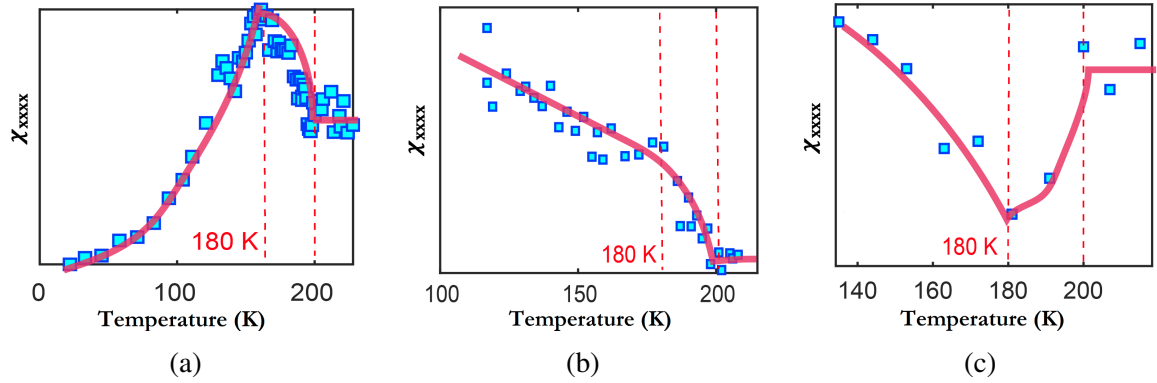


Figure 6.10: RA-THG susceptibility tensor element (χ_{xxxx}) as a function of temperature from three different thermal cycles, (a) first cycle (b) second cycle (c) third cycle. We note that both transitions either increased or decreased independently from one another at the two transition temperatures $T_{CDW} \simeq 200$ K and $T_* \simeq 180$ K.

The phase transitions in 1T-TiSe₂, both at T_{CDW} and at T_* were analyzed using the critical exponential function

$$I \propto \left(1 - \frac{T}{T_c}\right)^a \quad (6.3-6)$$

where T_c is the relevant transition temperature and a is a critical exponential parameter.

In so doing, we are making the assumption that the radiating polarization scales linearly proportionally to the order parameter and thus linearly proportionally with $\chi_{ijkl}^{(3)} E_j E_k E_l$.

The best fit results, shown in Figure 6.11b, reveal that the CDW phase transition at $\simeq 201$ K has a critical exponent of $a = 0.53$. Elastic X-ray diffraction measurements yielded a critical exponential of 0.52, tracking the integrated intensities of superlattice reflection from the $[0, 1/2, 19/2]$ [239]. In addition, a second phase transition was observed at around 180 K,

of critical exponent of 0.52 as shown in Figure 6.11a. However, X-ray the diffraction intensity data from the $[0, 1/2, 8]$ superlattice peak associated with the lower temperature transition are linear as a function of temperature. Furthermore, the signal was quite weak [239]. In a separate study, the integrated intensity of reflection from the $[3/2, 3/2, 1/2]$ and $[5/2, 0, 0]$ superlattice peaks in elastic X-ray diffraction experiments also observed two separate phase transition temperatures, which were at 192 K and 183 K, respectively. The upper temperature was ascribed to the CDW transition, as indicated by the superlattice peaks. The X-ray integrated intensity of the superlattice reflection at a lower temperature is ≈ 50 times weaker than the primary CDW peak [164]. In our measurement, both intensities are approximately equally strong of a change in magnitude per unit temperature change.

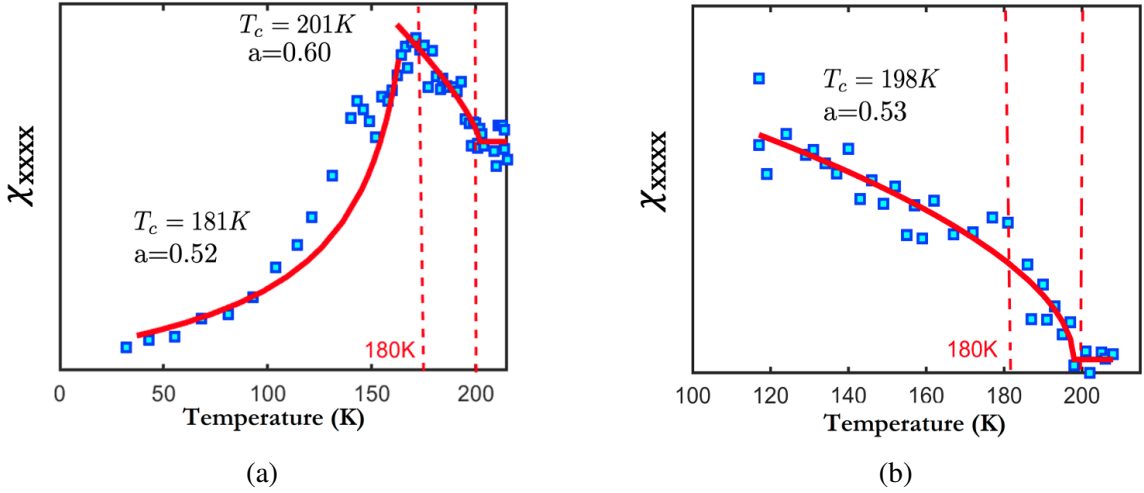


Figure 6.11: RA-THG susceptibility tensor element $\chi_{xxxx}^{(3)}$ fitted by the critical exponent Equation 6.3-6 for (a) the first (b) the second temperature cycle.

We now argue that the signature at $T_* \approx 180$ K is the result of the orbital ordering transition observed in Ref. [156] by resonant x-ray scattering. There has been no observation of time-reversal symmetry breaking in 1T-TiSe₂, indicating no magnetic order. Furthermore, the CDW itself does not change in morphology as would be visible in STM measurements. Since there is no measurable lattice deformation at $T_* \simeq 180$ K as would appear in X-ray scattering, by a process of exclusion, we are left with orbital ordering. The configuration of the orbital ordering is shown in Figure 6.12, which is oriented along the three different

CDW ordering vectors $\vec{\epsilon}_i$ and is driven by charge transfer between the Se- p and Ti- d orbitals as shown in the figure. Specifically, the Ti- d orbitals are those that belong to the t_{2g} manifold in the octahedral crystal field of the Se atoms, i.e., d_{xy} , d_{xy} and d_{xz} . In order to minimize their mutual Coulomb repulsion, the different CDW components designated by different ϵ_i slide relative to one another to cause charge transfer from Se- p to Ti- d , thus creating a charge imbalance within the members of the t_{2g} manifold i.e., orbital order. While this might also induce aggregate inversion symmetry breaking, the effect might be too small even for STM or X-ray diffraction to measure [240] of significant note is that the charge configuration shown in Figure 6.12 is a complex object of coordinated multipolar charge distributions known as a cluster multipole [241]. The combination of hybridized p - and d - orbital (hybrid multipole) in the inter-lattice-site arrangement can give rise to a complex multipole with an active rank-3 component [241], which can be measured by THG. That NHG is sensitive to complex multipolar/orbital ordering is to be expected based on previous work on Sr_2IrO_4 [236] where SHG was used to uncover a magnetotropical multipole produced by orbital ordering. However, a final confirmation of this observation may require rotating scattering plane THG with the same experimental geometry used in Ref. [236] for SHG.

The set of all observations given here appears to point a contradictory picture of the symmetry of the CDW transition in 1T-TiSe₂. The observation of finite tr-CD would seem to indicate that there is a photoinduced phase transition into a structurally chiral phase that is predominantly of a single helicity; if the photoexcited region were racemically twinned (i.e., equal populations of right and left helical domains), the overall response would be null as the probe would integrate over equal regions of right and left racemates, as it is understood that opposite handedness results in opposite signed CD responses of equal magnitude. Instead, a finite signal of the same polarity was observed with each cooling cycle, an example of which is given by Figure 6.5.

It follows that we should also expect to see a finite pp-SHG response due to the prevalence of one racemate over the other, as structural chirality trivially indicates inversion symmetry breaking, and SHG is considered a far more sensitive probe of chirality than a linear CD. In a chiral sample, opposite helicities yield SHG of opposite phase such that the racemic twinning ruled out by tr-CD should also give a null result with the restoration of a mirror symmetry. A null result in pp-SHG was, however, observed. We also obtained a null result of static SHG, indicating that no photoinduced phase transition occurs within the laser's pulse duration.

Of note is that the tr-CD signals occurred at $T_{CDW} \approx 200$ K with no discernable change in magnitude or dynamics across $T_* \simeq 180$ K, indicating that whatever mechanism was responsible for the tr-CD signal is not associated with the onset of orbital order at T_* . We thus posit that the tr-CD experiment is not probing any form of chirality and instead must be thought of as a $\chi^{(3)}$ response, i.e., $P_i = \chi_{ijkl}^{(3)} E_j E_k E_l$ where E_j and E_k are pump fields, E_l the probe field and P_i the radiating polarization.

Similarly, we see another strong $\chi^{(3)}$ response in THG at $T_{CDW} \approx 200$ K, that is equally sensitive to the onset of orbital order at $T_* \simeq 180$ K. Given the independent signs that each transition shows from the other during every thermal cycle, the signals clearly point to a symmetry-breaking phase transition. If the picture of orbital ordering in Figure 6.12 is correct, then the cluster multipole associated with orbital ordering, as well as the three-vector CDW, both bilinearly couple to $\chi^{(3)}$ responses suggesting that both ordering objects are of rank-3, the CDW may be considered $\varepsilon_i \varepsilon_j \varepsilon_k$ and couples both to tr-CD and THG, while the cluster multipole only couples to THG.

6.4 Conclusions

In this study, we investigated the second and third-order nonlinear optical responses of transition metal dichalcogenide 1T-TiSe₂. The lack of second-order nonlinear optical signals from this material revealed the absence of any significant changes in its achiral

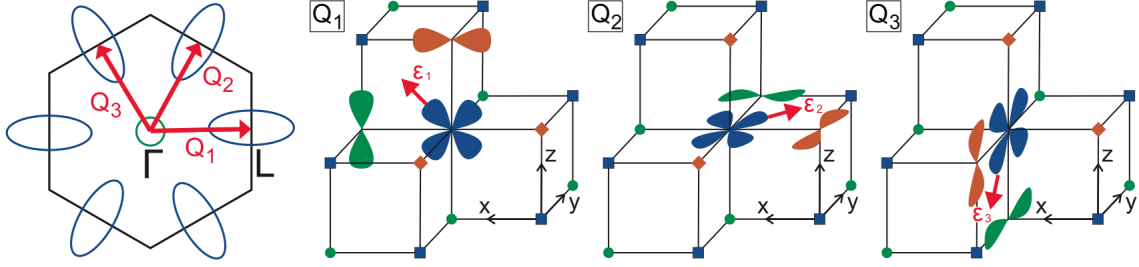


Figure 6.12: Left: Schematic representation of the Fermi surface pockets in the first Brillouin zone of TiSe_2 . The three propagation vectors of the charge density modulations connect the central Se hole pocket Γ with the Ti electron pockets at the L points. Right: The orbitals involved in the charge transfer processes of each of the three charge density wave components. The layer of Ti atoms (squares) is sandwiched between two layers of Se atoms (circles and diamonds). The resulting polarization directions of the corresponding displacement waves are indicated. We note that the orbital configurations shown here constitute a cluster multiple. Figure taken from Ref. [242].

nature below T_{CDW} . However, THG data revealed a distinct phase transition occurring at approximately 180 K. This transition was previously observed through elastic X-ray scattering and was consistent with orbital ordering transition. We observed that the domains of this order rearranged themselves randomly with each thermal cycle.

In conclusion, an investigation of the nonlinear optical responses of 1T- TiSe_2 and its phase transition behavior has been presented. By using experimental techniques such as THG spectroscopy, we provide evidence for an orbitally ordered phase transition in 1T- TiSe_2 , along with the presence of domain-type structures strongly correlated with the THG signal. A more complete understanding of the order observed at $T_* \simeq 180$ K will require RA-THG in a rotating scattering plane geometry. Work toward this objective is underway.

CHAPTER 7

TERAHERTZ EMISSION PHOTO GALVANIC EFFECT SPECTROSCOPY OF RIGHT AND LEFT HAND ENANTIOMERS OF THE CHIRAL MULTIFOLD FERMION PdGa

This chapter presents our findings on circular photogalvanic effect (CPGE) and linear photogalvanic effect (LPGE) measurements conducted in both enantiomers of the structurally chiral Weyl semimetal PdGa. Theoretical calculations predict that topological parameters, such as the Berry phase and the Chern, number undergo a sign reversal from one enantiomer to the other that can reverse the direction of the laser injected photocurrent [243]. We employed THz emission spectroscopy to measure CPGE and LPGE spectra over the 0.47 - 1.08 eV incident photon energy range. The obtained spectra exhibited mirror-image characteristics, supporting the prediction of a sign reversal in the topological parameters.

7.1 Introduction

In certain crystalline materials, the atomic arrangements lack mirror symmetry, which results in the crystal being classified as structurally chiral. Quartz is a well-known example as, depending on the spiral arrangement of silica tetrahedral, the crystal is both chiral and considered to be either right or left-handed, i.e., it is helical [244]. The Weyl semimetals belonging to space group 198, distinguish themselves from many other Weyl semimetals not only by harboring a three-fold degeneracy that technically classifies them as “multifold

fermions” of pseudospin -1 [245], but also through other physical attributes such as unusual lattice dynamics [246] and long Fermi arc surface states [247]. These materials, which are in part defined by their topological invariants, such as the Berry phase and Chern number, support novel phenomena including approximately quantized circular photogalvanic effects [248, 249] and unusual magnetotransport phenomena [250].

Angle-Resolved Photo Emission Spectroscopy (ARPES) and Scanning Tunneling Microscopy (STM), have provided evidence for the existence of large surface Fermi arcs in space group 198 materials [245, 251, 252]. However, while these measurements provide valuable information on the equilibrium band structure and density of states, they do not directly probe material response, in particular as it relates to structural symmetry and topological properties. The second-order nonlinear optical responses CPGE and LPGE are odd with respect to inversion, which suggests a possible method to detect the relationship between structural chirality and topology [247]. In a theoretical study centered on this space group, Y. Sun et al. studied the relationship between structural chirality and chiral multi-fold fermions in second-order optical response and showed the nonzero independent tensor elements for both CPGE and LPGE are inverted between the two enantiomers, as shown in Figures 7.1a and 7.1d [243]. A representative diagram of the opposite direction of current flow between two such opposite helicity samples is shown for CPGE in Figures 7.1b and 7.1c, and for LPGE in 7.1e and 7.1f.

Here, we used THz emission spectroscopy to measure the bulk CPGE and LPGE spectra of both enantiomers of (111) oriented PdGa. In PdGa, structural chirality is manifest through the helical arrangement of Ga atoms in the unit cell, as shown in Figure 7.2a from a topological view, PdGa hosts complementary Weyl nodes at the Γ and R points of the Brillouin zone as represented schematically in Figure 7.2b. These modes are not constrained to be coincident in energy due to the lack of mirror-plane symmetries. Structurally chirality is also relevant to the change in sign of the topological charge as the structural handedness

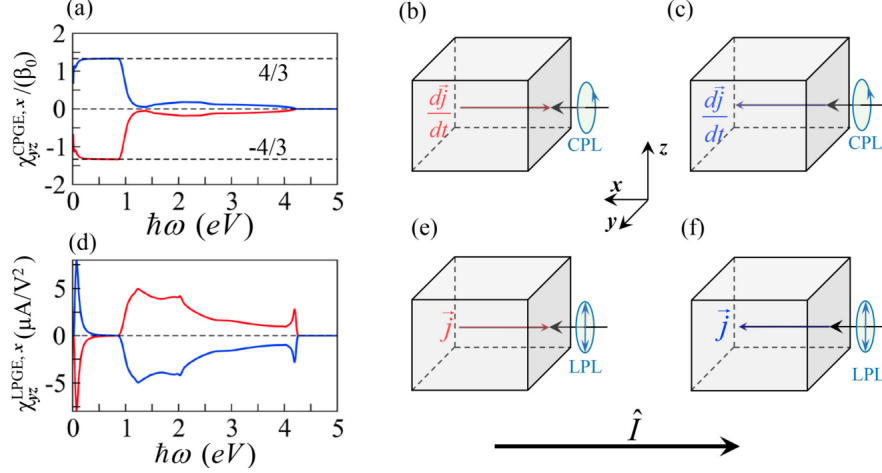


Figure 7.1: Frequency-dependent second-order conductivity for (a) CPGE and (d) LPGE derived from numerical calculations based on a tight binding model of RhSi. The red and blue curves correspond to responses from the opposite chirality of the chiral fermions. The signs of all conductivities flip with the inversion of chirality of the crystal structure. Schematic of the experimental setup to identify multifold fermions in crystals with opposite chiralities by (b), (c) CPGE and (e), (f) LPGE. CPL in (b), (c) represents circularly polarized light, and LPL in (e), (f) represents linearly polarized light. Figure taken from Ref. [243].

is inverted. The effect is that at least signed second-order nonlinear optical probes should also change sign for the two enantiomers.

7.2 Experimental Setup

The photocurrent j_i in CPGE and LPGE is given by,

$$\frac{dj_i^{cpge}(0)}{dt} = \beta_{ij}[\mathbf{E}(\omega) \times \mathbf{E}^*(\omega)]_j \quad (7.2-1)$$

$$j_i^{lpge}(0) = \eta_{ijk}\tilde{E}_j(\omega)\tilde{E}_k(-\omega) \quad (7.2-2)$$

where, β_{ij} and η_{ijk} are the CPGE and LPGE tensors, respectively, $j_i^{cpge}(0)$ and $j_i^{lpge}(0)$ are the CPGE and LPGE photocurrents respectively, and the subscript $i = x, y, z$ defines the direction of the photocurrent. The direction of the photocurrent is reversed if the sign of

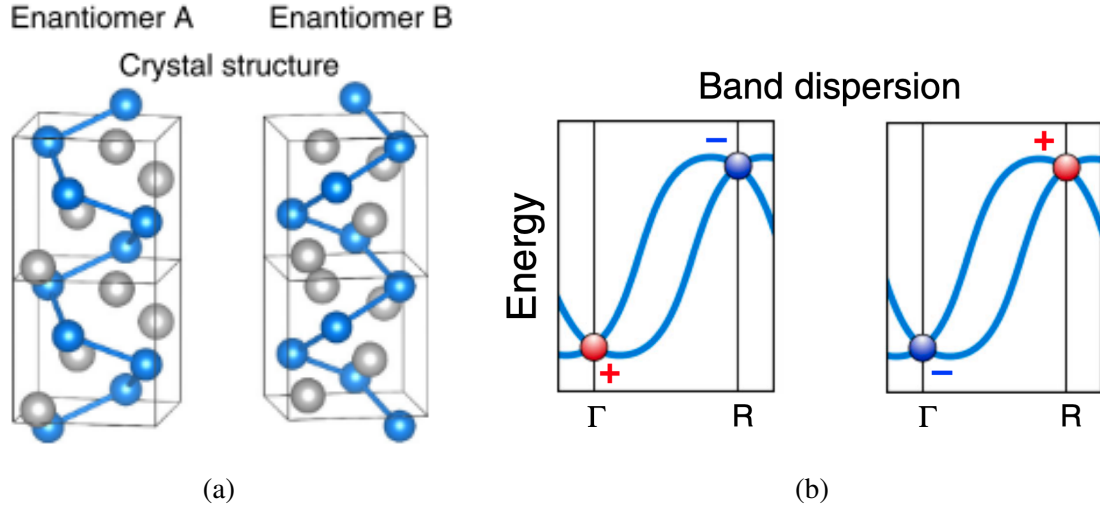


Figure 7.2: (a) Crystal structure of two opposite-handedness enantiomers of PdGa. Gray and blue atoms correspond to Pd and Ga atoms, respectively. Structural chirality can be distinguished by helices formed by the Ga atoms (b) Schematic symmetry-protected band crossings at the Γ and R points. The Chern number is inverted by the mirror operation. Figure taken from Ref. [253].

the Chern number changes [243].

The choice of PdGa was motivated by the fact that as of the time of the writing of this thesis, it is the only space group 198 material that can be controllably grown as either enantiomer. This provided an experimental handle to demonstrate the influence of structural chirality on the direction of Berry curvature flow in momentum space. To measure the LPGE and CPGE spectrum of enantiomers of PdGa, we used the experimental apparatus depicted in Fig.7.3.

This apparatus employed a regenerative amplifier laser system that emitted 800 nm pulses with 35 fs duration and a 5 kHz repetition rate. This laser seeded an Optical Parametric Amplifier (OPA) that could provide continuously tunable output from 490 nm - 16 μm , though our investigations specifically focused on wavelengths between 1140 nm and 2600 nm.

In order to achieve a high degree of polarization purity in the OPA output, we used a wire-grid polarizer after the OPA [Thorlabs, WP12L-UB] that also removed parasitic out-

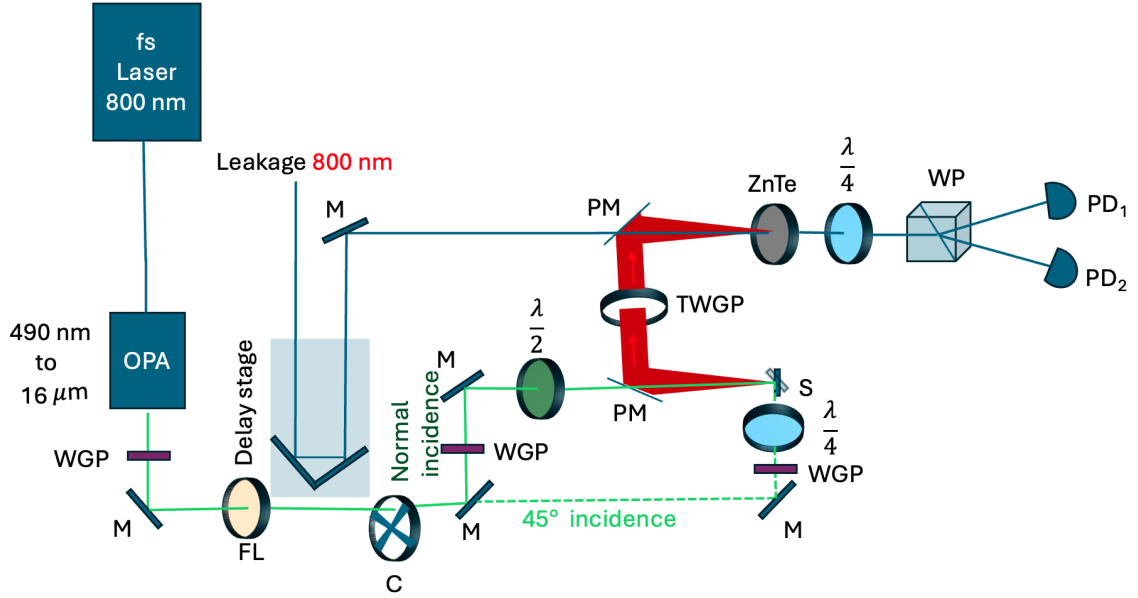


Figure 7.3: Experimental setup used here for THz emission spectroscopy. Optics are: FL - longpass filter, C - optical chopper wheel, WGP - wire-grid polarizer, M - mirror, PM - parabolic mirror, $\frac{\lambda}{4}$ - quarter waveplate, $\frac{\lambda}{2}$ - half waveplate, TWGP - THz wire-grid polarizer, S - sample, WP - Wollaston prism, PD₁, PD₂ detectors. The setup has two optical geometries for the pump beam: Normal incidence on the sample was used for LPGE measurements and 45° incidence to the sample was used for CPGE measurements. The THz radiation from the sample was collected and collimated using an off-axis parabolic mirror. The collimated THz radiation passed through a THz wire-grid polarizer and was focused onto a ZnTe crystal by a second off axis parabola for electro-optical sampling measurement using mechanically delayed 800nm light.

put beams with orthogonal polarization. A sequence of filters [Thorlabs FELH0900 for 1400 to 1600 nm, Thorlabs FELH1500 for 1600 to 2600 nm] was used to further eliminate extraneous wavelengths. The pump beam's intensity was modulated by a mechanical chopper operating at 2.5 kHz. A combination of half and quarter-wave plates was used for precise adjustment of the incident pump polarization on the sample. For the CPGE measurements, we arranged for the laser beam to strike the sample at a 45° angle. In contrast, our LPGE measurements were conducted at normal incidence of the beam on the sample surface.

As shown in Figure 7.3, the THz radiation emitted from the photocurrents was collected by an off-axis parabolic mirror, passed through a THz to ensure the choice of measured

polarization, which is parallel to the component of the driven current, and then focused onto a ZnTe (110) crystal by the other off-axis parabolic mirror.

The signal amplitude of the THz field was recorded through the electro-optic sampling technique [254] in the ZnTe crystal using an 800 nm beam taken from leakage and then mechanically delayed with a piezo-driven delay stage to build up the THz transient. The resultant modulation in the optical pulse's polarization state was enhanced using an optical biasing technique after passage through a Wollaston prism (WP). The optical biasing technique increases sensitivity in the measurements [255]. Data acquisition was performed using a DAC-based balanced detection scheme [175], as briefly discussed in Chapter 4 of this thesis.

7.3 Results and Discussion

Representative THz transients from our LPGE experiments are presented in Figure 7.4a. The opposite sign nature of the transients is due to the two enantiomers. The THz field magnitude is proportional to the current driven by Equation 7.2-2, which is a function of incident polarization and photon energy. The time-domain response for both experiments closely resembled the second derivative of a Gaussian function with a small admixture of first derivative. To quantitatively analyze these dynamics, we fit the data using a combination of the first and second derivatives of a Gaussian function. As the LPGE tensor η_{ijk} depended only on one element η_{xyz} in this space group, we used the THz radiation along the (100) axis. In space group 198 the magnitude of LPGE response as a function of incident polarization ϕ is

$$E_H = \frac{2}{3}[\eta_{xyz}(0; \omega, -\omega) \cos(2\phi)] \quad (7.3-3)$$

which matches the form of the data shown in Figure 7.4b. Also shown in Figure 7.4b is a fit to Equation 7.3-3. These fits were normalized by incident fluence using a standard

procedure. The fits were compiled as a function of incident wavelength to yield the data in Figure 7.4c where we see that η_{xyz} does change sign between enantiomers as expected.

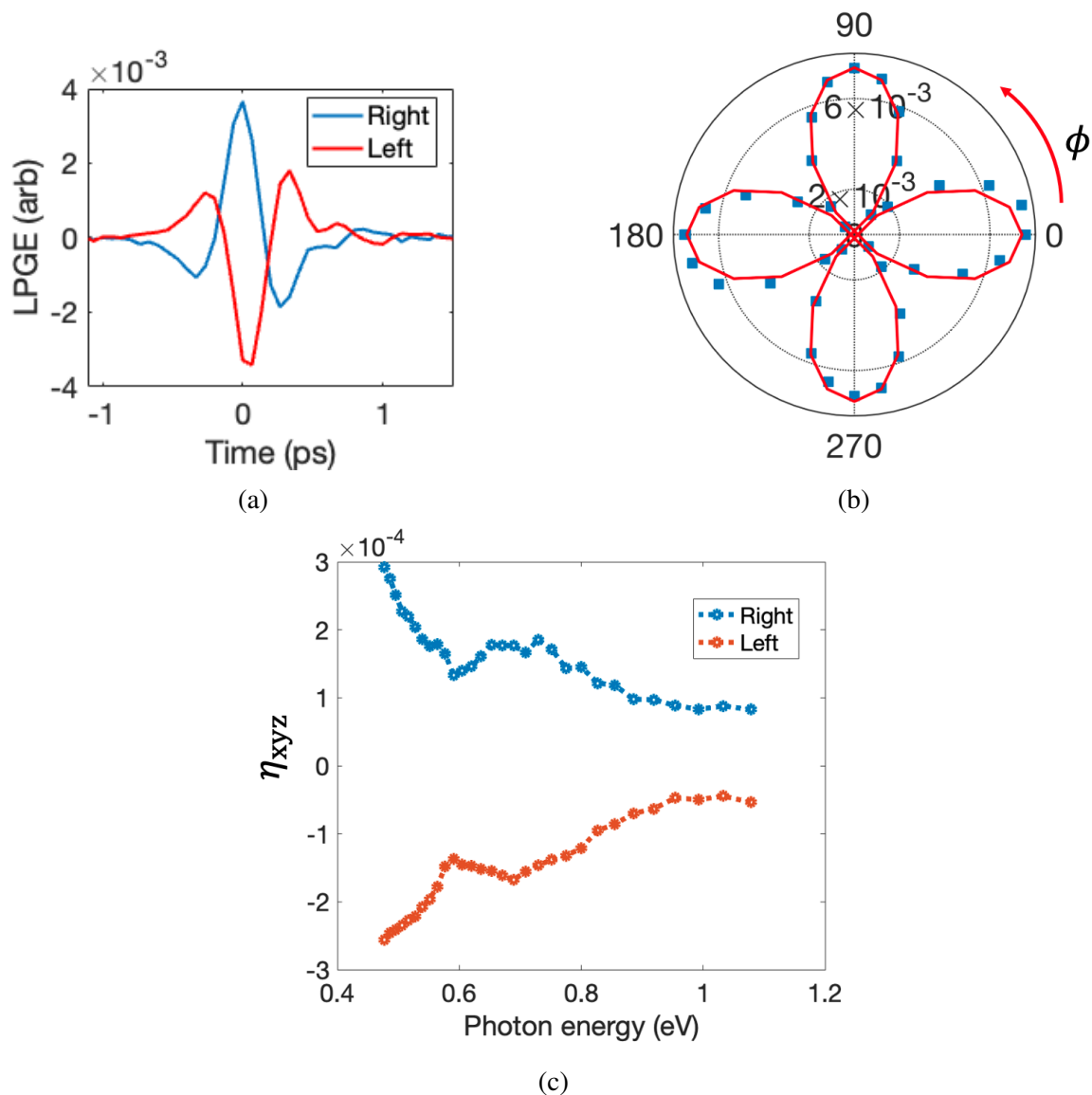


Figure 7.4: THz time-domain data for LPGE with spectra for both PdGa enantiomers. (a) transient data for left-handed (red) and right-handed (blue) PdGa samples. (b) polarization-dependent LPGE THz radiation (blue) and fitting with Equation 7.3-3 (red). On a polar plot, both enantiomers will produce the same rotational anisotropy plots but with opposite signs that cannot be replicated in a polar plot. radiate with the same patterns. (c) The spectra obtained by fitting the transients to the second derivative of a Gaussian function and normalizing by incident fluence.

We now turn to our CPGE measurements. Representative THz transients from our CPGE experiments are presented in Figure 7.5a. As in the LPGE measurements, the opposite nature of transients is due to the flow of the currents between the two enantiomers. In order to produce a CPGE spectrum, we took the difference between the responses driven by the right and left-hand circularly polarized pump beams and fit to the second derivative of the Gaussian. These values were normalized by incident fluence in the same manner as the LPGE spectrum.

The spectra obtained from this procedure are shown in Figure 7.5b. Notably, both sets of spectra appear as mirror images of one another, verifying the relationship between structural chirality and nonlinear optical response. We note that the pronounced peak at approximately 0.68 eV in the CPGE spectrum corresponds to a similar peak predicted for the linear optical conductivity [111]. These transitions occur between parallel bands connecting the Γ and R points, as well as the M and R points in the band structure, as shown in Figure 7.6.

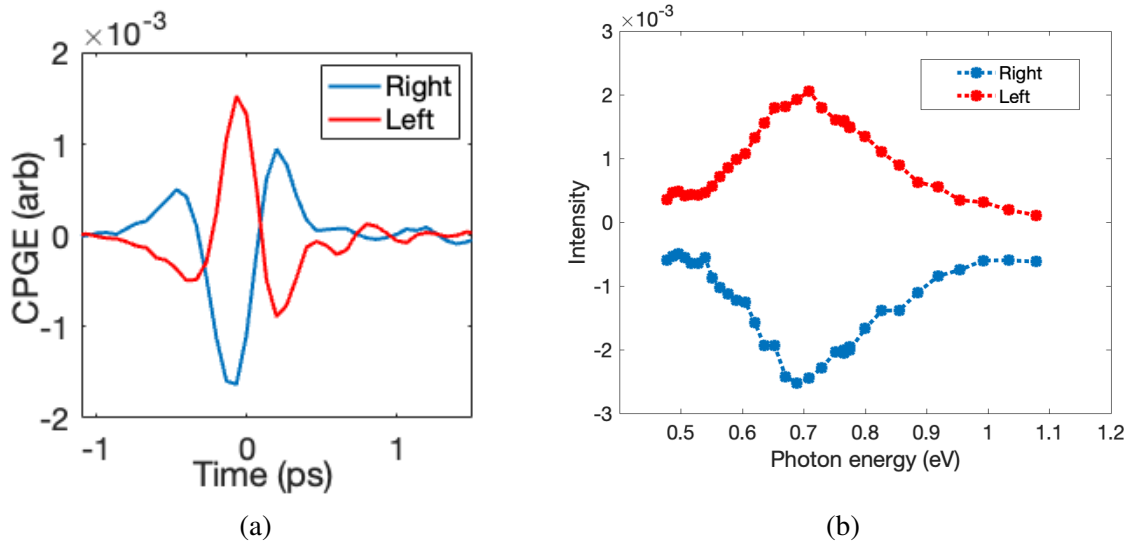


Figure 7.5: THz time-domain data for CPGE with spectra (a) transient data for left-handed (right-handed) are in red (blue). (b) Spectrum obtained by fitting transient data with the Gaussian function. The spectrum peak ~ 680 meV is due to optical transition between parallel bands between the Γ and R points.

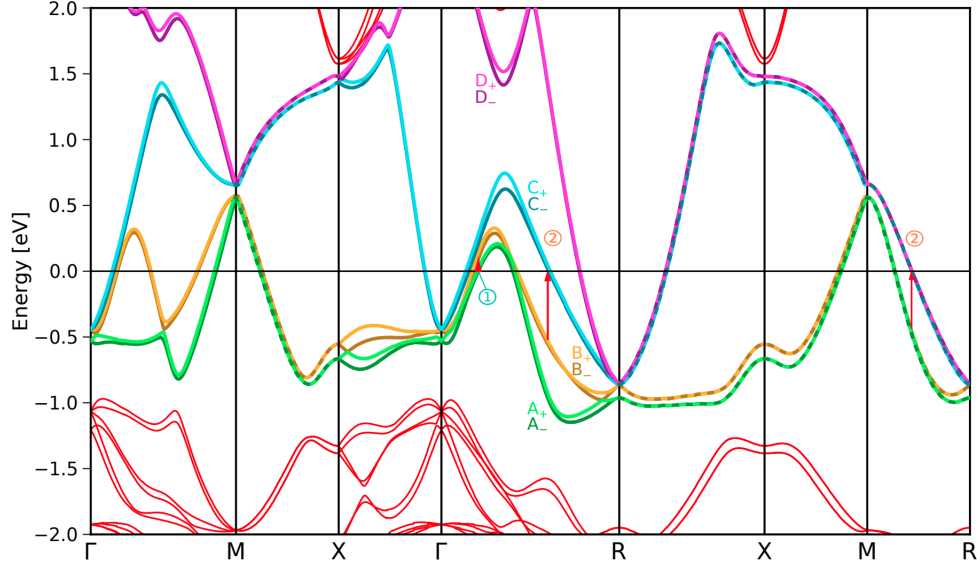


Figure 7.6: Band structure of PdGa with spin-orbit coupling (SOC). Bands that cross the Fermi surface are labeled in pairs A_{\pm} to D_{\pm} , with respect to their energy. The Fermi energy is positioned at $E_F = 0$ eV. The label \pm refer to spin pairs, which split away from high symmetry points. This splitting, due to lack of inversion and mirror symmetries, gives rise to a 4-fold intersection at Γ and 6-fold intersection at R, both with Chern numbers of magnitude $\chi = 4$. Figure taken from Ref. [111].

7.4 Conclusions

We have measured the spectral dependence of the circular photogalvanic effect (CPGE) and the linear photogalvanic effect (LPGE) in enantiomeric pairs of structurally chiral multifold fermion material using THz emission spectroscopy. Our primary observation is the opposite signs of the CPGE and LPGE spectra, which reveals the direct link between the topological and structural properties of the material and supports theoretical predictions by Yan et al. regarding structurally chiral Weyl semimetals. Future work will center on examining the surface LPGE and CPGE responses that couple to the helicoidal surface Fermi arc states since they report on topological properties much more directly. Work toward this objective is already underway.

CHAPTER 8

CONCLUSIONS

In this thesis, we have used time-resolved and nonlinear optical spectroscopy to uncover both an intrinsic, nonlinear form of electromagnetically induced chirality (EIC) deriving from electronic hybridization in the paramagnetic phase of the LnAlSi (Ln= La, Ce, Pr and Nd) series of Weyl semimetals and unconventional electronic ordering in the charge density wave (CDW) phase of the transition metal dichalcogenide (TMD) 1T–TiSe₂. We have also used THz emission spectroscopy to investigate the relationship between the topological and structural properties of enantiomeric pairs of the chiral Weyl semimetal PdGa.

Our rotational anisotropy second harmonic generation (RA-SHG) measurements on LnAlSi in their paramagnetic phase revealed a novel, nonlinear form of EIC that derives from resonant magnetic dipole (MD) transitions. This novel EIC is due to a quantum interference between the narrow band f - orbitals of the Ln⁺³ ion and a broad electric dipole resonance stemming from highly dispersive bands from d - and p - like orbitals that present as a Fano resonance in the MD SHG spectrum. This nonlinear EIC, which is a form of nonlinear magnetoelectricity governed by $P_i = \chi_{ijk}^{em} E_j H_k$, gives rise to the emission of elliptically polarized SHG from normally incident, linearly polarized fundamental light. This effect has not been observed before at nonlinear order, nor has it been observed as an intrinsic property of the bandstructure, instead relying upon either external electromagnetic fields, collective excitation or magnetic ordering to be observed at linear order. While the effect observed here did not rely upon magnetic ordering, magnetism may allow for the $M_i = \chi_{ijk}^{me} E_j E_k$ response to also be activated, realizing the complete nonlinear constitutive relations of chiral media at second order. Thus, we propose that experiments at low

temperatures should be conducted with the aim of separating the effects of time-reversal symmetry breaking from nonreciprocity due to electromagnetic chirality.

Our measurements on 1T–TiSe₂ were intended to resolve the fundamental questions surrounding the symmetry of the order parameter below the CDW transition temperature $T_{CDW} \approx 200$ K. Time-resolved circular dichroism (tr-CD) measurements appeared to show a photoinduced structure phase transition for $T \lesssim T_{CDW}$ into a transient, structurally chiral state. However, a null result from tr-SHG measurements immediately put that notion to rest.

Further static SHG measurements also suggested the absence of any significant changes to its achiral structure below T_{CDW} , as evidenced by the lack of bulk second-order nonlinear optical signals. However, our third harmonic generation (THG) data revealed two separate transitions at $T_{CDW} \approx 200$ K and $T_* \approx 180$ K, both of which were observed to independently produce either an increasing or decreasing THG response, indicating the probe lengthscale was small enough to discern between domains of each response. Taken together, we have argued that the transition at $T_{CDW} \approx 200$ K is a CDW transition into a structurally achiral phase, and the transition at $T_* \approx 180$ K is due to orbital ordering that is also achiral. Specifically, the orbital ordering is consistent with a cluster multipole driven by charge transfer between the Se p and Ti d - orbitals that is representable by a time-reversal even, parity-even rank-3 electrical toroidal multipole. However, further RA-THG experiments conducted with a rotating scattering plane geometry will be required to uniquely determine the nature of the order parameter's symmetry. As the domains were observed to produce signal that either increased or decreased with change in temperature, indicating that spatially, they could orient in at least two directions, we propose that imaging experiments should be conducted to obtain information on their morphology. This visual representation of the domain structure could further determine the nature of the symmetry breaking phases at T_{CDW} and T_* .

Finally, our linear photogalvanic effect (LPGE) and circular photogalvanic effect (CPGE) measurements on the two enantiomers of PdGa revealed signals of opposite sign. This observation aligns with the theoretical prediction that the laser-driven current flow should be in opposite directions in each enantiomer due to the material's topological and structural properties. Further measurement should focus exclusively on the topological features of the surface Fermi arc states as a means of examining the link between topology and structure more closely. We expect that the helicoidal dispersion of these states should give rise to photocurrents whose orientation will spiral in the opposite direction for the two different enantiomers.

We acknowledge funding by the National Science Foundation under Award No. NSF/DMR1945222.

BIBLIOGRAPHY

- [1] Klaus von Klitzing, Gerhard Dorda, and Michael Pepper. New method for high-accuracy determination of the fine-structure constant based on quantized Hall resistance. *Physical Review Letters*, 45(6):494, 1980.
- [2] Liang Fu and Charles L Kane. Topological insulators with inversion symmetry. *Physical Review B*, 76(4):045302, 2007.
- [3] ZK Liu, Bo Zhou, Yong Zhang, ZJ Wang, HM Weng, Dharmalingam Prabhakaran, S-K Mo, ZX Shen, Zhong Fang, Xi Dai, Z. Hussain, and Y. L. Chen. Discovery of a three-dimensional topological Dirac semimetal, Na_3Bi . *Science*, 343(6173):864–867, 2014.
- [4] Xiao-Liang Qi and Shou-Cheng Zhang. Topological insulators and superconductors. *Reviews of Modern Physics*, 83(4):1057, 2011.
- [5] Zhijun Wang, Yan Sun, Xing-Qiu Chen, Cesare Franchini, Gang Xu, Hongming Weng, Xi Dai, and Zhong Fang. Dirac semimetal and topological phase transitions in A_3Bi ($\text{A} = \text{Na}, \text{K}, \text{Rb}$). *Physical Review B*, 85(19):195320, 2012.
- [6] Chen Fang, Yige Chen, Hae-Young Kee, and Liang Fu. Topological nodal line semimetals with and without spin-orbital coupling. *Physical Review B*, 92(8):081201, 2015.
- [7] M Mogi, M Kawamura, R Yoshimi, A Tsukazaki, Y Kozuka, N Shirakawa, KS Takahashi, M Kawasaki, and Y Tokura. A magnetic heterostructure of topological insulators as a candidate for an axion insulator. *Nature Materials*, 16(5):516–521, 2017.
- [8] Kostya S Novoselov, Andre K Geim, Sergei V Morozov, De-eng Jiang, Yanshui Zhang, Sergey V Dubonos, Irina V Grigorieva, and Alexandr A Firsov. Electric field effect in atomically thin carbon films. *Science*, 306(5696):666–669, 2004.
- [9] Mark P Levendorf, Cheol-Joo Kim, Lola Brown, Pinshane Y Huang, Robin W Havener, David A Muller, and Jiwoong Park. Graphene and boron nitride lateral heterostructures for atomically thin circuitry. *Nature*, 488(7413):627–632, 2012.
- [10] Branimir Radisavljevic, Aleksandra Radenovic, Jacopo Brivio, Valentina Giacometti, and Andras Kis. Single-layer MoS_2 transistors. *Nature Nanotechnology*, 6(3):147–150, 2011.

- [11] Charles L Kane and Eugene J Mele. Z_2 topological order and the quantum spin Hall effect. *Physical Review Letters*, 95(14):146802, 2005.
- [12] Yoichi Ando. Topological insulator materials. *Journal of the Physical Society of Japan*, 82(10):102001, 2013.
- [13] M Zahid Hasan and Charles L Kane. Colloquium: topological insulators. *Reviews of Modern Physics*, 82(4):3045, 2010.
- [14] NP Armitage, EJ Mele, and Ashvin Vishwanath. Weyl and Dirac semimetals in three-dimensional solids. *Reviews of Modern Physics*, 90(1):015001, 2018.
- [15] Nitesh Kumar, Yan Sun, Nan Xu, Kaustuv Manna, Mengyu Yao, Vicky Süß, Inge Leermakers, Olga Young, Tobias Förster, Marcus Schmidt, Borrmann Horst, Binghai Yan, Uli Zeitler, Ming Shi, Claudia Felser, and Chandra Shekhar. Extremely high magnetoresistance and conductivity in the type-II Weyl semimetals WP_2 and MoP_2 . *Nature Communications*, 8(1):1642, 2017.
- [16] Hao Su, Xianbiao Shi, Jian Yuan, Yimin Wan, Erjian Cheng, Chuanying Xi, Li Pi, Xia Wang, Zhiqiang Zou, Na Yu, Weiwei Zhao, Shiyan Li, and Yanfeng Guo. Multiple Weyl fermions in the noncentrosymmetric semimetal $LaAlSi$. *Physical Review B*, 103(16):165128, 2021.
- [17] Christopher M. Dodson and Rashid Zia. Magnetic dipole and electric quadrupole transitions in the trivalent lanthanide series: Calculated emission rates and oscillator strengths. *Physical Review B*, 86:125102, Sep 2012.
- [18] Mark Kasperczyk, Steven Person, Duarte Ananias, Luis D. Carlos, and Lukas Novotny. Excitation of magnetic dipole transitions at optical frequencies. *Physical Review Letters*, 114:163903, Apr 2015.
- [19] Rafi Ud Din, Xiaodong Zeng, Guo-Qin Ge, and M Suhail Zubairy. Physics of electromagnetically induced chirality and anti-symmetric wave transmission. *Journal of Modern Optics*, 66(16):1678–1687, 2019.
- [20] Manfred Fiebig, Victor V Pavlov, and Roman V Pisarev. Second-harmonic generation as a tool for studying electronic and magnetic structures of crystals. *JOSA B*, 22(1):96–118, 2005.
- [21] Nadia A Abdulrahman, Z Fan, Taishi Tonooka, Sharon M Kelly, Nikolaj Gadegaard, Euan Hendry, Alexander O Govorov, and Malcolm Kadodwala. Induced chirality through electromagnetic coupling between chiral molecular layers and plasmonic nanostructures. *Nano Letters*, 12(2):977–983, 2012.
- [22] Sajedeh Manzeli, Dmitry Ovchinnikov, Diego Pasquier, Oleg V Yazyev, and Andras Kis. 2D transition metal dichalcogenides. *Nature Reviews Materials*, 2(8):1–15, 2017.

- [23] Tao Chu, Hesameddin Ilatikhameneh, Gerhard Klimeck, Rajib Rahman, and Zhihong Chen. Electrically tunable bandgaps in bilayer MoS₂. *Nano Letters*, 15(12):8000–8007, 2015.
- [24] Nengjie Huo, Yujue Yang, Yu-Ning Wu, Xiao-Guang Zhang, Sokrates T Pantelides, and Gerasimos Konstantatos. High carrier mobility in monolayer CVD-grown MoS₂ through phonon suppression. *Nanoscale*, 10(31):15071–15077, 2018.
- [25] Drew W Lutzke, Wentao Zhang, Aslihan Suslu, Tay-Rong Chang, Hsin Lin, Horng-Tay Jeng, Sefaattin Tongay, Junqiao Wu, Arun Bansil, and Alessandra Lanzara. Electronic structure, spin-orbit coupling, and interlayer interaction in bulk MoS₂ and WS₂. *Physical Review B*, 91(23):235202, 2015.
- [26] Carmen Palacios-Berraquero. *Quantum confined excitons in 2-dimensional materials*. Springer, 2018.
- [27] Martin Holt, Paul Zschack, Hawoong Hong, MY Chou, and T-C Chiang. X-ray studies of phonon softening in TiSe₂. *Physical Review Letters*, 86(17):3799, 2001.
- [28] Jianjun Ying, Hari Paudyal, Christoph Heil, Xiao-Jia Chen, Viktor V Struzhkin, and Elena R Margine. Unusual pressure-induced periodic lattice distortion in SnSe₂. *Physical Review Letters*, 121(2):027003, 2018.
- [29] Anshul Kogar, Gilberto Antonio de La Pena, Sangjun Lee, Yizhi Fang, SX-L Sun, David B Lioi, Goran Karapetrov, Kenneth D Finkelstein, Jacob PC Ruff, Peter Abbamonte, and Stephan Rosenkranz. Observation of a charge density wave incommensuration near the superconducting dome in Cu_xTiSe₂. *Physical Review Letters*, 118(2):027002, 2017.
- [30] Emilia Morosan, Henny W Zandbergen, BS Dennis, JWG Bos, Y Onose, Tomasz Klimczuk, AP Ramirez, NP Ong, and Robert J Cava. Superconductivity in Cu_xTiSe₂. *Nature Physics*, 2(8):544–550, 2006.
- [31] Darshana Wickramaratne, Sujan Subedi, Darius H Torchinsky, G Karapetrov, and II Mazin. Photoinduced chiral charge density wave in TiSe₂. *Physical Review B*, 105(5):054102, 2022.
- [32] C Riekel. Structure refinement of TiSe₂ by neutron diffraction. *Journal of Solid State Chemistry*, 17(4):389–392, 1975.
- [33] Julia CE Rasch, Torsten Stemmler, Beate Müller, Lenart Dudy, and Recardo Manzke. 1T–TiSe₂: Semimetal or semiconductor? *Physical Review Letters*, 101(23):237602, 2008.
- [34] Junya Ishioka, YH Liu, K Shimatake, T Kurosawa, K Ichimura, Y Toda, M Oda, and S Tanda. Chiral charge-density waves. *Physical Review Letters*, 105(17):176401, 2010.

- [35] F Weber, S Rosenkranz, J-P Castellan, R Osborn, G Karapetrov, R Hott, R Heid, K-P Bohnen, and A Alatas. Electron-phonon coupling and the soft phonon mode in TiSe_2 . *Physical Review Letters*, 107(26):266401, 2011.
- [36] John A. Wilson. Concerning the semimetallic characters of TiS_2 and TiSe_2 . *Solid State Communications*, 22(9):551–553, 1977.
- [37] Baptiste Hildebrand, Thomas Jaouen, M-L Mottas, Gaël Monney, Céline Barreteau, E Giannini, DR Bowler, and Philipp Aebi. Local real-space view of the achiral 1T-TiSe_2 $2 \times 2 \times 2$ charge density wave. *Physical Review Letters*, 120(13):136404, 2018.
- [38] Ruiming Zhang, Wei Ruan, Junyao Yu, Libo Gao, Helmuth Berger, László Forró, Kenji Watanabe, Takashi Taniguchi, Ahmad Ranjbar, Rodion V Belosludov, Thomas D. Kühne, Mohammad Saeed Bahramy, and Xiaoxiang Xi. Second-harmonic generation in atomically thin 1T-TiSe_2 and its possible origin from charge density wave transitions. *Physical Review B*, 105(8):085409, 2022.
- [39] Mikhail F Limonov, Mikhail V Rybin, Alexander N Poddubny, and Yuri S Kivshar. Fano resonances in photonics. *Nature Photonics*, 11(9):543–554, 2017.
- [40] Ugo Fano, Guido Pupillo, Alberto Zannoni, and Charles W Clark. On the absorption spectrum of noble gases at the arc spectrum limit. *Journal of Research of the National Institute of Standards and Technology*, 110(6):583, 2005.
- [41] Ugo Fano. Effects of configuration interaction on intensities and phase shifts. *Physical Review*, 124(6):1866, 1961.
- [42] Robert Williams Wood. On a remarkable case of uneven distribution of light in a diffraction grating spectrum. *The London, Edinburgh, and Dublin Philosophical Magazine and Journal of Science*, 4(21):396–402, 1902.
- [43] R Rosenfelder. A Fano effect in photonuclear reactions? *Journal of Physics G: Nuclear Physics*, 5(11):L217, 1979.
- [44] Abraham Nitzan. Photon absorption and scattering in Fano anti-resonances. *Molecular Physics*, 27(1):65–80, 1974.
- [45] PF Wainwright, MJ Alguard, Günter Baum, and MS Lubell. Application of a dc Fano effect polarized electron source to low-energy electron–atom scattering. *Review of Scientific Instruments*, 49(5):571–585, 1978.
- [46] H Schmidt, KL Campman, AC Gossard, and A Imamoğlu. Tunneling induced transparency: Fano interference in intersubband transitions. *Applied Physics Letters*, 70(25):3455–3457, 1997.
- [47] Boris Luk’Yanchuk, Nikolay I Zheludev, Stefan A Maier, Naomi J Halas, Peter Nordlander, Harald Giessen, and Chong Tow Chong. The Fano resonance in plasmonic nanostructures and metamaterials. *Nature Materials*, 9(9):707–715, 2010.

- [48] Ranjan Singh, Ibraheem AI Al-Naib, Martin Koch, and Weili Zhang. Sharp Fano resonances in thz metamaterials. *Optics Express*, 19(7):6312–6319, 2011.
- [49] MV Rybin, AB Khanikaev, M Inoue, KB Samusev, MJ Steel, G Yushin, and MF Limonov. Fano resonance between mie and bragg scattering in photonic crystals. *Physical Review Letters*, 103(2):023901, 2009.
- [50] Zhihui He, Weiwei Xue, Wei Cui, Chunjiang Li, Zhenxiong Li, Lihui Pu, Jiaojiao Feng, Xintao Xiao, Xuyang Wang, and Gang Li. Tunable Fano resonance and enhanced sensing in a simple Au/TiO₂ hybrid metasurface. *Nanomaterials*, 10(4):687, 2020.
- [51] Mikhail F Limonov. Fano resonance for applications. *Advances in Optics and Photonics*, 13(3):703–771, 2021.
- [52] Hua-Jun Chen. Fano resonance induced fast to slow light in a hybrid semiconductor quantum dot and metal nanoparticle system. *Laser Physics Letters*, 17(2):025201, 2020.
- [53] Azar Vafafard, Mostafa Sahrai, Hamid Reza Hamed, and Seyyed Hossein Asadpour. Tunneling induced two-dimensional phase grating in a quantum well nanostructure via third and fifth orders of susceptibility. *Scientific Reports*, 10(1):7389, 2020.
- [54] Wei Wang, Yabin Jin, Wan Wang, Bernard Bonello, Bahram Djafari-Rouhani, and Romain Fleury. Robust Fano resonance in a topological mechanical beam. *Physical Review B*, 101(2):024101, 2020.
- [55] Kunyan Zhang, Tong Wang, Xiaoqi Pang, Fei Han, Shun-Li Shang, Nguyen T Hung, Zi-Kui Liu, Mingda Li, Riichiro Saito, and Shengxi Huang. Anisotropic Fano resonance in the Weyl semimetal candidate LaAlSi. *Physical Review B*, 102(23):235162, 2020.
- [56] Jianmei Li, Zirui Guo, Pinxu Li, Jingyi Liu, Xiaomin Zhai, Zeyu Chang, Wenyao Chang, Guankui Long, Binghui Niu, and Yang Guo. Magnetic Fano resonance enhanced second-harmonic generation in chiral hybrid bismuth halides. *Applied Physics Letters*, 122(9), 2023.
- [57] Masatomi Iizawa, Satoshi Kosugi, Fumihiko Koike, and Yoshiro Azuma. The quantum and classical Fano parameter q . *Physica Scripta*, 96(5):055401, 2021.
- [58] Stephen E Harris, JE Field, and A Imamoglu. Nonlinear optical processes using electromagnetically induced transparency. *Physical Review Letters*, 64(10):1107, 1990.
- [59] K-J Boller, A Imamoglu, and Stephen E Harris. Observation of electromagnetically induced transparency. *Physical Review Letters*, 66(20):2593, 1991.

- [60] JE Field, KH Hahn, and SE Harris. Observation of electromagnetically induced transparency in collisionally broadened lead vapor. *Physical Review Letters*, 67(22):3062, 1991.
- [61] VA Sautenkov, YuV Rostovtsev, H Chen, P Hsu, Girish S Agarwal, and MO Scully. Electromagnetically induced magnetochiral anisotropy in a resonant medium. *Physical Review Letters*, 94(23):233601, 2005.
- [62] Tomoyuki Yokouchi, Fumitaka Kagawa, Max Hirschberger, Yoshichika Otani, Naoto Nagaosa, and Yoshinori Tokura. Emergent electromagnetic induction in a helical-spin magnet. *Nature*, 586(7828):232–236, 2020.
- [63] F G Sedgwick. Electromagnetically induced transparency. *Wikipedia*, 2024.
- [64] Gunnar Dolling, Christian Enkrich, Martin Wegener, Costas M Soukoulis, and Stefan Linden. Low-loss negative-index metamaterial at telecommunication wavelengths. *Optics Letters*, 31(12):1800–1802, 2006.
- [65] Jürgen Kästel, Michael Fleischhauer, Susanne F Yelin, and Ronald L Walsworth. Tunable negative refraction without absorption via electromagnetically induced chirality. *Physical Review Letters*, 99(7):073602, 2007.
- [66] Michael Victor Berry. Quantal phase factors accompanying adiabatic changes. *Proceedings of the Royal Society of London. A. Mathematical and Physical Sciences*, 392(1802):45–57, 1984.
- [67] Yakir Aharonov and David Bohm. Significance of electromagnetic potentials in the quantum theory. *Physical Review*, 115(3):485, 1959.
- [68] Holger Bech Nielsen and Masao Ninomiya. No-go theorem for regularizing chiral fermions. Technical report, Science Research Council, 1981.
- [69] Charles L Kane and Eugene J Mele. Quantum spin Hall effect in graphene. *Physical Review Letters*, 95(22):226801, 2005.
- [70] Markus König, Steffen Wiedmann, Christoph Brune, Andreas Roth, Hartmut Buhmann, Laurens W Molenkamp, Xiao-Liang Qi, and Shou-Cheng Zhang. Quantum spin Hall insulator state in HgTe quantum wells. *Science*, 318(5851):766–770, 2007.
- [71] B Andrei Bernevig, Taylor L Hughes, and Shou-Cheng Zhang. Quantum spin Hall effect and topological phase transition in HgTe quantum wells. *Science*, 314(5806):1757–1761, 2006.
- [72] Shujie Tang, Chaofan Zhang, Dillon Wong, Zahra Pedramrazi, Hsin-Zon Tsai, Chunjing Jia, Brian Moritz, Martin Claassen, Hyejin Ryu, Salman Kahn, Juan Jiang, Hao Yan, Makoto Hashimoto, Donghui Lu, Robert G. Moore, Chan-Cuk Hwang, Choongyu Hwang, Zahid Hussain, Yulin Chen, Miguel M. Ugeda, Zhi Liu, Xiaoming Xie, Thomas P. Devereaux, Michael F. Crommie, Sung-Kwan Mo, and Zhi-Xun Shen. Quantum spin Hall state in monolayer $1T' - WTe_2$. *Nature Physics*, 13(7):683–687, 2017.

- [73] Xiao Li, Fan Zhang, and Qian Niu. Unconventional quantum Hall effect and tunable spin Hall effect in Dirac materials: application to an isolated MoS₂ trilayer. *Physical Review Letters*, 110(6):066803, 2013.
- [74] Xiaofeng Qian, Junwei Liu, Liang Fu, and Ju Li. Quantum spin Hall effect in two-dimensional transition metal dichalcogenides. *Science*, 346(6215):1344–1347, 2014.
- [75] M Zahid Hasan and Joel E Moore. Three-dimensional topological insulators. *Annual Review of Condensed Matter Physics.*, 2(1):55–78, 2011.
- [76] ZK Liu, Jianzhong Jiang, Bo Zhou, ZJ Wang, Yi Zhang, HM Weng, Dharmalingam Prabhakaran, Sung Kwan Mo, Han Peng, Pavel Dudin, T Kim, M Hoesch, Z Fang, X Dai, ZX Shen, DL Feng, Z Hussain, and YL Chen. A stable three-dimensional topological Dirac semimetal Cd₃As₂. *Nature Materials*, 13(7):677–681, 2014.
- [77] Su-Yang Xu, Ilya Belopolski, Nasser Alidoust, Madhab Neupane, Guang Bian, Chenglong Zhang, Raman Sankar, Guoqing Chang, Zhujun Yuan, Chi-Cheng Lee, Shin-Ming Huang, Hao Zheng, Jie Ma, Daniel S. Sanchez, BaoKai Wang, Arun Bansil, Fangcheng Chou, Pavel P. Shibayev, Hsin Lin, Shuang Jia, and M. Zahid Hasan. Discovery of a Weyl fermion semimetal and topological Fermi arcs. *Science*, 349(6248):613–617, 2015.
- [78] Binghai Yan and Claudia Felser. Topological materials: Weyl semimetals. *Annual Review of Condensed Matter Physics*, 8:337–354, 2017.
- [79] AA Burkov. Topological semimetals. *Nature Materials*, 15(11):1145–1148, 2016.
- [80] Yan Sun, Shu-Chun Wu, and Binghai Yan. Topological surface states and Fermi arcs of the noncentrosymmetric Weyl semimetals TaAs, TaP, NbAs, and NbP. *Physical Review B*, 92(11):115428, 2015.
- [81] Chi-Cheng Lee, Su-Yang Xu, Shin-Ming Huang, Daniel S Sanchez, Ilya Belopolski, Guoqing Chang, Guang Bian, Nasser Alidoust, Hao Zheng, Madhab Neupane, Baokai Wang, Arun Bansil, M. Zahid Hasan, and Hsin Lin. Fermi surface interconnectivity and topology in Weyl fermion semimetals TaAs, TaP, NbAs, and NbP. *Physical Review B*, 92(23):235104, 2015.
- [82] Alexey A Soluyanov, Dominik Gresch, Zhijun Wang, QuanSheng Wu, Matthias Troyer, Xi Dai, and B Andrei Bernevig. Type-II Weyl semimetals. *Nature*, 527(7579):495–498, 2015.
- [83] Heng Gao, Jörn WF Venderbos, Youngkuk Kim, and Andrew M Rappe. Topological semimetals from first principles. *Annual Review of Materials Research*, 49:153–183, 2019.

- [84] Ke Deng, Guoliang Wan, Peng Deng, Kenan Zhang, Shijie Ding, Eryin Wang, Mingzhe Yan, Huaqing Huang, Hongyun Zhang, Zhilin Xu, Jonathan Denlinger, Alexei Fedorov, Haitao Yang, Wenhui Duan, Hong Yao, Yang Wu, Shoushan Fan, Haijun Zhang, Chen Xi, and Zhou Shuyun. Experimental observation of topological Fermi arcs in type-II Weyl semimetal MoTe_2 . *Nature Physics*, 12(12):1105–1110, 2016.
- [85] Ilya Belopolski, Su-Yang Xu, Yukiaki Ishida, Xingchen Pan, Peng Yu, Daniel S Sanchez, Hao Zheng, Madhab Neupane, Nasser Alidoust, Guoqing Chang, Tay-Rong Chang, Yun Wu, Guang Bian, Shin-Ming Huang, Chi-Cheng Lee, Daixiang Mou, Lunan Huang, You Song, Baigeng Wang, Guanghou Wang, Yao-Wen Yeh, Nan Yao, Julien E. Rault, Patrick Le Fèvre, François Bertran, Horng-Tay Jeng, Takeshi Kondo, Adam Kaminski, Hsin Lin, Zheng Liu, Fengqi Song, Shik Shin, and M. Zahid Hasan. Fermi arc electronic structure and chern numbers in the type-II Weyl semimetal candidate $\text{Mo}_x\text{W}_{1-x}\text{Te}_2$. *Physical Review B*, 94(8):085127, 2016.
- [86] Aleksandr Aleksandrovich Zyuzin and Rakesh P Tiwari. Intrinsic anomalous Hall effect in type-II Weyl semimetals. *JETP Letters*, 103:717–722, 2016.
- [87] TE O’Brien, M Diez, and CWJ Beenakker. Magnetic breakdown and Klein tunneling in a type-II Weyl semimetal. *Physical Review Letters*, 116(23):236401, 2016.
- [88] Liang Wu, Shreyas Patankar, Takahiro Morimoto, Nityan L Nair, Eric Thewalt, Arielle Little, James G Analytis, Joel E Moore, and Joseph Orenstein. Giant anisotropic nonlinear optical response in transition metal mononictide Weyl semimetals. *Nature Physics*, 13(4):350–355, 2017.
- [89] Jiawei Lai, Yinan Liu, Junchao Ma, Xiao Zhuo, Yu Peng, Wei Lu, Zheng Liu, Jianhao Chen, and Dong Sun. Broadband anisotropic photoresponse of the “hydrogen atom” version type-II Weyl semimetal candidate TaIrTe_4 . *ACS Nano*, 12(4):4055–4061, 2018.
- [90] Takahiro Morimoto and Naoto Nagaosa. Topological aspects of nonlinear excitonic processes in noncentrosymmetric crystals. *Physical Review B*, 94(3):035117, 2016.
- [91] Shreyas Patankar, Liang Wu, Baozhu Lu, Manita Rai, Jason D Tran, T Morimoto, Daniel E Parker, Adolfo G Grushin, NL Nair, JG Analytis, J. E. Moore, J. Orenstein, and D. H. Torchinsky. Resonance-enhanced optical nonlinearity in the Weyl semimetal TaAs . *Physical Review B*, 98(16):165113, 2018.
- [92] Baozhu Lu, Sharareh Sayyad, Miguel Ángel Sánchez-Martínez, Kaustuv Manna, Claudia Felser, Adolfo G Grushin, and Darius H Torchinsky. Second-harmonic generation in the topological multifold semimetal rhsI . *Physical Review Research*, 4(2):L022022, 2022.
- [93] Kazuaki Takasan, Takahiro Morimoto, Joseph Orenstein, and Joel E Moore. Current-induced second harmonic generation in inversion-symmetric Dirac and Weyl semimetals. *Physical Review B*, 104(16):L161202, 2021.

- [94] Youngjun Ahn, Xiaoyu Guo, Rui Xue, Kejian Qu, Kai Sun, David Mandrus, and Liuyan Zhao. Electric quadrupole second-harmonic generation revealing dual magnetic orders in a magnetic Weyl semimetal. *Nature Photonics*, 18(1):26–31, 2024.
- [95] MY Zhang, ZX Wang, YN Li, LY Shi, D Wu, T Lin, SJ Zhang, YQ Liu, QM Liu, J Wang, T Dong, and NL Wang. Light-induced subpicosecond lattice symmetry switch in MoTe₂. *Physical Review X*, 9(2):021036, 2019.
- [96] Petra Hein, Stephan Jauernik, Hermann Erk, Lexian Yang, Yanpeng Qi, Yan Sun, Claudia Felser, and Michael Bauer. Mode-resolved reciprocal space mapping of electron-phonon interaction in the Weyl semimetal candidate Td–WTe₂. *Nature Communications*, 11(1):2613, 2020.
- [97] Hyun-Jung Kim, Seoung-Hun Kang, Ikutaro Hamada, and Young-Woo Son. Origins of the structural phase transitions in MoTe₂ and WTe₂. *Physical Review B*, 95(18):180101, 2017.
- [98] Christian Tzschaschel, Jian-Xiang Qiu, Xue-Jian Gao, Hou-Chen Li, Chunyu Guo, Hung-Yu Yang, Cheng-Ping Zhang, Ying-Ming Xie, Yu-Fei Liu, Anyuan Gao, Damien Bérubé, Thao Dinh, Sheng-Chin Ho, Yuqiang Fang, Fuqiang Huang, Johanna Nordlander, Qiong Ma, Fazel Tafti, Philip J.W. Moll, Kam Tuen Law, and Su-Yang Xu. Nonlinear optical diode effect in a magnetic Weyl semimetal. *arXiv Preprint arXiv:2307.15603*, 2023.
- [99] Viktor Iosifovich Belinicher and Boris Itskhakovich Sturman. The photogalvanic effect in media lacking a center of symmetry. *Soviet Physics Uspekhi*, 23(3):199, 1980.
- [100] Yang Zhang, Hiroaki Ishizuka, Jeroen van den Brink, Claudia Felser, Binghai Yan, and Naoto Nagaosa. Photogalvanic effect in Weyl semimetals from first principles. *Physical Review B*, 97(24):241118, 2018.
- [101] Pavan Hosur. Circular photogalvanic effect on topological insulator surfaces: Berry-curvature-dependent response. *Physical Review B*, 83(3):035309, 2011.
- [102] Dylan Rees, Kaustuv Manna, Baozhu Lu, Takahiro Morimoto, Horst Borrmann, Claudia Felser, JE Moore, Darius H Torchinsky, and J Orenstein. Helicity-dependent photocurrents in the chiral Weyl semimetal rhsi. *Science Advances*, 6(29):eaba0509, 2020.
- [103] N Sirica, RI Tobey, LX Zhao, GF Chen, B Xu, R Yang, B Shen, DA Yarotski, P Bownan, SA Trugman, JX Zhu, YM Dai, AK Azad, N Ni, XG Qiu, AJ Taylor, and RP Prasankumar. Tracking ultrafast photocurrents in the Weyl semimetal TaAs using THz emission spectroscopy. *Physical Review Letters*, 122(19):197401, 2019.

- [104] Guoqing Chang, Jia-Xin Yin, Titus Neupert, Daniel S Sanchez, Ilya Belopolski, Songtian S Zhang, Tyler A Cochran, Zǐjiā Chéng, Ming-Chien Hsu, Shin-Ming Huang, Biao Lian, Su-Yang Xu, Hsin Lin, and M. Zahid Hasan. Unconventional photocurrents from surface Fermi arcs in topological chiral semimetals. *Physical Review Letters*, 124(16):166404, 2020.
- [105] Dylan Rees, Baozhu Lu, Yue Sun, Kaustuv Manna, Rüstem Özgür, Sujan Subedi, Horst Borrmann, Claudia Felser, Joseph Orenstein, and Darius H Torchinsky. Direct measurement of helicoid surface states in rhSi using nonlinear optics. *Physical Review Letters*, 127(15):157405, 2021.
- [106] Guoqing Chang, Bahadur Singh, Su-Yang Xu, Guang Bian, Shin-Ming Huang, Chuang-Han Hsu, Ilya Belopolski, Nasser Alidoust, Daniel S Sanchez, Hao Zheng, Hong Lu, Yi Bian, Tay-Rong Chang, Horng-Tay Jeng, Arun Bansil, Han Hsu, Shuang Jia, Titus Neupert, Hsin Lin, and M. Zahid Hasan. Magnetic and noncentrosymmetric Weyl fermion semimetals in the RAlGe family of compounds (R= rare earth). *Physical Review B*, 97(4):041104, 2018.
- [107] Jonathan Gaudet, Hung-Yu Yang, Santu Baidya, Baozhu Lu, Guangyong Xu, Yang Zhao, Jose A Rodriguez-Rivera, Christina M Hoffmann, David E Graf, Darius H Torchinsky, et al. Weyl-mediated helical magnetism in NdAlSi. *Nature Materials*, 20(12):1650–1656, 2021.
- [108] Yue Sun, Changmin Lee, Hung-Yu Yang, Darius H Torchinsky, Fazel Tafti, and Joseph Orenstein. Mapping domain-wall topology in the magnetic Weyl semimetal CeAlSi. *Physical Review B*, 104(23):235119, 2021.
- [109] Erjian Cheng, Limin Yan, Xianbiao Shi, Rui Lou, Alexander Fedorov, Mahdi Behnami, Jian Yuan, Pengtao Yang, Bosen Wang, Jin-Guang Cheng, Yuanji Xu, Yang Xu, Wei Xia, Nikolai Pavlovskii, Darren C. Peets, Weiwei Zhao, Yimin Wan, Ulrich Burkhardt, Yanfeng Guo, Shiyan Li, Claudia Felser, Wenge Yang, and Bernd Büchner. Tunable positions of Weyl nodes via magnetism and pressure in the ferromagnetic Weyl semimetal CeAlSi. *Nature Communications*, 15(1):1467, 2024.
- [110] Meng Lyu, Junsen Xiang, Zhenyu Mi, Hengcan Zhao, Zhen Wang, Enke Liu, Genfu Chen, Zhian Ren, Gang Li, and Peijie Sun. Nonsaturating magnetoresistance, anomalous Hall effect, and magnetic quantum oscillations in the ferromagnetic semimetal PrAlSi. *Physical Review B*, 102(8):085143, 2020.
- [111] Sascha Polatkan and Ece Uykur. Optical response of chiral multifold semimetal PdGa. *Crystals*, 11(2):80, 2021.
- [112] Lucky Z. Maulana, Kaustuv Manna, Ece Uykur, Claudia Felser, Martin Dressel, and Artem V. Pronin. Optical conductivity of multifold fermions: The case of RhSi. *Physical Review Research*, 2(2):023018, 2020.
- [113] Rudolf Peierls. The dynamics of charge-density waves. *Reviews of Modern Physics*, 60(4):1129, 1988.

- [114] Rudolf Ernst Peierls. *Quantum Theory of Solids*. Oxford University Press, 1955.
- [115] Herbert Fröhlich. On the theory of superconductivity: the one-dimensional case. *Proceedings of the Royal Society of London. Series A. Mathematical and Physical Sciences*, 223(1154):296–305, 1954.
- [116] Chih-Wei Chen, Jesse Choe, and E Morosan. Charge density waves in strongly correlated electron systems. *Reports on Progress in Physics*, 79(8):084505, 2016.
- [117] R Comes, M Lambert, H Launois, and HR Zeller. Evidence for a peierls distortion or a kohn anomaly in one-dimensional conductors of the type $K_2Pt(CN)_4Br_{0.30} \cdot xH_2O$. *Physical Review B*, 8(2):571, 1973.
- [118] P Monceau, NP Ong, A Meerschaut Portis, A Meerschaut, and J Rouxel. Electric field breakdown of charge-density-wave—induced anomalies in $NbSe_3$. *Physical Review Letters*, 37(10):602, 1976.
- [119] DE Moncton, JD Axe, and FJ DiSalvo. Study of superlattice formation in $2H-NbSe_2$ and $2H-TaSe_2$ by neutron scattering. *Physical Review Letters*, 34(12):734, 1975.
- [120] C Berthier, D Jerome, P Molinie, and J Rouxel. Charge density waves in layer structures: A NMR study on a $2H-NbSe_2$ single crystal. *Solid State Communications*, 19(2):131–135, 1976.
- [121] NG Stoffel, SD Kevan, and NV Smith. Experimental band structure of $1T-TiSe_2$ in the normal and charge-density-wave phases. *Physical Review B*, 31(12):8049, 1985.
- [122] CB Scruby, PM Williams, and GS Parry. The role of charge density waves in structural transformations of $1T-TaS_2$. *Philosophical Magazine*, 31(2):255–274, 1975.
- [123] He Haifeng and Zhang Dianlin. Charge density wave gap formation of $NbSe_3$ detected by electron tunneling. *Physical Review Letters*, 82(4):811, 1999.
- [124] Jacques Des Cloizeaux. Exciton instability and crystallographic anomalies in semiconductors. *Journal of Physics and Chemistry of Solids*, 26(2):259–266, 1965.
- [125] John C Slonczewski. Theory of the dynamical Jahn-Teller effect. *Physical Review*, 131(4):1596, 1963.
- [126] D Jérôme, TM Rice, and W Kohn. Excitonic insulator. *Physical Review*, 158(2):462, 1967.
- [127] Johannes Zittartz. Theory of the excitonic insulator in the presence of normal impurities. *Physical Review*, 164(2):575, 1967.
- [128] Nikolay N Bogoljubov, Vladimir Veniaminovic Tolmachov, and DV Širkov. A new method in the theory of superconductivity. *Fortschritte der Physik*, 6(11-12):605–682, 1958.

- [129] Zhi Li, Muhammad Nadeem, Zengji Yue, David Cortie, Michael Fuhrer, and Xiaolin Wang. Possible excitonic insulating phase in quantum-confined Sb nanoflakes. *Nano Letters*, 19(8):4960–4964, 2019.
- [130] Qiang Gao, Yang-hao Chan, Pengfei Jiao, Haiyang Chen, Shuaishuai Yin, Kanjana-porn Tangprapha, Yichen Yang, Xiaolong Li, Zhengtai Liu, Dawei Shen, Shengwei Jiang, and Peng Chen. Observation of possible excitonic charge density waves and metal–insulator transitions in atomically thin semimetals. *Nature Physics*, (20):597–602, 2024.
- [131] Hermann Arthur Jahn and Edward Teller. Stability of polyatomic molecules in degenerate electronic states-I-orbital degeneracy. *Proceedings of the Royal Society of London. Series A-Mathematical and Physical Sciences*, 161(905):220–235, 1937.
- [132] Ppzjld. Jahn-Teller effect. *Wikipedia*, 2024.
- [133] VV Kabanov and D Mihailovic. Manifestations of mesoscopic Jahn-Teller real-space pairing and clustering in $\text{YBa}_2\text{Cu}_3\text{O}_{7-\delta}$. *Physical Review B*, 65(21):212508, 2002.
- [134] K Rosnagel, L Kipp, and M Skibowski. Charge-density-wave phase transition in 1T-TiSe_2 : Excitonic insulator versus band-type Jahn-Teller mechanism. *Physical Review B*, 65(23):235101, 2002.
- [135] A Wegner, J Zhao, J Li, J Yang, AA Anikin, G Karapetrov, K Esfarjani, D Louca, and U Chatterjee. Evidence for pseudo-Jahn-Teller distortions in the charge density wave phase of 1T-TiSe_2 . *Physical Review B*, 101(19):195145, 2020.
- [136] Ziqiang Xu, Huixia Yang, Xuan Song, Yaoyao Chen, Han Yang, Meng Liu, Zeping Huang, Quanzhen Zhang, Jiatao Sun, Liwei Liu, and Yeliang Wang. Topical review: recent progress of charge density waves in 2D transition metal dichalcogenide-based heterojunctions and their applications. *Nanotechnology*, 32(49):492001, 2021.
- [137] Roscoe G Dickinson and Linus Pauling. The crystal structure of molybdenite. *Journal of the American Chemical Society*, 45(6):1466–1471, 1923.
- [138] JI A Wilson and AD Yoffe. The transition metal dichalcogenides discussion and interpretation of the observed optical, electrical and structural properties. *Advances in Physics*, 18(73):193–335, 1969.
- [139] RC Morris, RV Coleman, and Rajendra Bhandari. Superconductivity and magnetoresistance in NbSe_2 . *Physical Review B*, 5(3):895, 1972.
- [140] Sridevi Krishnamurthi, Mojtaba Farmanbar, and Geert Brocks. One-dimensional electronic instabilities at the edges of MoS_2 . *Physical Review B*, 102(16):165142, 2020.

- [141] Adam W Tsen, Robert Hovden, Dennis Wang, Young Duck Kim, Junichi Okamoto, Katherine A Spoth, Yu Liu, Wenjian Lu, Yuping Sun, James C Hone, Lena F Kourkoutis, Philip Kim, and Abhay N Pasupathy. Structure and control of charge density waves in two-dimensional 1T-TaS₂. *Proceedings of the National Academy of Sciences*, 112(49):15054–15059, 2015.
- [142] Sangyun Lee, Tae Beom Park, Jihyun Kim, Soon-Gil Jung, Won Kyung Seong, Namjung Hur, Yongkang Luo, Duk Y Kim, and Tuson Park. Tuning the charge density wave quantum critical point and the appearance of superconductivity in TiSe₂. *Physical Review Research*, 3(3):033097, 2021.
- [143] TE Kidd, T Miller, MY Chou, and T-C Chiang. Electron-hole coupling and the charge density wave transition in TiSe₂. *Physical Review Letters*, 88(22):226402, 2002.
- [144] H Cercellier, Claude Monney, F Clerc, Corsin Battaglia, Laurent Despont, MG Garnier, H Beck, Philipp Aebi, L Patthey, H Berger, and L Forró. Evidence for an excitonic insulator phase in 1T-TiSe₂. *Physical Review Letters*, 99(14):146403, 2007.
- [145] Bahadur Singh, Chuang-Han Hsu, Wei-Feng Tsai, Vitor M Pereira, and Hsin Lin. Stable charge density wave phase in a 1T-TiSe₂ monolayer. *Physical Review B*, 95(24):245136, 2017.
- [146] Shin-Ming Huang, Su-Yang Xu, Bahadur Singh, Ming-Chien Hsu, Chuang-Han Hsu, Chenliang Su, Arun Bansil, and Hsin Lin. Aspects of symmetry and topology in the charge density wave phase of 1T-TiSe₂. *New Journal of Physics*, 23(8):083037, 2021.
- [147] Chuan Chen, Bahadur Singh, Hsin Lin, and Vitor M Pereira. Reproduction of the charge density wave phase diagram in 1-TiSe₂ exposes its excitonic character. *Physical Review Letters*, 121(22):226602, 2018.
- [148] Shichao Yan, Davide Iaia, Emilia Morosan, Eduardo Fradkin, Peter Abbamonte, and Vidya Madhavan. Influence of domain walls in the incommensurate charge density wave state of Cu intercalated 1T-TiSe₂. *Physical Review Letters*, 118(10):106405, 2017.
- [149] Young Il Joe, XM Chen, P Ghaemi, KD Finkelstein, GA De La Peña, Y Gan, JCT Lee, S Yuan, J Geck, GJ MacDougall, T.C. Chiang, S.L Cooper, E. Fradkin, and P. Abbamonte. Emergence of charge density wave domain walls above the superconducting dome in 1T-TiSe₂. *Nature Physics*, 10(6):421–425, 2014.
- [150] F Jr Di Salvo, DE Moncton, and JV Waszczak. Electronic properties and superlattice formation in the semimetal TiSe₂. *Physical Review B*, 14(10):4321, 1976.
- [151] Katsuaki Sugawara, Yuki Nakata, Ryota Shimizu, Patrick Han, Taro Hitosugi, Takafumi Sato, and Takashi Takahashi. Unconventional charge-density-wave transition in monolayer 1T-TiSe₂. *ACS Nano*, 10(1):1341–1345, 2016.

- [152] HP Hughes. Structural distortion in TiSe_2 and related materials—a possible Jahn-Teller effect? *Journal of Physics C: Solid State Physics*, 10(11):L319, 1977.
- [153] Matthew D Watson, Oliver J Clark, Federico Mazzola, Igor Marković, Veronika Sunko, Timur K Kim, Kai Rossnagel, and Philip DC King. Orbital- and k_z -selective hybridization of Se $4p$ and Ti $3d$ states in the charge density wave phase of TiSe_2 . *Physical Review Letters*, 122(7):076404, 2019.
- [154] Anshul Kogar, Melinda S Rak, Sean Vig, Ali A Husain, Felix Flicker, Young Il Joe, Luc Venema, Greg J MacDougall, Tai C Chiang, Eduardo Fradkin, Jasper van Wezel, and Peter Abbamonte. Signatures of exciton condensation in a transition metal dichalcogenide. *Science*, 358(6368):1314–1317, 2017.
- [155] Claude Monney, EF Schwier, Michael Gunnar Garnier, N Mariotti, Clement Didiot, Hervé Cercellier, Jacques Marcus, Helmut Berger, AN Titov, Hans Beck, and P Aebi. Probing the exciton condensate phase in 1T-TiSe_2 with photoemission. *New Journal of Physics*, 12(12):125019, 2010.
- [156] Yingying Peng, Xuefei Guo, Qian Xiao, Qizhi Li, Jörg Stempfer, Yongseong Choi, Dong Yan, Huixia Luo, Yuqing Huang, Shuang Jia, Janson Oley, Peter Abbamonte, Jeroen van den Brink, and Jasper van Wezel. Observation of orbital order in the van der Waals material 1T-TiSe_2 . *Physical Review Research*, 4(3):033053, 2022.
- [157] Jasper van Wezel. Observing the chiral charge ordering transition in TiSe_2 . *Advances in Science and Technology*, 90:103–110, 2014.
- [158] Myung Hwan Whangbo and Enric Canadell. Analogies between the concepts of molecular chemistry and solid-state physics concerning structural instabilities. electronic origin of the structural modulations in layered transition metal dichalcogenides. *Journal of the American Chemical Society*, 114(24):9587–9600, 1992.
- [159] Jasper van Wezel, Paul Nahai-Williamson, and Siddarth S Saxena. Exciton-phonon-driven charge density wave in TiSe_2 . *Physical Review B*, 81(16):165109, 2010.
- [160] Michael Porer, Ursula Leierseder, J-M Ménard, Hatem Dachraoui, L Mouchliadis, IE Perakis, Ulrich Heinzmann, J Demsar, K Rossnagel, and Rupert Huber. Non-thermal separation of electronic and structural orders in a persisting charge density wave. *Nature Materials*, 13(9):857–861, 2014.
- [161] Claude Monney, Michele Puppini, CW Nicholson, M Hoesch, RT Chapman, E Springate, H Berger, A Magrez, C Cacho, Ralph Ernstorfer, and M Wolf. Revealing the role of electrons and phonons in the ultrafast recovery of charge density wave correlations in 1T-TiSe_2 . *Physical Review B*, 94(16):165165, 2016.
- [162] JJ Gao, WH Zhang, JG Si, X Luo, J Yan, ZZ Jiang, W Wang, HY Lv, P Tong, WH Song, X.B. Zhu, W.J. Lu, Y. Yin, and Y.P. Sun. Chiral charge density waves induced by Ti-doping in 1T-TaS_2 . *Applied Physics Letters*, 118(21), 2021.

- [163] Su-Yang Xu, Qiong Ma, Yang Gao, Anshul Kogar, Alfred Zong, Andrés M Mier Valdivia, Thao H Dinh, Shin-Ming Huang, Bahadur Singh, Chuang-Han Hsu, Tay-Rong Chang, Jacob PC Ruff, Kenji Watanabe, Takashi Taniguchi, Hsi Lin, Goran Karapetrov, Dai Xiao, Pablo Jarillo-Herrero, and Nuh Gedik. Spontaneous gyrotropic electronic order in a transition-metal dichalcogenide. *Nature*, 578(7796):545–549, 2020.
- [164] John-Paul Castellan, Stephan Rosenkranz, Ray Osborn, KE Gray, X Luo, U Welp, Goran Karapetrov, JPC Ruff, and Jasper van Wezel. Chiral phase transition in charge ordered 1T–TiSe₂. *Physical Review Letters*, 110(19):196404, 2013.
- [165] Wujun Shi, Benjamin J Wieder, Holger L Meyerheim, Yan Sun, Yang Zhang, Yiwei Li, Lei Shen, Yanpeng Qi, Lexian Yang, Jagannath Jena, Peter Werner, Klaus Koepf, Stuart Parkin, Yulin Chen, Claudia Felser, B. Andrei Bernevig, and Zhijun Wang. A charge-density-wave topological semimetal. *Nature Physics*, 17(3):381–387, 2021.
- [166] Yu-Xiao Jiang, Jia-Xin Yin, M Michael Denner, Nana Shumiya, Brenden R Ortiz, Gang Xu, Zurab Guguchia, Junyi He, Md Shafayat Hossain, Xiaoxiong Liu, Jacob Ruff, Linus Kautzsch, Songtian S. Zhang, Guoqing Chang, Ilya Belopolski, Qi Zhang, Tyler A. Cochran, Daniel Multer, Maksim Litskevich, Zi-Jia Cheng, Xian P. Yang, Ziqiang Wang, Ronny Thomale, Titus Neupert, Stephen D. Wilson, and M. Zahid Hasan. Unconventional chiral charge order in kagome superconductor KV₃Sb₅. *Nature Materials*, 20(10):1353–1357, 2021.
- [167] Ekaterina Möhr-Vorobeva, Steven L Johnson, Paul Beaud, Urs Staub, R De Souza, Chris Milne, Gerhard Ingold, Jure Demsar, Hanjo Schäfer, and A Titov. Nonthermal melting of a charge density wave in TiSe₂. *Physical Review Letters*, 107(3):036403, 2011.
- [168] Yuan Zhang, Junfeng Dai, Xiangli Zhong, Dongwen Zhang, Gaokuo Zhong, and Jiangyu Li. Probing ultrafast dynamics of ferroelectrics by time-resolved pump-probe spectroscopy. *Advanced Science*, 8(22):2102488, 2021.
- [169] Hermann A Dürr, Ralph Ernstorfer, and Bradley J Siwick. Revealing momentum-dependent electron–phonon and phonon–phonon coupling in complex materials with ultrafast electron diffuse scattering. *MRS Bulletin*, 46(8):731–737, 2021.
- [170] Tal Heilpern, Manoj Manjare, Alexander O Govorov, Gary P Wiederrecht, Stephen K Gray, and Hayk Harutyunyan. Determination of hot carrier energy distributions from inversion of ultrafast pump-probe reflectivity measurements. *Nature Communications*, 9(1):1853, 2018.
- [171] Deying Luo, Rui Su, Wei Zhang, Qihuang Gong, and Rui Zhu. Minimizing non-radiative recombination losses in perovskite solar cells. *Nature Reviews Materials*, 5(1):44–60, 2020.

- [172] Martin C Fischer, Jesse W Wilson, Francisco E Robles, and Warren S Warren. Invited review article: pump-probe microscopy. *Review of Scientific Instruments*, 87(3), 2016.
- [173] T Konstantinova, L Wu, W-G Yin, J Tao, GD Gu, XJ Wang, Jie Yang, IA Zaliznyak, and Y Zhu. Photoinduced Dirac semimetal in ZrTe₅. *NPJ Quantum Materials*, 5(1):80, 2020.
- [174] Paola Borri, Wolfgang Langbein, Jesper Mørk, and Jørn Marcher Hvam. Heterodyne pump-probe and four-wave mixing in semiconductor optical amplifiers using balanced lock-in detection. *Optics Communications*, 169(1-6):317–324, 1999.
- [175] Christopher A Werley, Stephanie M Teo, and Keith A Nelson. Pulsed laser noise analysis and pump-probe signal detection with a data acquisition card. *Review of Scientific Instruments*, 82(12):123108, 2011.
- [176] Chih-Wei Luo, YT Wang, FW Chen, HC Shih, and T Kobayashi. Eliminate coherence spike in reflection-type pump-probe measurements. *Optics Express*, 17(14):11321–11327, 2009.
- [177] S Bhagavantam and PV Pantulu. Generalized symmetry and neumann’s principle. In *Proceedings of the Indian Academy of Sciences-Section A*, volume 66, pages 33–39. Springer, 1967.
- [178] David A Kleinman. Theory of second harmonic generation of light. *Physical Review*, 128(4):1761, 1962.
- [179] Jeff A Squier, Michiel Müller, GJ Brakenhoff, and Kent R Wilson. Third harmonic generation microscopy. *Optics Express*, 3(9):315–324, 1998.
- [180] M Bass, PA Franken, JF Ward, and G Weinreich. Optical rectification. *Physical Review Letters*, 9(11):446, 1962.
- [181] Akihiro Morita. *Theory of sum frequency generation spectroscopy*, volume 97. Springer, 2018.
- [182] Perry T Mahon and JE Sipe. From magnetoelectric response to optical activity. *Physical Review Research*, 2(4):043110, 2020.
- [183] Jeffery J Maki, Martti Kauranen, and André Persoons. Surface second-harmonic generation from chiral materials. *Physical Review B*, 51(3):1425, 1995.
- [184] Dennis H Goldstein. *Polarized light*. CRC Press, 2017.
- [185] Baozhu Lu, Jason D Tran, and Darius H Torchinsky. Fast reflective optic-based rotational anisotropy nonlinear harmonic generation spectrometer. *Review of Scientific Instruments*, 90(5), 2019.

- [186] Hung-Yu Yang, Bahadur Singh, Jonathan Gaudet, Baozhu Lu, Cheng-Yi Huang, Wei-Chi Chiu, Shin-Ming Huang, Baokai Wang, Faranak Bahrami, Bochao Xu, Jacob Franklin, Ilya Sochnikov, David E. Graf, Guangyong Xu, Yang Zhao, Christina M. Hoffman, Hsin Lin, Darius H. Torchinsky, Collin L. Broholm, Arun Bansil, and Fazel Tafti. Noncollinear ferromagnetic Weyl semimetal with anisotropic anomalous Hall effect. *Physical Review B*, 103(11):115143, 2021.
- [187] Truman Ng, Yongzheng Luo, Jiaren Yuan, Yihong Wu, Hyunsoo Yang, and Lei Shen. Origin and enhancement of the spin Hall angle in the Weyl semimetals LaAlSi and LaAlGe. *Physical Review B*, 104(1):014412, 2021.
- [188] Jin-Feng Wang, Qing-Xin Dong, Zhao-Peng Guo, Meng Lv, Yi-Fei Huang, Jun-Sen Xiang, Zhi-An Ren, Zhi-Jun Wang, Pei-Jie Sun, Gang Li, and Gen-Fu Chen. NdAlSi: A magnetic Weyl semimetal candidate with rich magnetic phases and atypical transport properties. *Physical Review B*, 105(14):144435, 2022.
- [189] Satoshi Tomita, Hiroyuki Kurosawa, Tetsuya Ueda, and Kei Sawada. Metamaterials with magnetism and chirality. *Journal of Physics D: Applied Physics*, 51(8):083001, 2018.
- [190] Bahadur Singh. Private communication.
- [191] Christopher M Dodson and Rashid Zia. Magnetic dipole and electric quadrupole transitions in the trivalent lanthanide series: Calculated emission rates and oscillator strengths. *Physical Review B*, 86(12):125102, 2012.
- [192] Ismo Lindell, Ari Sihvola, Sergei Tretyakov, and Ari J Viitanen. *Electromagnetic waves in chiral and bi-isotropic media*. Artech House, 1994.
- [193] Herbert Wiegmann, AGM Jansen, P Wyder, J-P Rivera, and H Schmid. Magneto-electric effect of Cr₂O₃ in strong static magnetic fields. *Ferroelectrics*, 162(1):141–146, 1994.
- [194] Min-Soo Hwang, Ha-Reem Kim, Kwang-Yong Jeong, Hong-Gyu Park, and Yuri Kivshar. Novel non-plasmonic nanolasers empowered by topology and interference effects. *Nanophotonics*, 10(14):3599–3611, 2021.
- [195] Kirill Koshelev and Yuri Kivshar. Dielectric resonant metaphotonics. *Acs Photonics*, 8(1):102–112, 2020.
- [196] N Noginova, G Zhu, M Mavy, and MA Noginov. Magnetic dipole based systems for probing optical magnetism. *Journal of Applied Physics*, 103(7):07E901, 2008.
- [197] Nan Yang, Yiqiao Tang, and Adam E Cohen. Spectroscopy in sculpted fields. *Nano Today*, 4(3):269–279, 2009.
- [198] N Noginova, Yu Barnakov, H Li, and MA Noginov. Effect of metallic surface on electric dipole and magnetic dipole emission transitions in Eu³⁺ doped polymeric film. *Optics Express*, 17(13):10767–10772, 2009.

- [199] Xingjie Ni, Gururaj V Naik, Alexander V Kildishev, Yu Barnakov, Alexandra Boltasseva, and Vladimir M Shalaev. Effect of metallic and hyperbolic metamaterial surfaces on electric and magnetic dipole emission transitions. *Applied Physics B*, 103(3):553–558, 2011.
- [200] Sinan Karaveli and Rashid Zia. Strong enhancement of magnetic dipole emission in a multilevel electronic system. *Optics Letters*, 35(20):3318–3320, 2010.
- [201] Sinan Karaveli and Rashid Zia. Spectral tuning by selective enhancement of electric and magnetic dipole emission. *Physical Review Letters*, 106(19):193004, 2011.
- [202] Christian Enkrich, M Wegener, S Linden, Sven Burger, Lin Zschiedrich, Frank Schmidt, JF Zhou, Th Koschny, and CM Soukoulis. Magnetic metamaterials at telecommunication and visible frequencies. *Physical Review Letters*, 95(20):203901, 2005.
- [203] Bogdan-Ioan Popa and Steven A Cummer. Compact dielectric particles as a building block for low-loss magnetic metamaterials. *Physical Review Letters*, 100(20):207401, 2008.
- [204] Brice Rolly, Brian Stout, and Nicolas Bonod. Boosting the directivity of optical antennas with magnetic and electric dipolar resonant particles. *Optics Express*, 20(18):20376–20386, 2012.
- [205] Arseniy I Kuznetsov, Andrey E Miroshnichenko, Yuan Hsing Fu, JingBo Zhang, and Boris Luk’Yanchuk. Magnetic light. *Scientific Reports*, 2(1):1–6, 2012.
- [206] Alexander E Krasnok, Andrey E Miroshnichenko, Pavel A Belov, and Yuri S Kivshar. All-dielectric optical nanoantennas. *Optics Express*, 20(18):20599–20604, 2012.
- [207] John Brian Pendry. Negative refraction makes a perfect lens. *Physical Review Letters*, 85(18):3966, 2000.
- [208] John David Jackson. *Classical electrodynamics*, 1999.
- [209] Mirza I Bichurin. *Magnetolectric Composites*. Jenny Stanford Publishing, 2019.
- [210] Tim H Taminiau, Sinan Karaveli, Niek F Van Hulst, and Rashid Zia. Quantifying the magnetic nature of light emission. *Nature Communications*, 3(1):1–6, 2012.
- [211] Ryan A DeCrescent, Naveen R Venkatesan, Clayton J Dahlman, Rhys M Kennard, Xie Zhang, Wenhao Li, Xinhong Du, Michael L Chabinyc, Rashid Zia, and Jon A Schuller. Bright magnetic dipole radiation from two-dimensional lead-halide perovskites. *Science Advances*, 6(6):eaay4900, 2020.
- [212] Andrei Kirilyuk and Theo Rasing. Magnetization-induced-second-harmonic generation from surfaces and interfaces. *JOSA B*, 22(1):148–167, 2005.

- [213] JF McGilp. Probing surface and interface structure using optics. *Journal of Physics: Condensed Matter*, 22(8):084018, 2010.
- [214] Sava A Denev, Tom TA Lummen, Eftihia Barnes, Amit Kumar, and Venkatraman Gopalan. Probing ferroelectrics using optical second harmonic generation. *Journal of the American Ceramic Society*, 94(9):2699–2727, 2011.
- [215] Mark Kasperczyk, Steven Person, Duarte Ananias, Luis D Carlos, and Lukas Novotny. Excitation of magnetic dipole transitions at optical frequencies. *Physical Review Letters*, 114(16):163903, 2015.
- [216] Manfred Fiebig, Dietmar Fröhlich, BB Krichevtsov, and Roman V Pisarev. Second harmonic generation and magnetic-dipole-electric-dipole interference in antiferromagnetic Cr_2O_3 . *Physical Review Letters*, 73(15):2127, 1994.
- [217] Manfred Fiebig, Th Lottermoser, Victor V Pavlov, and Roman V Pisarev. Magnetic second harmonic generation in centrosymmetric CoO , NiO , and KNiF_3 . *Journal of Applied Physics*, 93(10):6900–6902, 2003.
- [218] Debanand Sa, R Valenti, and C Gros. A generalized ginzburg-landau approach to second harmonic generation. *The European Physical Journal B-Condensed Matter and Complex Systems*, 14(2):301–305, 2000.
- [219] Hung-Yu Yang, Bahadur Singh, Baozhu Lu, Cheng-Yi Huang, Faranak Bahrami, Wei-Chi Chiu, David Graf, Shin-Ming Huang, Baokai Wang, Hsin Lin, Darius Torchinsky, Arun Bansil, and Fazel Tafti. Transition from intrinsic to extrinsic anomalous Hall effect in the ferromagnetic Weyl semimetal $\text{PrAlGe}_{1-x}\text{Si}_x$. *APL Materials*, 8(1):011111, 2020.
- [220] Sébastien Cuffe, Dongfang Li, You Zhou, Franklin J Wong, Jonathan A Kurvits, Shriram Ramanathan, and Rashid Zia. Dynamic control of light emission faster than the lifetime limit using VO_2 phase-change. *Nature Communications*, 6(1):1–6, 2015.
- [221] WT Carnall, PR Fields, and K Rajnak. Spectral intensities of the trivalent lanthanides and actinides in solution. ii. Pm^{3+} , Sm^{3+} , Eu^{3+} , Gd^{3+} , Tb^{3+} , Dy^{3+} , and Ho^{3+} . *The Journal of Chemical Physics*, 49(10):4412–4423, 1968.
- [222] Keith Nelson. Private communication.
- [223] O Madelung, PG Klemens, G Neuer, GK White, B Sundqvist, and C Uher. *Thermal Conductivity of Pure Metals and Alloys/Wärmeleitfähigkeit von Reinen Metallen Und Legierungen*, volume 3. Springer, 1991.
- [224] Deji Akinwande, Christopher J Brennan, J Scott Bunch, Philip Egberts, Jonathan R Felts, Huajian Gao, Rui Huang, Joon-Seok Kim, Teng Li, Yao Li, Kenneth M. Liechti, Nanshu Lu, Harold S. Park, Evan J. Reed, Peng Wang, Boris I. Yakobson, Teng Zhang, Yong-Wei Zhang, Yao Zhou, and Yong Zhu. A review on mechanics and mechanical properties of 2D materials—graphene and beyond. *Extreme Mechanics Letters*, 13:42–77, 2017.

- [225] Wenzhi Yu, Kaiwen Gong, Yanyong Li, Binbin Ding, Lei Li, Yongkang Xu, Rong Wang, Lianbi Li, Guangyu Zhang, and Shenghuang Lin. Flexible 2D materials beyond graphene: synthesis, properties, and applications. *Small*, 18(14):2105383, 2022.
- [226] Zhiyong Y Zhu, Yingchun C Cheng, and Udo Schwingenschlögl. Giant spin-orbit-induced spin splitting in two-dimensional transition-metal dichalcogenide semiconductors. *Physical Review B*, 84(15):153402, 2011.
- [227] Ethan C Ahn. 2D materials for spintronic devices. *NPJ 2D Materials and Applications*, 4(1):17, 2020.
- [228] Richard A Klemm. Pristine and intercalated transition metal dichalcogenide superconductors. *Physica C: Superconductivity and its Applications*, 514:86–94, 2015.
- [229] P Chen, Y-H Chan, X-Y Fang, S-K Mo, Z Hussain, A-V Fedorov, MY Chou, and T-C Chiang. Hidden order and dimensional crossover of the charge density waves in 1T–TiSe₂. *Scientific Reports*, 6(1):37910, 2016.
- [230] Martin R Otto, Jan-Hendrik Pöhls, Laurent P René de Cotret, Mark J Stern, Mark Sutton, and Bradley J Siwick. Mechanisms of electron-phonon coupling unraveled in momentum and time: The case of soft phonons in TiSe₂. *Science Advances*, 7(20):eabf2810, 2021.
- [231] Antoine Comby, Samuel Beaulieu, Martial Boggio-Pasqua, Dominique Descamps, Francois Légaré, Laurent Nahon, Stéphane Petit, Bernard Pons, Baptiste Fabre, Yann Mairesse, and Valerie Blanchet. Relaxation dynamics in photoexcited chiral molecules studied by time-resolved photoelectron circular dichroism: Toward chiral femtochemistry. *The Journal of Physical Chemistry Letters*, 7(22):4514–4519, 2016.
- [232] David J Kissick, Debbie Wanapun, and Garth J Simpson. Second-order nonlinear optical imaging of chiral crystals. *Annual Review of Analytical Chemistry*, 4:419–437, 2011.
- [233] MA Belkin and YR Shen. Non-linear optical spectroscopy as a novel probe for molecular chirality. *International Reviews in Physical Chemistry*, 24(2):257–299, 2005.
- [234] AJ Sabbah and D Mark Riffe. Femtosecond pump-probe reflectivity study of silicon carrier dynamics. *Physical Review B*, 66(16):165217, 2002.
- [235] Andreas Othonos. Probing ultrafast carrier and phonon dynamics in semiconductors. *Journal of Applied Physics*, 83(4):1789–1830, 1998.
- [236] L Zhao, DH Torchinsky, H Chu, V Ivanov, R Lifshitz, R Flint, T Qi, G Cao, and D Hsieh. Evidence of an odd-parity hidden order in a spin-orbit coupled correlated iridate. *Nature Physics*, 12(1):32–36, 2016.

- [237] DH Torchinsky, H Chu, L Zhao, NB Perkins, Y Sizyuk, T Qi, Gang Cao, and D Hsieh. Structural distortion-induced magnetoelastic locking in Sr_2IrO_4 revealed through nonlinear optical harmonic generation. *Physical Review Letters*, 114(9):096404, 2015.
- [238] A de La Torre, Sergio Di Matteo, D Hsieh, and MR Norman. Implications of second harmonic generation for hidden order in $\text{Sr}_2\text{CuO}_2\text{Cl}_2$. *Physical Review B*, 104(3):035138, 2021.
- [239] Hiroki Ueda, Michael Porer, José RL Mardegan, Sergii Parchenko, Namrata Gurung, Federica Fabrizi, Mahesh Ramakrishnan, Larissa Boie, Martin Josef Neugebauer, Bulat Burganov, Max Burian, Steven Lee Johnson, Kai Rossnagel, and Urs Staub. Correlation between electronic and structural orders in 1T-TiSe_2 . *Physical Review Research*, 3(2):L022003, 2021.
- [240] Christian Stingl, RS Perry, Y Maeno, and Philipp Gegenwart. Symmetry-breaking lattice distortion in $\text{Sr}_3\text{Ru}_2\text{O}_7$. *Physical Review Letters*, 107(2):026404, 2011.
- [241] Satoru Hayami, Megumi Yatsushiro, Yuki Yanagi, and Hiroaki Kusunose. Classification of atomic-scale multipoles under crystallographic point groups and application to linear response tensors. *Physical Review B*, 98(16):165110, 2018.
- [242] Jasper Van Wezel. The chiral charge density wave transition in 1T-TiSe_2 . In *Journal of Physics: Conference Series*, volume 391, page 012167. IOP Publishing, 2012.
- [243] Yan Sun, Qiunan Xu, Yang Zhang, Congcong Le, and Claudia Felser. Optical method to detect the relationship between chirality of reciprocal space chiral multifold fermions and real space chiral crystals. *Physical Review B*, 102(10):104111, 2020.
- [244] George B Kauffman and Robin D Myers. The resolution of racemic acid: A classic stereochemical experiment for the undergraduate laboratory. *Journal of Chemical Education*, 52(12):777, 1975.
- [245] Niels BM Schröter, Ding Pei, Maia G Vergniory, Yan Sun, Kaustuv Manna, Fernando De Juan, Jonas A Krieger, Vicky Süss, Marcus Schmidt, Pavel Dudin, Barry Bradiyn, Timur K Kim, Thorsten Schmitt, Cephise Cacho, Claudia Felser, and Yulin Strocov, Vladimir N an d Chen. Chiral topological semimetal with multifold band crossings and long Fermi arcs. *Nature Physics*, 15(8):759–765, 2019.
- [246] Pierre Rinkel, Pedro LS Lopes, and Ion Garate. Signatures of the chiral anomaly in phonon dynamics. *Physical Review Letters*, 119(10):107401, 2017.
- [247] Gerhard H Fecher, Jürgen Kübler, and Claudia Felser. Chirality in the solid state: Chiral crystal structures in chiral and achiral space groups. *Materials*, 15(17):5812, 2022.

- [248] Fernando De Juan, Adolfo G Grushin, Takahiro Morimoto, and Joel E Moore. Quantized circular photogalvanic effect in Weyl semimetals. *Nature Communications*, 8(1):15995, 2017.
- [249] Guoqing Chang, Su-Yang Xu, Benjamin J Wieder, Daniel S Sanchez, Shin-Ming Huang, Ilya Belopolski, Tay-Rong Chang, Songtian Zhang, Arun Bansil, Hsin Lin, and M. Zahid Hasan. Unconventional chiral fermions and large topological Fermi arcs in RhSi. *Physical Review Letters*, 119(20):206401, 2017.
- [250] Felix Flicker, Fernando De Juan, Barry Bradlyn, Takahiro Morimoto, Maia G Vergniory, and Adolfo G Grushin. Chiral optical response of multifold fermions. *Physical Review B*, 98(15):155145, 2018.
- [251] Daniel S Sanchez, Ilya Belopolski, Tyler A Cochran, Xitong Xu, Jia-Xin Yin, Guoqing Chang, Weiwei Xie, Kaustuv Manna, Vicky Süß, Cheng-Yi Huang, Nasser Alidoust, Daniel Multer, Songtian S Zhang, Nana Shumiya, Xirui Wang, Guang-Qiang Wang, Tay-Rong Chang, Claudia Felser, Su-Yang Xu, Shuang Jia, Hsin Lin, and M. Zahid Hasan. Topological chiral crystals with helicoid-arc quantum states. *Nature*, 567(7749):500–505, 2019.
- [252] Qian-Qian Yuan, Liqin Zhou, Zhi-Cheng Rao, Shangjie Tian, Wei-Min Zhao, Cheng-Long Xue, Yixuan Liu, Tiantian Zhang, Cen-Yao Tang, Zhi-Qiang Shi, Zhen-Yu Jia, Hongming Weng, Hong Ding, Yu-Jie Sun, Hechang Lie, and Shao-Chun Li. Quasiparticle interference evidence of the topological Fermi arc states in chiral fermionic semimetal CoSi. *Science Advances*, 5(12):eaaw9485, 2019.
- [253] Paolo Sessi, Feng-Ren Fan, Felix Küster, Kaustuv Manna, Niels BM Schröter, Jing-Rong Ji, Samuel Stolz, Jonas A Krieger, Ding Pei, Timur K Kim, Pavel Dudin, Cephise Cacho, Roland Widmer, Horst Borrmann, Wujun Shi, Kai Chang, Yan Sun, Claudia Felser, and Stuart SP Parkin. Handedness-dependent quasiparticle interference in the two enantiomers of the topological chiral semimetal pdga. *Nature Communications*, 11(1):3507, 2020.
- [254] Qi Wu and X-C Zhang. Free-space electro-optic sampling of terahertz beams. *Applied Physics Letters*, 67(24):3523–3525, 1995.
- [255] Jeremy A Johnson, Fabian DJ Brunner, Sebastian Grübel, Andrés Ferrer, Steven L Johnson, and Thomas Feurer. Distortion-free enhancement of terahertz signals measured by electro-optic sampling. II. experiment. *JOSA B*, 31(5):1035–1040, 2014.
- [256] Achim Gelessus, Walter Thiel, and Wolfgang Weber. Multipoles and symmetry. *Journal of Chemical Education*, 72(6):505, 1995.
- [257] Robert W Boyd, Alexander L Gaeta, and Enno Giese. Nonlinear optics. In *Springer Handbook of Atomic, Molecular, and Optical Physics*, pages 1097–1110. Springer, 2008.

APPENDIX

APPENDIX A

ROTATIONAL ANISOTROPY SECOND HARMONIC GENERATION WITH SUBGROUP OF C_{4V}

C_{4v}	E	$2C_4$	C_2	$2\sigma_v$	$2\sigma_d$
A_1	1	1	1	1	1
A_2	1	1	1	-1	-1
B_1	1	-1	1	1	-1
B_2	1	-1	1	-1	1
E	2	0	-2	0	0

Table A.1: Character table for C_{4v} point group.

The LnAlSi ($\text{Ln} = \text{La, Ce, Pr, and Nd}$) belongs to the point group C_{4v} . This point group has following symmetry operation:

E: Identical operation.

$2C_4$: Two four-fold rotational symmetry around the principle axis.

C_2 : Two fold rotational symmetry around the principle axis.

$2\sigma_v$: Two vertical mirror planes

$2\sigma_d$: Two dihedral mirror planes

In physics, an irreducible representation describes the basic methods by which a symmetry group influences a physical system, effectively representing the system's fundamental characteristics. These representations are essential for understanding the behavior of a physical system when subjected to different symmetry operations, such as rotation, reflection, and translation. In C_{4v} , there are five irreducible representations in which A and B are non-degenerate singlets representations, but E is a doubly degenerate representation. The irreducible representation A_1 is totally symmetric, i.e., it does not change under all symmetric operations, but A_2 changes its sign under mirror planes [256]. In order to rule out a structural origin of the SHG response, we relaxed the point group symmetries of the material to its nearest structural subgroups, i.e., C_4 , C_{2v} , C_2 and C_s . The second harmonic nonlinear susceptibility tensors for electric dipole (ED) χ_{ijk}^{eee} and for magnetic dipole (MD) χ_{ijk}^{eem} for different subgroups are presented below. All susceptibility tensors are generated by considering nonvanishing tensor elements given by Robert W. Boyd [257] with permutation symmetry. The polar (axial) signal originating from ED (MD) sources is calculated for different experimental configurations, as described in Chapter 5. It is presented as a function of the incoming polarization angle ϕ for the (101) facet and calculated results are fitted with experimental data.

A.1 C_{4v} Electric Dipole

Bulk ED susceptibility tensor χ_{ijk}^{eee} for non-centrosymmetric materials belongs to C_{4v} point group which has three non zero elements χ_{xxz}^{eee} , χ_{zxx}^{eee} and χ_{zzz}^{eee} . The polar signal deriving from ED sources as a function of incoming polarization angle ϕ for the (101) facet at different experimental configurations is given by Equation A.1 - A.4. The global fitting with experimental data taken with 1350 nm as an incoming beam is shown in Figure A.1. The global fitting with experimental data taken with 800 nm as an incoming beam is shown in Figure A.2, which does not fit as with 1350 nm incoming light.

$$\chi_{ijk}^{eee} = \left[\begin{array}{c} \left(\begin{array}{c} 0 \\ 0 \\ \chi_{xxz}^{eee} \end{array} \right) \left(\begin{array}{c} 0 \\ 0 \\ 0 \end{array} \right) \left(\begin{array}{c} \chi_{xxz}^{eee} \\ 0 \\ 0 \end{array} \right) \\ \left(\begin{array}{c} 0 \\ 0 \\ 0 \end{array} \right) \left(\begin{array}{c} \chi_{zxx}^{eee} \\ 0 \\ 0 \end{array} \right) \left(\begin{array}{c} 0 \\ 0 \\ \chi_{xxz}^{eee} \end{array} \right) \\ \left(\begin{array}{c} \chi_{zxx}^{eee} \\ 0 \\ 0 \end{array} \right) \left(\begin{array}{c} 0 \\ \chi_{zxx}^{eee} \\ 0 \end{array} \right) \left(\begin{array}{c} 0 \\ 0 \\ \chi_{zzz}^{eee} \end{array} \right) \end{array} \right]_{C_{4v}}$$

$$I_{\parallel}^{eee} = \frac{1}{32} \cos^2(\phi) [(-2\chi_{xxz}^{eee} - \chi_{zxx}^{eee} + \chi_{zzz}^{eee}) \cos(2\phi) + 6\chi_{xxz}^{eee} + 3\chi_{zxx}^{eee} + \chi_{zzz}^{eee}]^2 \quad (\text{A.1})$$

$$I_{\perp}^{eee} = \frac{1}{8} \sin^2(\phi) [(-2\chi_{xxz}^{eee} + \chi_{zxx}^{eee} + \chi_{zzz}^{eee}) \cos^2(\phi) + 2\chi_{zxx}^{eee} \sin^2(\phi)]^2 \quad (\text{A.2})$$

$$I_H^{eee} = \frac{1}{8} [(2\chi_{xxz}^{eee} + \chi_{zxx}^{eee} + \chi_{zzz}^{eee}) \cos^2(\phi) + 2\chi_{zxx}^{eee} \sin^2(\phi)]^2 \quad (\text{A.3})$$

$$I_V^{eee} = 2[\chi_{xxz}^{eee} \sin(\phi) \cos(\phi)]^2 \quad (\text{A.4})$$

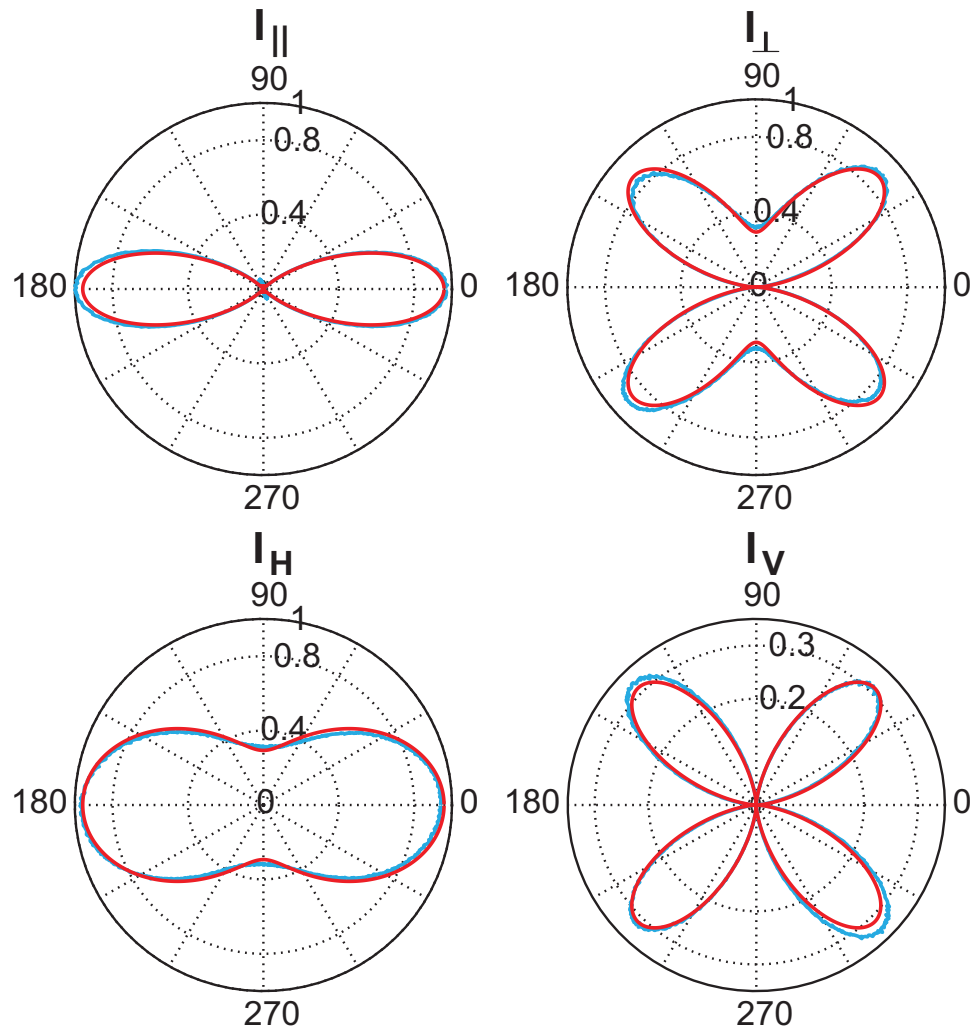


Figure A.1: Experimentally measured second harmonic generation data (blue) for incoming wavelength 1350 nm, outgoing wavelength 675 nm, and fit (red) to bulk electric dipolar SHG in the C_{4v} point group.

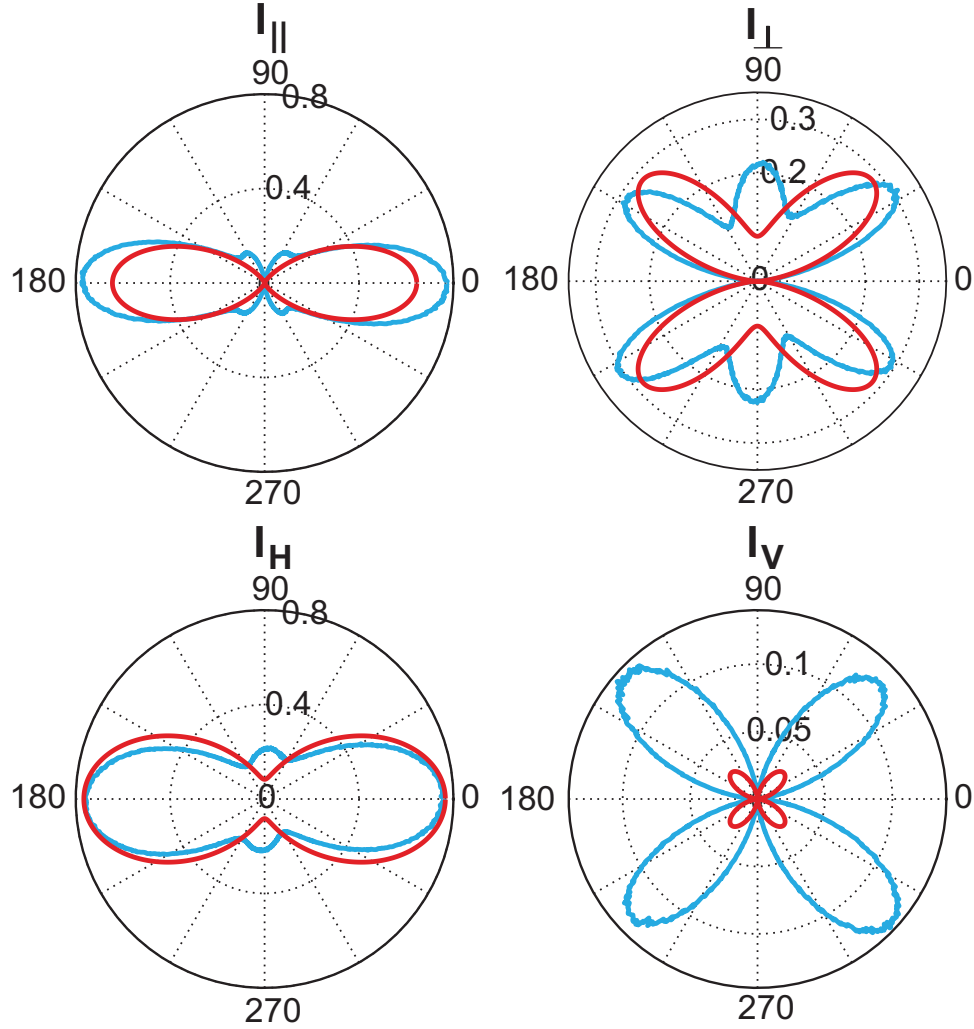


Figure A.2: Experimentally measured second harmonic generation data (blue) for incoming wavelength 800 nm, outgoing wavelength 400 nm, and fit (red) to bulk electric dipolar SHG in the C_{4v} point group.

A.2 C_{2v} Electric Dipole

Bulk ED susceptibility tensor χ_{ijk}^{ee} for C_{2v} point group has five non zero elements. The polar signal deriving from ED sources as a function of incoming polarization angle ϕ for the (101) facet at different experimental configurations is given by Equation A.5 - A.8. The global fitting with experimental data taken with 800 nm as an incoming beam is shown in Figure A.3.

$$\chi_{ijk}^{eee} = \left[\begin{array}{c} \left(\begin{array}{c} 0 \\ 0 \\ \chi_{xxz}^{eee} \end{array} \right) \left(\begin{array}{c} 0 \\ 0 \\ 0 \end{array} \right) \left(\begin{array}{c} \chi_{xxz}^{eee} \\ 0 \\ 0 \end{array} \right) \\ \left(\begin{array}{c} 0 \\ 0 \\ 0 \end{array} \right) \left(\begin{array}{c} 0 \\ 0 \\ \chi_{yyz}^{eee} \end{array} \right) \left(\begin{array}{c} 0 \\ \chi_{yyz}^{eee} \\ 0 \end{array} \right) \\ \left(\begin{array}{c} \chi_{zxx}^{eee} \\ 0 \\ 0 \end{array} \right) \left(\begin{array}{c} 0 \\ \chi_{zyy}^{eee} \\ 0 \end{array} \right) \left(\begin{array}{c} 0 \\ 0 \\ \chi_{zzz}^{eee} \end{array} \right) \end{array} \right]_{C_{2v}}$$

$$I_{\parallel}^{eee} = \frac{1}{8} [(2\chi_{xxz}^{eee} + \chi_{zxx}^{eee} + \chi_{zzz}^{eee}) \cos^3(\phi) + (2\chi_{yyz}^{eee} + \chi_{zyy}^{eee}) \sin(\phi) \sin(2\phi)]^2 \quad (\text{A.5})$$

$$I_{\perp}^{eee} = \frac{1}{8} [(2\chi_{xxz}^{eee} - 4\chi_{yyz}^{eee} + \chi_{zxx}^{eee} + \chi_{zzz}^{eee}) \cos^2(\phi) \sin(\phi) + 2\chi_{zyy}^{eee} \sin^3(\phi)]^2 \quad (\text{A.6})$$

$$I_H^{eee} = \frac{1}{8} [(2\chi_{xxz}^{eee} + \chi_{zxx}^{eee} + \chi_{zzz}^{eee}) \cos^2(\phi) + 2\chi_{zyy}^{eee} \sin^2(\phi)]^2 \quad (\text{A.7})$$

$$I_V^{eee} = 2[\chi_{yyz}^{eee} \cos \phi \sin \phi]^2 \quad (\text{A.8})$$

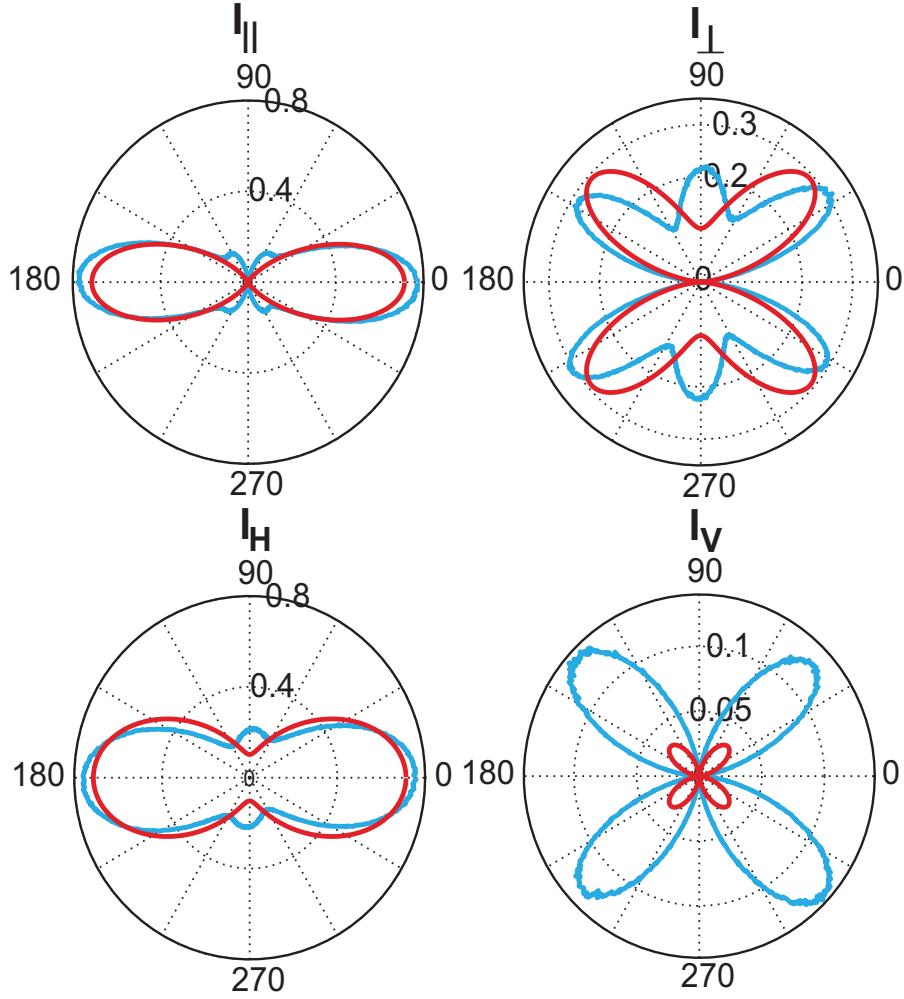


Figure A.3: Experimentally measured second harmonic generation data (blue) for incoming wavelength 800 nm, outgoing wavelength 400 nm, and fit (red) to bulk electric dipolar SHG in the C_{2v} point group.

A.3 C_2 Electric Dipole

Bulk ED susceptibility tensor χ_{ijk}^{eee} for C_2 point group has eight non zero elements. The polar signal deriving from ED sources as a function of incoming polarization angle ϕ for the (101) facet at different experimental configurations is given by Equation A.9 - A.12. The global fitting with experimental data taken with 800 nm as an incoming beam is shown in Figure A.4.

$$\chi_{ijk}^{eee} = \left[\begin{array}{c} \left(\begin{array}{c} 0 \\ 0 \\ \chi_{xxz}^{eee} \end{array} \right) \\ \left(\begin{array}{c} 0 \\ 0 \\ \chi_{xyz}^{eee} \end{array} \right) \\ \left(\begin{array}{c} 0 \\ 0 \\ \chi_{yxz}^{eee} \end{array} \right) \\ \left(\begin{array}{c} 0 \\ 0 \\ \chi_{yyz}^{eee} \end{array} \right) \\ \left(\begin{array}{c} \chi_{yxz}^{eee} \\ \chi_{zxx}^{eee} \\ \chi_{zxy}^{eee} \\ 0 \end{array} \right) \\ \left(\begin{array}{c} \chi_{xyz}^{eee} \\ \chi_{yyz}^{eee} \\ \chi_{zxy}^{eee} \\ 0 \end{array} \right) \\ \left(\begin{array}{c} \chi_{xxz}^{eee} \\ \chi_{xyz}^{eee} \\ 0 \\ \chi_{yxz}^{eee} \\ \chi_{yyz}^{eee} \\ 0 \\ 0 \\ \chi_{zzz}^{eee} \end{array} \right) \end{array} \right]_{C_2}$$

$$I_{\parallel}^{eee} = \frac{1}{16} [\sqrt{2}(2\chi_{xxz}^{eee} + \chi_{zxx}^{eee} + \chi_{zzz}^{eee}) \cos^3(\phi) + 2 \cos(\phi) \sin(\phi) (2(\chi_{xyz}^{eee} + \chi_{yxz}^{eee} + \chi_{zxy}^{eee}) \cos(\phi) + \sqrt{2}(\chi_{yyz}^{eee} + \chi_{zyy}^{eee}) \sin(\phi))]^2 \quad (\text{A.9})$$

$$I_{\perp}^{eee} = [-\chi_{yxz}^{eee} \cos^3(\phi) + \frac{(2\chi_{xxz}^{eee} - 4\chi_{yyz}^{eee} + \chi_{zxx}^{eee} + \chi_{zzz}^{eee}) \cos^2(\phi) \sin(\phi)}{2\sqrt{2}} + (\chi_{xyz}^{eee} + \chi_{zxy}^{eee}) \cos(\phi) \sin^2(\phi) + \frac{\chi_{zyy}^{eee} \sin^3(\phi)}{\sqrt{2}}]^2 \quad (\text{A.10})$$

$$I_H^{eee} = \frac{1}{16} [\sqrt{2}(2\chi_{xxz}^{eee} + \chi_{zxx}^{eee} + \chi_{zzz}^{eee}) \cos^2(\phi) + 2 \sin(\phi) (2(\chi_{xyz}^{eee} + \chi_{zxy}^{eee}) \cos(\phi) + \sqrt{2}\chi_{zyy}^{eee} \sin(\phi))]^2 \quad (\text{A.11})$$

$$I_V^{eee} = \cos^2(\phi) [\chi_{yxz}^{eee} \cos(\phi) + \sqrt{2}\chi_{yyz}^{eee} \sin(\phi)]^2 \quad (\text{A.12})$$

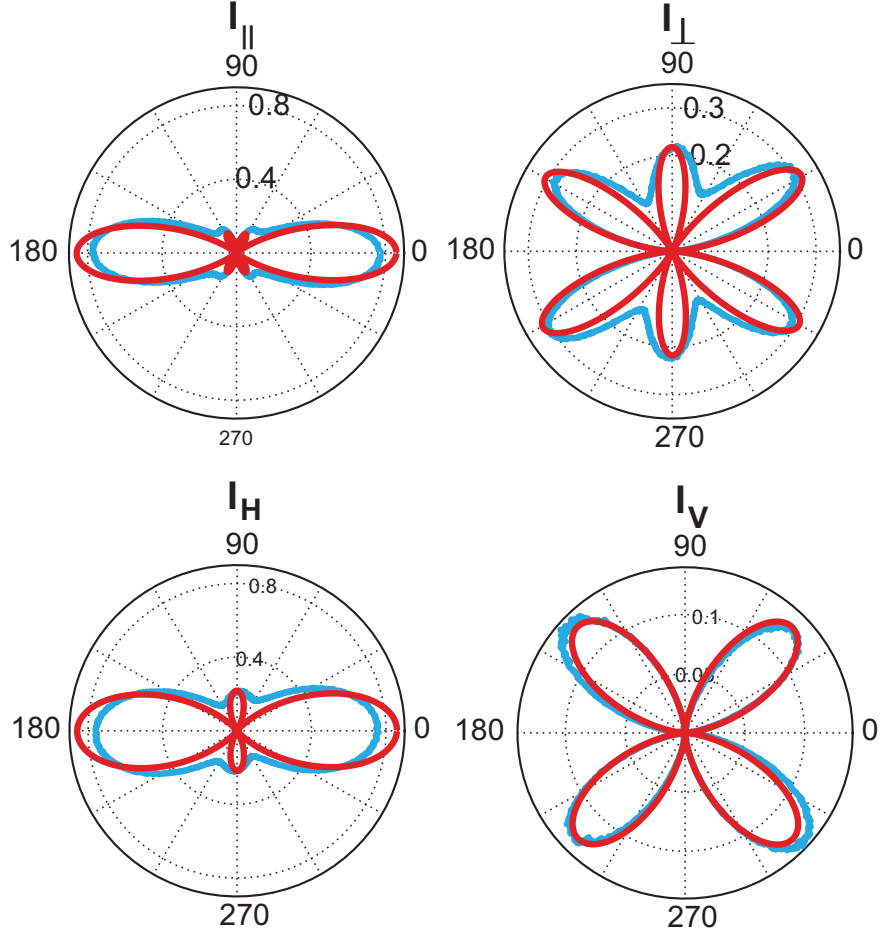


Figure A.4: Experimentally measured second harmonic generation data (blue) for incoming wavelength 800 nm, outgoing wavelength 400 nm, and fit (red) to bulk electric dipolar SHG in the C_2 point group.

A.4 C_4 Electric Dipole

Bulk ED susceptibility tensor χ_{ijk}^{eee} for C_4 point group has five non zero elements. The polar signal deriving from ED sources as a function of incoming polarization angle ϕ for the (101) facet at different experimental configurations is given by Equation A.13 - A.16. The global fitting with experimental data taken with 800 nm as an incoming beam is shown in Figure A.5.

$$\chi_{ijk}^{eee} = \left[\begin{array}{ccc} \begin{pmatrix} 0 \\ 0 \\ \chi_{xxz}^{eee} \end{pmatrix} & \begin{pmatrix} 0 \\ 0 \\ \chi_{xyz}^{eee} \end{pmatrix} & \begin{pmatrix} \chi_{xxz}^{eee} \\ \chi_{xyz}^{eee} \\ 0 \end{pmatrix} \\ \begin{pmatrix} 0 \\ 0 \\ -\chi_{xyz}^{eee} \end{pmatrix} & \begin{pmatrix} 0 \\ 0 \\ \chi_{xxz}^{eee} \end{pmatrix} & \begin{pmatrix} -\chi_{xyz}^{eee} \\ \chi_{xxz}^{eee} \\ 0 \end{pmatrix} \\ \begin{pmatrix} \chi_{zxx}^{eee} \\ \chi_{zxy}^{eee} \\ 0 \end{pmatrix} & \begin{pmatrix} -\chi_{zxy}^{eee} \\ \chi_{zxx}^{eee} \\ 0 \end{pmatrix} & \begin{pmatrix} 0 \\ 0 \\ \chi_{zzz}^{eee} \end{pmatrix} \end{array} \right]_{C_4}$$

$$I_{\parallel}^{eee} = \frac{1}{32} \cos^2(\phi) [6\chi_{xxz}^{eee} + 3\chi_{zxx}^{eee} + \chi_{zzz}^{eee} + (-2\chi_{xxz}^{eee} - \chi_{zxx}^{eee} + \chi_{zzz}^{eee}) \cos(2\phi)]^2 \quad (\text{A.13})$$

$$I_{\perp}^{eee} = [\chi_{xyz}^{eee} \cos(\phi) + \frac{1}{8\sqrt{2}} (-2\chi_{xxz}^{eee} + 7\chi_{zxx}^{eee} + \chi_{zzz}^{eee}) \sin(\phi) + (-2\chi_{xxz}^{eee} - \chi_{zxx}^{eee} + \chi_{zzz}^{eee}) \sin(3\phi)]^2 \quad (\text{A.14})$$

$$I_H^{eee} = \frac{1}{16} [\sqrt{2}(2\chi_{xxz}^{eee} + \chi_{zxx}^{eee} + \chi_{zzz}^{eee}) \cos^2(\phi) + 4\chi_{xyz}^{eee} \cos(\phi) \sin(\phi) + 2\sqrt{2}\chi_{zxx}^{eee} \sin^2(\phi)]^2 \quad (\text{A.15})$$

$$I_V^{eee} = \cos^2(\phi) [\chi_{xyz}^{eee} \cos(\phi) - \sqrt{2}\chi_{xxz}^{eee} \sin(\phi)]^2 \quad (\text{A.16})$$

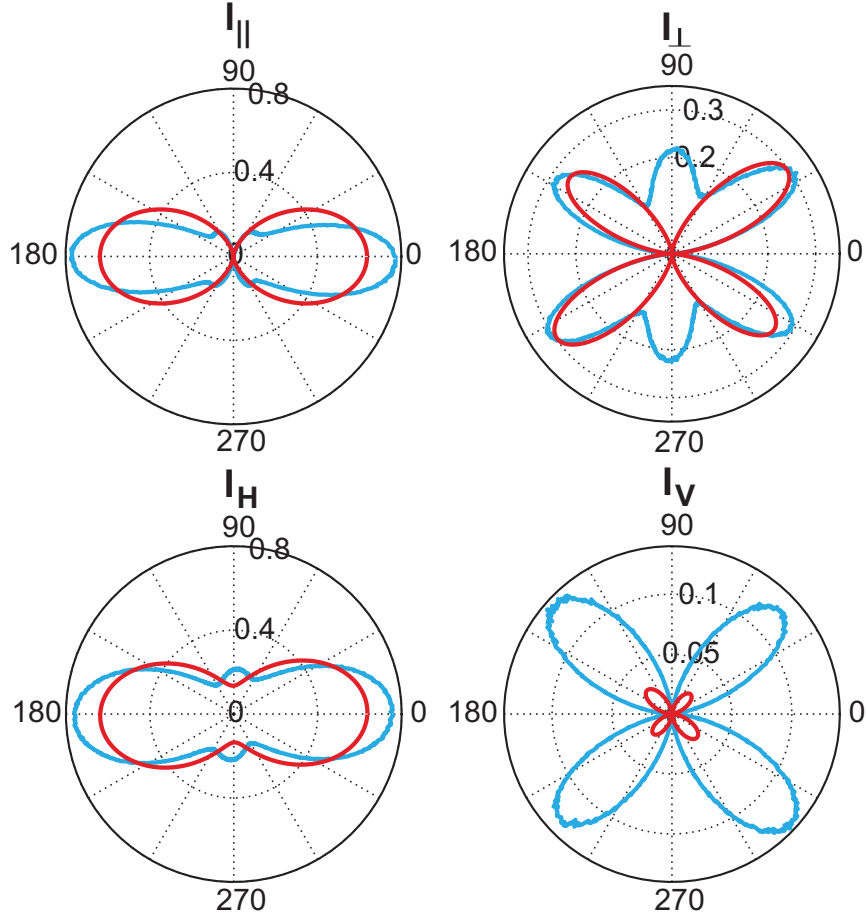


Figure A.5: Experimentally measured second harmonic generation data (blue) for incoming wavelength 800 nm, outgoing wavelength 400 nm, and fit (red) to bulk electric dipolar SHG in the C_4 point group.

A.5 C_s Electric Dipole

Bulk ED susceptibility tensor χ_{ijk}^{eee} for C_s point group has ten non-zero elements. The polar signal deriving from ED sources as a function of incoming polarization angle ϕ for the (101) facet at different experimental configurations is given by Equation A.17 - A.20. The global fitting with experimental data taken with 800 nm as an incoming beam is shown in Figure A.6.

$$\chi_{ijk}^{eee} = \left[\begin{array}{c} \left(\begin{array}{c} \chi_{xxx}^{eee} \\ \chi_{xxy}^{eee} \\ 0 \end{array} \right) \left(\begin{array}{c} \chi_{xxy}^{eee} \\ \chi_{xyy}^{eee} \\ 0 \end{array} \right) \left(\begin{array}{c} 0 \\ 0 \\ \chi_{xzz}^{eee} \end{array} \right) \\ \left(\begin{array}{c} \chi_{yxx}^{eee} \\ \chi_{yxy}^{eee} \\ 0 \end{array} \right) \left(\begin{array}{c} \chi_{yxy}^{eee} \\ \chi_{yyy}^{eee} \\ 0 \end{array} \right) \left(\begin{array}{c} 0 \\ 0 \\ \chi_{yzz}^{eee} \end{array} \right) \\ \left(\begin{array}{c} 0 \\ 0 \\ 0 \end{array} \right) \left(\begin{array}{c} 0 \\ 0 \\ 0 \end{array} \right) \left(\begin{array}{c} \chi_{zzx}^{eee} \\ \chi_{zzy}^{eee} \\ 0 \end{array} \right) \end{array} \right]_{C_s}$$

$$\begin{aligned} I_{\parallel}^{eee} &= \frac{1}{16} (\sqrt{2}(\chi_{xxx}^{eee} + \chi_{xzz}^{eee} + 2\chi_{zzx}^{eee}) \cos^3(\phi) + 2(2\chi_{xxy}^{eee} + \chi_{yxx}^{eee} + \chi_{yzz}^{eee}) \cos^2(\phi) \sin(\phi) \\ &\quad + 4 \sin^2(\phi) (\sqrt{2}\chi_{yxy}^{eee} \cos(\phi) + \chi_{yyy}^{eee} \sin(\phi)) + ((\chi_{zzy}^{eee} + \chi_{zzy}^{eee}) \cos(\phi) + \sqrt{2}\chi_{xyy}^{eee} \sin(\phi)) \sin(2\phi))^2 \end{aligned} \quad (\text{A.17})$$

$$\begin{aligned} I_{\perp}^{eee} &= \frac{1}{16} [-2(\chi_{yxx}^{eee} + \chi_{yzz}^{eee}) \cos^3(\phi) + \sqrt{2}(\chi_{xxx}^{eee} + \chi_{xzz}^{eee} - 4\chi_{yxy}^{eee} + 2\chi_{zzx}^{eee}) \cos^2(\phi) \sin(\phi) \\ &\quad + 2\sqrt{2}\chi_{xyy}^{eee} \sin^3(\phi) + (2\chi_{xxy}^{eee} - 2\chi_{yyy}^{eee} + \chi_{zzy}^{eee} + \chi_{zzy}^{eee}) \sin(\phi) \sin(2\phi)]^2 \end{aligned} \quad (\text{A.18})$$

$$\begin{aligned} I_H^{eee} &= \frac{1}{16} [\sqrt{2}(\chi_{xxx}^{eee} + \chi_{xzz}^{eee} + 2\chi_{zzx}^{eee}) \cos^2(\phi) + 2\sqrt{2}\chi_{xyy}^{eee} \sin^2(\phi) + (2\chi_{xxy}^{eee} + \chi_{zzy}^{eee} \\ &\quad + \chi_{zzy}^{eee}) \sin(2\phi)]^2 \end{aligned} \quad (\text{A.19})$$

$$I_V^{eee} = \left[\frac{1}{2} (\chi_{yxx}^{eee} + \chi_{yzz}^{eee}) \cos^2(\phi) + \sqrt{2}\chi_{yxy}^{eee} \cos(\phi) \sin(\phi) + \chi_{yyy}^{eee} \sin^2(\phi) \right]^2 \quad (\text{A.20})$$

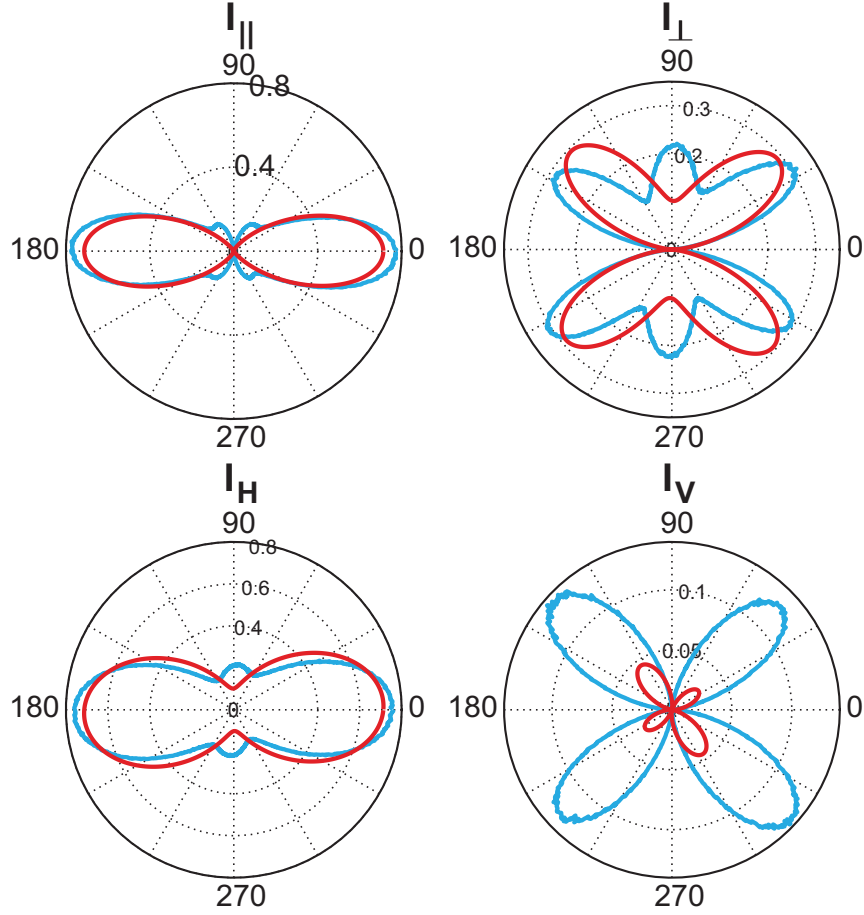


Figure A.6: Experimentally measured second harmonic generation data (blue) for incoming wavelength 800 nm, outgoing wavelength 400 nm, and fit (red) to bulk electric dipolar SHG in the C_s point group.

A.6 C_{4v} Magnetic Dipole

Bulk MD susceptibility tensor χ_{ijk}^{em} for C_{4v} point group has three non zero elements. The axial signal deriving from ED sources as a function of incoming polarization angle ϕ for the (101) facet at different experimental configurations is given by Equation A.21 - A.24.

$$\chi_{ijk}^{eem} = \left[\begin{array}{ccc} \begin{pmatrix} 0 \\ 0 \\ 0 \end{pmatrix} & \begin{pmatrix} 0 \\ 0 \\ \chi_{xyz}^{eee} \end{pmatrix} & \begin{pmatrix} 0 \\ \chi_{xzy}^{eee} \\ 0 \end{pmatrix} \\ \begin{pmatrix} 0 \\ 0 \\ -\chi_{xyz}^{eee} \end{pmatrix} & \begin{pmatrix} 0 \\ 0 \\ 0 \end{pmatrix} & \begin{pmatrix} -\chi_{xzy}^{eee} \\ 0 \\ 0 \end{pmatrix} \\ \begin{pmatrix} 0 \\ \chi_{zxy}^{eee} \\ 0 \end{pmatrix} & \begin{pmatrix} -\chi_{zxy}^{eee} \\ 0 \\ 0 \end{pmatrix} & \begin{pmatrix} 0 \\ 0 \\ 0 \end{pmatrix} \end{array} \right]_{C_{4v}}$$

$$I_{\parallel}^{eem} = \frac{1}{4}(\chi_{xzy}^{eem} + \chi_{zxy}^{eem})^2 \cos^2(\phi) \quad (\text{A.21})$$

$$I_{\perp}^{eem} = \frac{1}{4}(\chi_{xyz}^{eem} - \chi_{zxy}^{eem})^2 \sin^2(\phi) \quad (\text{A.22})$$

$$I_H^{eem} = \frac{1}{16}[-\chi_{xyz}^{eem} + \chi_{xzy}^{eem} + 2\chi_{zxy}^{eem} + (\chi_{xyz}^{eem} + \chi_{xzy}^{eem}) \cos(2\phi)]^2 \quad (\text{A.23})$$

$$I_V^{eem} = \frac{1}{16}(\chi_{xyz}^{eem} + \chi_{xzy}^{eem})^2 \sin^2(2\phi) \quad (\text{A.24})$$

A.7 C_{4v} Magnetic Dipole and Electric Dipole

In this case, both polar and axial responses from the sample are considered, as described in Chapter 5. The polar signal deriving from ED sources as a function of incoming polarization angle ϕ for the (101) facet at different experimental configurations is given by Equation. The global fitting with experimental data taken with 800 nm as an incoming beam for all studied samples LnAlSi is shown in Figure A.7.

$$I_{\parallel} = \frac{1}{32} \cos^2(\phi) [(-2\chi_{xxz}^{eee} - \chi_{zxx}^{eee} + \chi_{zzz}^{eee}) \cos(2\phi) + 6\chi_{xxz}^{eee} + 3\chi_{zxx}^{eee} + \chi_{zzz}^{eee}]^2 + \frac{1}{4} (\chi_{xzy}^{eem} + \chi_{zxy}^{eem})^2 \cos^2(\phi) \quad (\text{A.25})$$

$$I_{\perp} = \frac{1}{8} \sin^2(\phi) [(-2\chi_{xxz}^{eee} + \chi_{zxx}^{eee} + \chi_{zzz}^{eee}) \cos^2(\phi) + 2\chi_{zxx}^{eee} \sin^2(\phi)]^2 + \frac{1}{4} (\chi_{xyz}^{eem} - \chi_{zxy}^{eem})^2 \sin^2(\phi) \quad (\text{A.26})$$

$$I_H = \frac{1}{8} [(2\chi_{xxz}^{eee} + \chi_{zxx}^{eee} + \chi_{zzz}^{eee}) \cos^2(\phi) + 2\chi_{zxx}^{eee} \sin^2(\phi)]^2 + \frac{1}{16} [-\chi_{xyz}^{eem} + \chi_{xzy}^{eem} + 2\chi_{zxy}^{eem} + (\chi_{xyz}^{eem} + \chi_{xzy}^{eem}) \cos(2\phi)]^2 \quad (\text{A.27})$$

$$I_V = 2[\chi_{xxz}^{eee} \sin(\phi) \cos(\phi)]^2 + \frac{1}{16} (\chi_{xyz}^{eem} + \chi_{xzy}^{eem})^2 \sin^2(2\phi) \quad (\text{A.28})$$

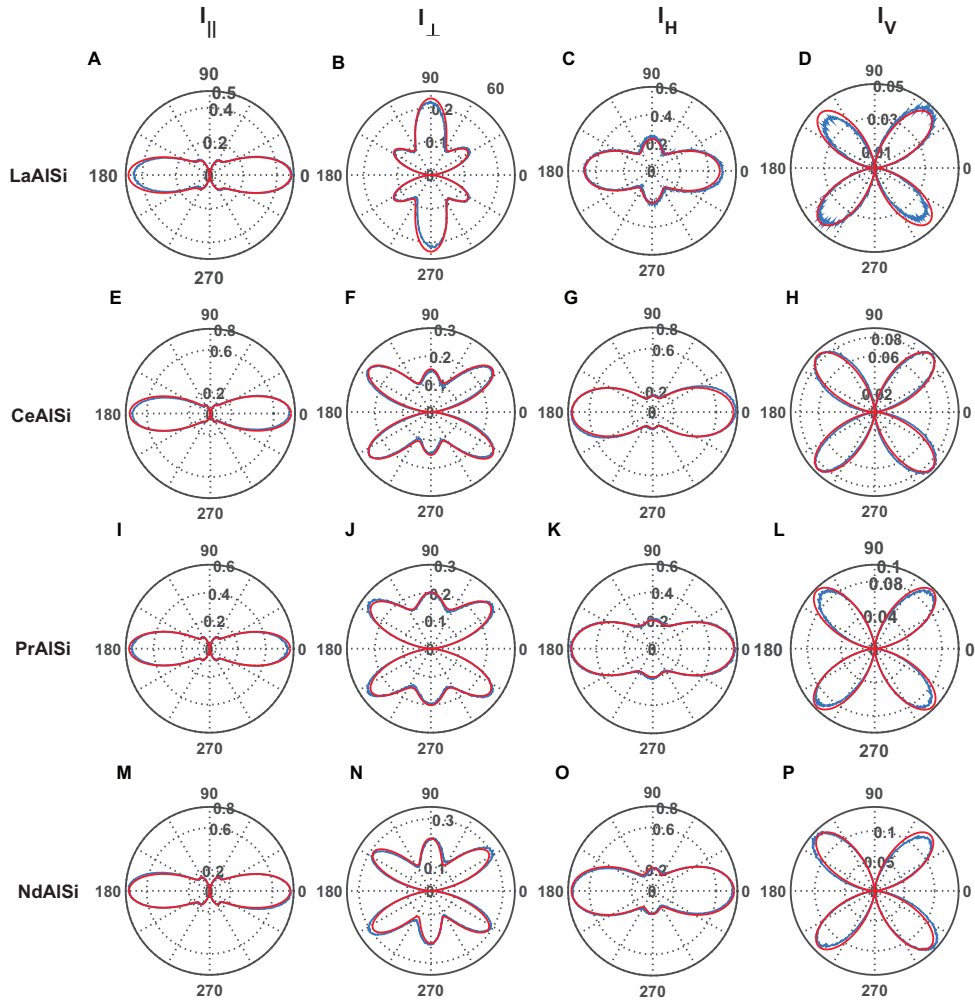


Figure A.7: Experimentally measured second harmonic generation data for incoming wavelength 800 nm, outgoing wavelength 400 nm, and fit to bulk electric and Magnetic dipolar SHG in the C_{4v} point group.